Tel Aviv University
Raymond and Beverly Sackler
Faculty of Exact Sciences

Examination of Kelvin-Helmholtz Instability as a Mechanism of Deformation in the Lisan Formation, Dead Sea Basin

Thesis submitted in partial fulfillment
Of the requirement for the degree of

M.Sc in Geophysics and Planetary Sciences

by

Nadav Wetzler

This work was carried out under the supervision of

Prof. Shmuel Marco

Dr. Eyal Heifetz

April 2009

Cover: Vincent Van Gogh, La Nuit Etoilee, 1888

Dedicated to my precious daughter Ella.

Abstract

The origin of the soft sediment deformation along the Lisan Formation has been convincingly tied to the tectonic activity of the Dead Sea Transform (DST) fault-system at the Late Pleistocene (Heifetz et al., 2005). The remarkable visual similarity of these seismites to Kelvin-Helmholtz instability (KHI) billows has given reason for the suspicion that these folds were formed under mechanism of shear instability.

In this research we investigate the feasibility of such mechanisms in the geological conditions of paleolake Lisan, the ancestor of the present Dead Sea. Throughout we explore these geometrical features by fluid dynamics methods that combine spectral analysis, numerical simulation and laboratory experiment.

We perform a set of geometrical examinations of more then 300 folds structures in the Lisan Formation. We suggest that these folds evolved through deformation stages that began as linear folding to non-linear coherent billows, under the influence of shear instability, and into a final stage of turbulence. Spectral analysis of these coherent billows indicates a uniform behavior and high spectral correlations to the turbulent stratified anisotropic power law of -1.9. This special power law is compatible with the turbulent nature of shear instability mechanisms such as KHI. The feasibility of such mechanisms is also dependent on the configuration of the density profile and the composition of the medium. Therefore we measured the properties of the sediments, namely viscosity and density, in their water-saturated condition for modeling purposes.

The feasibility investigation of such a shear instability mechanism was followed by Computational Fluid Dynamics (CFD) model by using the commercial software Fluent. We use three types of meshes, 2m long and 0.04, 0.1, and 0.5 meter high, divided into two layers of fluids, compatible with the Lisan prehistoric profile as evaluated. The model was based on evaluated density profile suitable to lacustrine environments. Under the conditions of the natural process of sedimentation, lighter layers of sediment stratified on top of denser sediments. This setup was combined with a sheared velocity field determined by a User Defined Function (UDF) also including sinusoidal perturbation. Sinusoidal perturbation simulates attenuation of the medium along the interfaces between layers during large earthquakes, and velocity field set by acceleration parameter 0.1 to 0.6g, induced as a result to the density profile. Simulations shows that the generation of KH billows are tied to the thickness of the layer and the intensity of the velocity shear e.g.

ground acceleration. Based on the CFD results we suggest a deformation-stage-scale that determines the peak ground acceleration occurring during the earthquake based on the degree of the deformed feature and its size.

The last chapter of this work is dedicated to laboratory experiments, in which two layers of mud resembling the Lisan wet sediments (collected from the Ze'elim Formation exposed around the Dead Sea) were laid horizontally in a water tank. The motion was set off as the water tank was tilted to an angle of 45^o, providing shear mechanism induced by gravity. Although experiments show that gravitational slide may produce small-scaled features such KHI, it is insufficient in order to overcome viscous forces within the sediments under smaller angels or produce larger billow-like folds as seen in the Lisan.
This research shows that the Lisan Formation answers to all criterions of shear like mechanism such as KHI, as the geometrical spectral analysis confirms turbulence and the CFD model demonstrated overwhelming similarity to the Lisan billow-like folds.

Acknowledgments

First of all I would like to thank my two supervisors Prof. Shmuel Marco and Dr. Eyal Heifetz who made this research so interesting and provided me with full support and academic freedom. With the collaboration of the geological and fluid dynamics approaches I was able to cope with the full aspects of this beautiful natural phenomenon. I am extremely grateful to both of them.

I would also like to thank my wife Michal for the love, moral and mental support, who throughout this research gave birth to our wonderful daughter Ella.

To my two loving father and mother.

I would like to thank Chloe Cook and Thomas Ermer for editing this thesis.

I also would like to thank Ehud Hadad for providing us with the aluminum grid.

Contents

List of figures

List of tables

1 INTRODUCTION

Folds are very common tectonic structures on earth. They usually involve plastic deformation (bending or buckling) of single or multiple layers, such as sediments or rocks. Folds range in scale from microscopic (in cases of fine-grained metamorphic rocks) to hundreds of kilometers across in epeirogenic warps (such as the Michigan basin) (Suppe, 1985). In most circumstances the folding process occurs under varying conditions of stress, hydrostatic pressure, pore pressure and heat, and may occur over a period of thousands or many more years. Folds are mainly classified according to their size, shape, tightness and dip of the axial plane. The mechanisms of folding are not limited only to rocks. It depends primarily on the nature of the materials of the layers that is contained in the deformed volume. Folded structures can be found in layered materials such as wood, metal, rubber, plastic, or viscous liquids. Furthermore, after the initial stage of deforming or bending, many folds under extreme conditions (for example metamorphic or shear instability) continue to grow largely through near homogenous ductile flow of the volume body, producing amplification and distortion of the existing fold. Thus the shape of the folds reflects a combination of several processes (Suppe, 1985).

Our case study addresses the case of multilayer folds. Multilayer folds exhibit an extremely wide variety of geometric form and scale of folds in naturally deformed rocks. In this work we investigate the special case of multilayer folds of the lacustrine Late Pleistocene Lisan Formation, Dead Sea basin.

The natural ductile property of soft sediments allows plastic flexibility under conditions of brutal force. The trigger mechanism of soft sediments deformation is discussed in numerous studies and previous research (Agnon et al., 2006; Arkin, 1985; Bachmann and Aref, 2005; Bartov and Sagy, 2004; Begin et al., 2005b; Ben-Menahem, 1991; El Isa and Mustafa, 1986; Garfunkel et al., 1981; Heifetz et al., 2005; Marco and Agnon, 2005; Marco et al., 2005; Marco et al., 1996). The terminology of these structures is complex and based largely on the investigator's perception of structure, geometry and origin (Lowe, 1975). These previous research refer to a wide variety of sedimentary conditions and driving forces including extensional stress fields, gravitational instabilities, overloading and unequal loading processes e.g. relative sea-level rise (Bachmann and Aref, 2005), and ground shaking. These mechanisms usually involve the process of pore-water escape and sediment compaction on the one hand, and liquefaction on the other.

Earthquakes may leave several types of marks on soft laminated beds including pseudondules, ball-and-pillow structures, folds, sagging structures, slumps, water-escape structures and microfaults (Bachmann and Aref, 2005; Rodriguez-Lopez et al., 2007; Rossetti, 1999). These features are known by the term *seismites*. The term seismite refers to beds interpreted to be deformed by seismic shock (Seilache.A, 1969). The delicate sediments makes seismites, which are observed within stratified depositional basins, an excellent candidate for paleoseismic research (Amit et al., 2002; Heifetz et al., 2005; Marco and Agnon, 2005; Marco et al., 2005; Marco et al., 1996; Rossetti, 1999). Such is the Lisan Formation, which lies close to of the active Dead Sea basin (DSB).

This research focuses on folds from a different perspective. The folds presented in this research are part of a large collection of paleoseismic data common within the well bedded (Figure 4) layers of the Lisan Formation, west side of the Dead Sea basin, south east Israel. The folds come in various sizes and in the form of billows or waves. Up until now, several mechanisms were suggested to be the inducing process that forms these structures, but none of them were investigated. In this research we investigate the feasibility that the folding occurs under the configuration of shear instability. The striking similarity of the fine-grained structures to KHI suggests that shear plays a central role in soft sediments deformation. We suggest that the folded geometrical structures of the Lisan Formation are seismites, produced by a sheared velocity flow induced by a large energy source – earthquakes.

1.1 Motivation

The main motivation of any paleoseismic research is to achieve a better understanding of dynamics of the medium induced by earthquakes. We seek the main mechanism that controls the folding of the Lisan's deformations.

In this research we attempt to combine two disciplines while investigating the Lisan's seismogenic features: the geological point of view and fluid dynamics point of view. With the tools of fluid dynamics we inspect the motion of saturated soft sediment under inducing earthquakes according to the geological comprehension of the region is paleo-setup. This gives use a clearer picture of the physics that involves in such complex process.

1.2 Objectives

The aim of this study is to document and interpret series of seismic features of the Lisan Formation in the Dead Sea region. In this work we discuss the seiemogenic origin of the soft sediment folded deformation and the onset primary conditions. This unique type of lacustrine folds remarkably resembles a well-known phenomenon from the world of fluid dynamics: Kelvin-Helmholtz instability.

Models such as shear instability are commonly used to describe atmospheric (Bernhardt, 2002) and oceanic (DeSilva et al., 1996) processes. In this study we attempt to use this approach in order to determine the nature of the relation between the billow-like folds of the Lisan Formation and regional earthquakes properties. We attempt to evaluate the regional sediments properties (density and viscosity) of the paleo-lake Lisan for numerical modeling purposes. This model gives us the impact ratio between peak ground acceleration (PGA) and the degree of the deformation. The guideline model is a configuration of perturbated shear instability of the type KHI, formed by the ground acceleration induced by earthquakes, creating a velocity shear between two horizontal layers of sediments at the lake's floor.

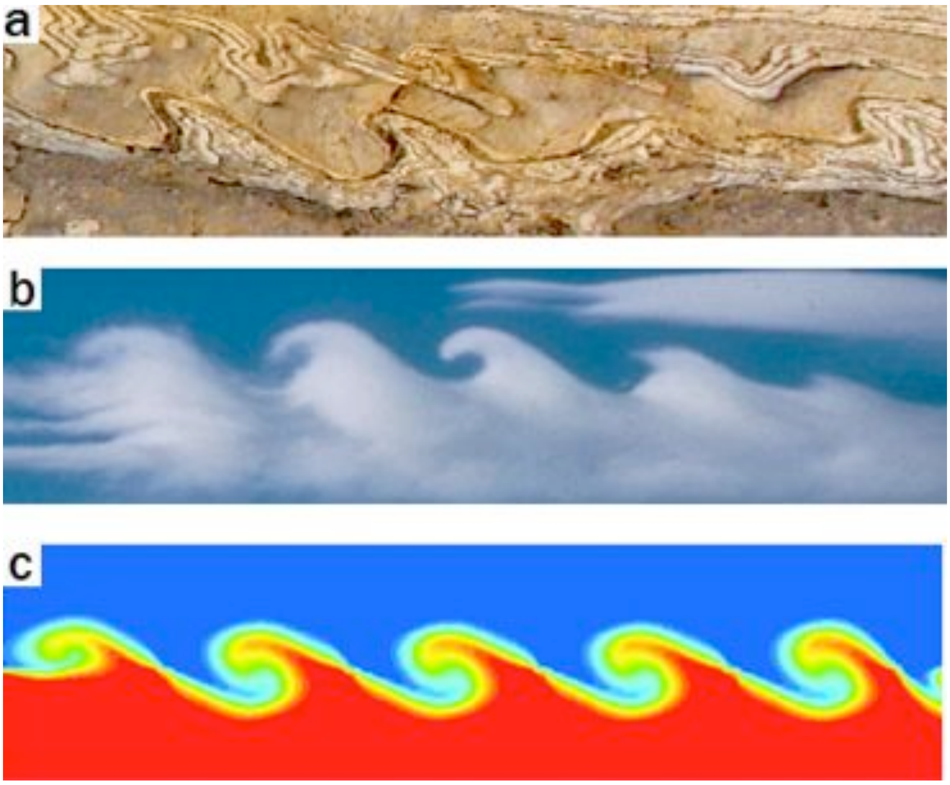

Figure 1 Visual resemblance. a) Deformed laminas, Lisan Formation, Dead Sea, Israel. b) Kelvin Helmholtz billows clouds over the sky of Laramie, Wyoming, USA. c) Numerical simulation of atmospheric KHI by Fluent software, 2.5 km long and 1 km high, using quad mesh of 50,000 cells (Marshall, 2004).

1.3 Geological setting

In this section we provide a large scale view of the region; presenting the stratigraphy from the Late Miocene and up to the Late Pleistocene. We also present the Lisan Formation and its deformed components, the tectonic history and the subject of our research.

1.3.1 Main faulting, Dead Sea transform

The study area lies in the Dead Sea pull-apart graben, which is located at the southern portion of an active strike-slip fault, the Dead Sea Fault system (DSF). The DSF spans 1200 km between the Taurus-Zagros Mountain in the north and the extensional zone of the Red Sea. The fault is the transform boundary between the African and Arabian plates (Hofstetter et al., 2007). This set of faults has been active since the Neogene by the breakup of the once continuous Arabo-African continent (Garfunkel, 1981), and has been one of the major features controlling the configuration and landscape of the Middle East (Figure 3). The transform accumulated in a left-lateral movement of 105 km in the last 17 Myr, which was first recognized by Quennell (1959). Throughout this period the Dead Sea region suffered from recurring earthquakes (Garfunkel et al., 1981), the last of which is the M_L=6.2 earthquake of July 11, 1927 (Figure 2). The entire structural system is characterized by the uplift of its margins, and subsidence of the depressions in between. The uplift of the margins was followed by intensive erosion, where some of its products fill the rift (Mart et al., 2005).

Seismic reflection profiling the Dead Sea reveals that the crust under the Dead Sea is about 33 km and that it thickens by several kilometers to the south (Ginzburg et al., 1981; Weber et al., 2004) with seismic velocities of 6.7 km/s at the lower crust, and ~6.2 km/s at the seismic basement (20 – 7 km deep).

The study sites are close (within a few km) to several faults: the Masada fault system, the Amaziahu fault, and the western margin fault of the DST (Figure 3c).

1.3.2 Secondary fault systems

Faults of variable sizes and ages can be seen almost everywhere along the DST. We will describe shortly some of the main faults along the research area.

1.3.2.1 Masada Fault Zone (MFZ)

The MFZ is a north-striking syndepositional fault system located (Figure 3) on the western coast of the Dead Sea, close to the Jewish rebels' stronghold fortress of Masada. The site ruins are indications of the strong earthquakes of 1202 and 1759, confirmed by paleoseismic observations (Marco and Agnon, 2005).

The MFZ, exposed in Lisan Formation, is mapped by Marco and Agnon (1995). Most of the fault planes strike north, parallel to the main graben faults. Dips are 40^{o} to 70^{o} eastward as well as westward, with normal displacements as much as 2 m. The MFZ provides high spatial and temporal resolution of faulting stage, showing repetitive slip events in the order of several tens of centimeters within time laps of 10^{3} – 10^{4} yr. The seismic events are separated by several hundreds to thousands of years of quiescence (Marco and Agnon, 1995).

1.3.2.2 Amaziahu fault

The Amaziahu fault is located in the margin extension of the DSB, oriented NW - SE. It is a large listric[1] fault on top of the salt layers, which exhibit at least 50m of downdip displacement (Hofstetter et al., 2007). The sedimentary cover that overlaps the fault is deformed by fractures and detached antithetic normal faults.

1.3.3 The Lisan Formation

The Dead Sea region had been occupied by several water-bodies during the Neogene-Quaternary tectonic depression. The region evolved through phases of dehydration from the largest and earliest of these water bodies: the marine *Sedom lagoon*, the *Lake Amora (Samra)*, the Lake Lisan (~70 – 15 kyr B.P.) and finally the Holocene Dead Sea.

The DSB is an 8-10 km deep pull-apart basin that is filled with a thick sequence of sediments transported from a large drainage area. Two major groups of strata have been recognized in the Dead Sea, prerift (pregraben) and synrift (postgraben) or intrarift (Csato et al., 1997). Most researches agree that the prerift stage of the basin ended after the deposition of the *Hazeva Formation*, considered to be late Miocene in age (Garfunkel.Z and Horowitz, 1966) .

The deposits detailed in this study belong to the late Pleistocene Lake Lisan, ancestor of the present Dead Sea and the Sea of Galilee, the Lisan Formation. The Lisan Formation

---

[1] Spoon shaped fault. The fault reduces in dip as it goes deeper.

was deposited during the Würm Pleistocene glacial between ~70 and 15 kyr. It is a well-stratified unit (Figure 4), exposed along 220 km at the margin of the DST, from the northern Arava valley in the south to the Sea of Galilee in the north. The Lisan Formation consists of alternating laminas of white aragonite and dark detritus which were formed by seasonal winter floods and periodic high evaporation (Arkin, 1985); both are up to a few millimeters thick. The aragonite precipitated chemically from the lake, while the detritus laminas, composed mainly of calcite, quartz, dolomite and clay, which are the erosion products from the Dead Sea rift surroundings.

Lake Lisan evolved through frequent water level fluctuations, which reflected the regional hydrological and climatic conditions. The limnological history of the Lake Lisan appears to reflect the global climatic conditions in the Northern hemisphere. Cold periods in the North Atlantic followed by fluvial conditions in the drainage region of the lake, while warmer conditions in the North Atlantic correlated to dryer condition in the region (Stein, 2001). Bartov et al. (2004) show that during that period water-level fluctuated between 160 to 370m below mean sea level (bmsl). During that period the water level was always higher than 380m bmsl, indicating a large water contribution to the region.

^{14}C dating indicates that the Lisan Formation started accumulating about 63,000 yr B.P., with water level up to 270 m bmsl. The upper part of the Lisan Formation, the aragonite-rich White Cliff Member, started accumulating about 36,000 yr B.P. with sedimentation rate of 0.8-0.9 mm/yr (Kaufman et al., 1992).

The Lisan stage comes to an end earlier than 18 ka and perhaps somewhat later. The retreat of the lake and the subsequent dehydration of the Dead Sea created deep (up to 40m) canyons exposing the formation, allowing us to investigate the layers closely.

1.3.4 Seismic behavior along the Dead Sea basin

Paleoseismic studies of the Lisan Formation reveal a 50,000-year of recorded seismic activity along the Dead Sea transform (Marco et al., 1996). Indeed, the Dead Sea was tectonically active throughout the Pleistocene, and the delicate stratification of the Lisan Formation acted as a natural seismograph which recorded this activity in the form of various types of seismites such as: faults, folds, breccia and other geological features. Marco et al. (1996) show that earthquakes of M≥5.5 took place in clusters of time interval ~10,000 years followed by quiet periods of similar length.

The largest reported magnitudes along the Dead Sea fault are of the order of 6.5-7.5 (Klinger et al., 2000). A minimum of 10 such earthquakes have occurred along the Jordan Valley in the past 2000 years (Ben-Menahem, 1991). Three earthquakes of large magnitude were instrumentally documented over the last century, occurring in 1927, 1956 and Aqaba 1995. Our remaining knowledge of historical earthquakes is compiled from data from different historical documents and their interpretations along with correlations to archeology. The frequency-magnitude relation was calculated to be $\log N = 3.10 - 0.86M$ (Marco et al., 1996).

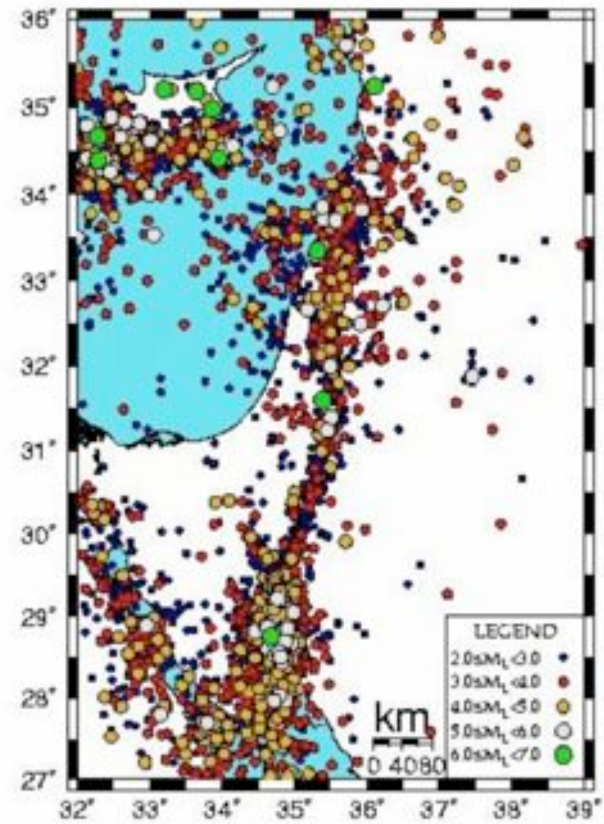

Figure 2 Map of earthquakes epicenters of magnitude <2 since 1900.

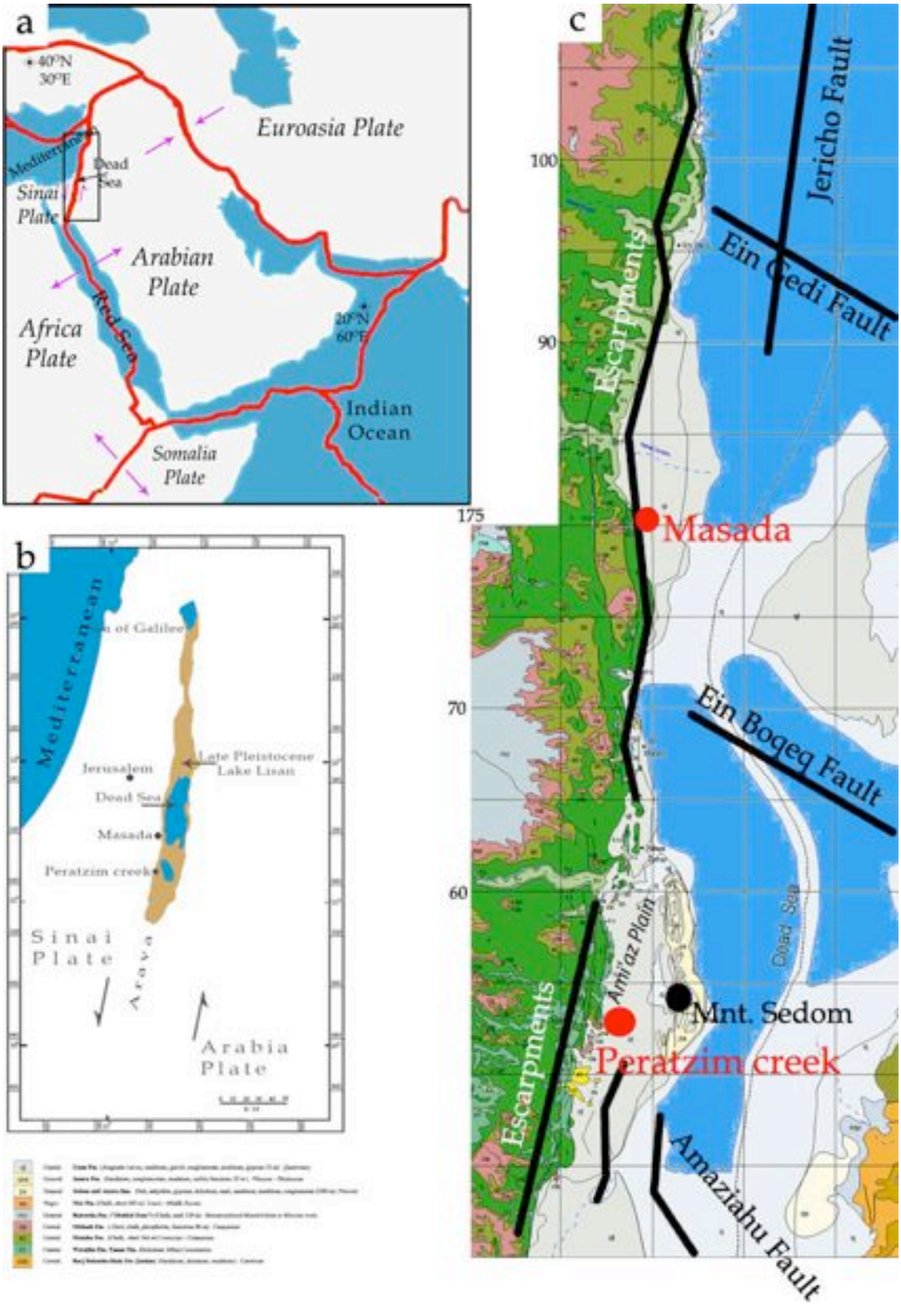

Figure 3 a) Plate tectonic setting of the Middle East. Red lines mark plate boundaries, arrows show relative movements. b) Location of measurement sites Masada and Peratzim Creek. C) Geological map of the research area. Active faults marked with black lines**.** Red circle marks the locations of M1 (Masada) and PZ1 (Peratzim).

1.4 The study areas

Two main sites studied in this research are: the M1 sedimentary section east of the Masada archeological site, and the (PZ1) Peratzim creek. Both sections are well stratified (Figure 4) and contain various types of folds.

Figure 4 Thin laminae of the Lisan Formation in the Masada study area

1.4.1 Masada

We studied the exposed late Pleistocene sediments in the Masada Plain, which consist of the overlying Lisan Formation. The study area is located 2 km east of the Masada archeological site (Figure 5) that was damaged by strong earthquakes. The base of the Lisan Formation is 374 mbsl, and the formation is approximately 30 m thick.

1.4.2 Peratzim Creek

The Peratzim Creek (PZ1) is located at the *Ami'az Plain* west of *Mount Sedom*. It is a bright and flat region around 6 km^2 located at 31º4′41″N, 35º22′10″E (Gilead and Karnieli, 2004). The elevation of the site ranges –260 to –270m bmsl.

Figure 5 Left, the Lisan Formation exposed in a creek at the Masada plain. Right, the Peratzim Creek. For locations, see Figure 2.

1.5 Seismogenic features in the Lisan Formation

Small ravines that flow to the Dead Sea expose the Lisan Formation through Peratzim creek and the Masada Plain up to 40m deep. These sites contain more than 50 kyrs of paleoseismic record extracted from the 70 – 14 ka lacustrain sediments of the Lisan Formation (Begin et al., 2005b). The formation includes various types of features that were interpreted as seismites: breccias[2], billow-like folds, dykes and faults. We present each of the seismogenic features that can be found in the Lisan Formation.

1.5.1 Breccias

Marco et al. (1996) presented three columnar sections of the Lisan Formation; one in Masada and two sections, 2 km apart, in the Ami'az Plain. Each section contains ~30 breccia layers. Breccias are well-blended sediment units that were formed by vigorous shaking and liquefaction that disturbed the stratification.

1.5.1.1 Character of the Breccias

The breccia layers can be easily distinguished as blended and mixed homogeneous in contrast to the well-laminated sediments of the formation (Figure 8). They are typically a few centimeters thick, but may also be several millimeters. The lateral extent of individual layers is in the order of hundreds of meters. The seismites observed near Masada are consistently thinner than the ones in the Ami'az plain, but no solid explanation has yet been found (Begin et al., 2005a).

1.5.1.2 Stages of formation

The breccias are the product of liquefaction. As pore water escapes and breaks into the upper sediment through the disrupted sediments, the latter becomes fluidized and subsequently blends and mixes. Agnon et al. (2006) suggest the following five stages of the formation of breccias:

1. Laminated mud is deposited over an older compact laminate.
2. The sediment layers are disrupted and deformed by ground and water column shaking. Within this stage the pressure of pore fluids in the sediments exceed the confining pressure of the overlaying lake water, resulting in the liquefaction of the sediments.

[2] Breccias: Seismite layers consisting of mixture of fragmented and pulverized laminae.

3. The top layers of the sediments are disrupted, laminae are torn, and the liquefied mass is suspended into the lake.
4. The suspended mud settles and forms a layer that partly fills the local relief.
5. Continual deposition covers the intraclast breccias and residual topography.

Generally speaking the formation of seismites mostly involves seismic energy with possible contribution of gravitational energy. The sediments of the Lisan Formation were deposited on a flat horizontal surface; therefore gravity would not have contributed to sliding and there is no evidence that gravitational waves were created within the Dead Sea deposits. Recent studies (Heifetz et al., 2005) show that the thickness of the breccias might relate to the local earthquake intensity.

1.5.1.3 Liquefaction

Liquefaction is a process by which loose water-saturated sands behave like liquids when shaken forcibly. In a steady state, water fills the pore spaces between the grains. As strong shaking moves the grains apart the soil behaves like liquid slurry (Figure 6). Buildings can sink and collapse swiftly during the few seconds of ground shaking over liquefied ground. Liquefaction of sand may occur near the epicenter of magnitudes as low as 5 or 4.6, but a quantitative analysis based on observations indicates that sand liquefaction is more characteristic at greater magnitudes.

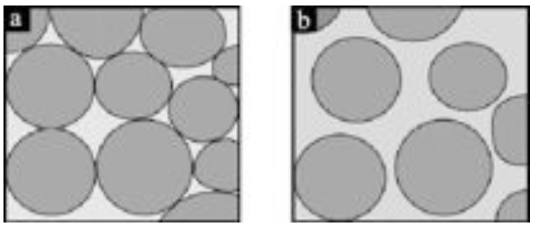

Figure 6 Illustration of liquefaction. a) Water-saturated sediment. Water fills the pore space between grains. Friction between grains holds sediments together. b) Liquefaction. Water completely surrounds every grain and eliminates all grain-to-grain contact. Sediment flows like fluid.

1.5.1.4 Breccias, liquefaction and earthquakes

The fact that breccias formed at the water-sediment interface makes them excellent recorders of earthquakes. Ken-Tor et al. (2001) identified seismites in the Holocene Ze'elim Terrace exposed on the shores of the Dead Sea, east to Masada. The sediments consist of laminated detritus and aragonite, similar to that of the Lisan Formation. Radiocarbon dating of organic remains indicates that the ages of the seismites correlate with the historically documented earthquakes of 140 and 31 B.C and 33, 419, 1212, 1293, 1834 and 1927 A.D. According to Ken-Tor, the seismites of the Ze'elim Terrace indicate M>5.5 earthquakes with average recurrence interval of ~100-300 years, and represent slip events on different faults in the DSB. In addition to magnitude, the subtle bottom topography as well as variables such as peak particle velocity, duration of motion, ground acceleration, and local properties of the medium influence the thickness of breccia layers.

Marco et al. (1996) studied the temporal distribution of earthquakes during Lisan time along three detailed columnar sections of the Lisan Formation. They present a detailed analysis of the distribution of breccia layers. They indicate ~30 breccia layers during the past 60,000 years, each layer representing a strong earthquake with a magnitude >5.5 (Agnon et al., 2006; Begin et al., 2005b; Marco and Agnon, 1995; Marco et al., 1996).

1.5.2 Dykes

Clastic dykes are exposed in the Ami'az Plateau, west side of Dead Sea. The vertical dykes that cross the Samra and Lisan Formation are seen on the walls of canyons of the Peratzim Creek and Masada Plain. In the Peratzim they are typically up to 0.4 m wide, ~50 m high, and up to 1 km long, and arranged mainly in radial and tangential geometry (Levi et al., 2006). The Dykes are commonly filled with brown sand mixed with some fragments of the Lisan rocks. These structures are tied to the rise up of Mt. Sedom (Marco et al., 2002). They suggested that a salt diaper pushed the *Black Hill*, (a dome structure formed by the rise of an underlying salt diapir), upward and triggered fracturing around it. Analysis of anisotropy of the magnetic susceptibility (AMS) fabric reveals that the sediments within the injection dykes were emplaced by flow (Levi et al., 2006). Furthermore, they suggested that most of the clastic dykes in the Ami'az Plain are associated with fluidization triggered by strong earthquakes along the DST, after the depositional of the Lisan Formation (i.e., after 15ka).

1.5.3 Faults

A north-tending fault zone was found near Masada (described in chapter 1.3.2.1). These faults rapture the lake bed, forming subaqueous fault scarps. In addition to the fault scarps, a breccia layer was formed at the water-sediment interface on both sides of the fault (Marco and Agnon, 2005). The breccia layers were formed simultaneously to the slip event, according to its degree of consolidation with depth. Most of the fault planes strike north, paralleling the main graben faults and morphological trends. Dips are 40^o to 70^o eastward and westward, with normal displacement as much as 2m.

1.5.4 Billow-like folds

The billow-like folds (Figure 8) are the subject matter of this research. The folds are exposed within the Lisan Formation at various sizes with amplitudes from a few millimeters up to ~1 m. The folds vary in shape; from small curved folds to well developed vortices. Some of the folds are characterized by low *curvatures*[3] whereas others show high value curvatures. The folds are in the form of waves or billows in a large variety of deformation stages. They may appear as linear and non-linear coherent billows, single or sequentially folded, one after the other at the same lamina-packet. The folds preserve a constant orientation of the axes along the deformed packets (Figure 9).

Some of the folds exhibit fractal qualities (Figure 7). It seems that the main lamina-packet can be deformed to exhibit much smaller features, similar in shape to the main fold, only much smaller. Ramsay and Huber (1987) attribute heterogeneous **shear mechanism** that is particularly strong at the upper and lower contacts of the folded packet. Fractal behavior is commonly observed in turbulent flows. This behavior can be defined by the fractal dimension of Hausdorff: the turbulent structures are assumed to be self-similar and to lie on fractal set of definite dimension (Lesieur, 1997).

Most of the large folded laminas (amplitude > 10cm) are usually accompanied with breccias either on top or below the folded layer-packet. In most cases the layers stratified underneath the folded-packet structure remain intact. This fact is very important for the understanding of the mechanism. The fact that some of the laminas deform and others do not implies that the driving mechanism is influenced by the characteristics of the laminas according to the depth. Obviously the laminas at the bottom were affected by the same driving mechanism as the one that operated and folded the top lamina-packet, but did not suffer any deformation.

[3] The curvature, C, of a line at any point is defined as the reciprocal of the radius of the curvature: C=1/r. Thus a straight line has an infinite radius of curvature and a zero curvature.

Figure 7 Fractal features in fold lamina-packets. Perazim creek. The square at the middle of the figure is magnified at the upper right corner. Notice the small scale features similar to the main fold geometry.

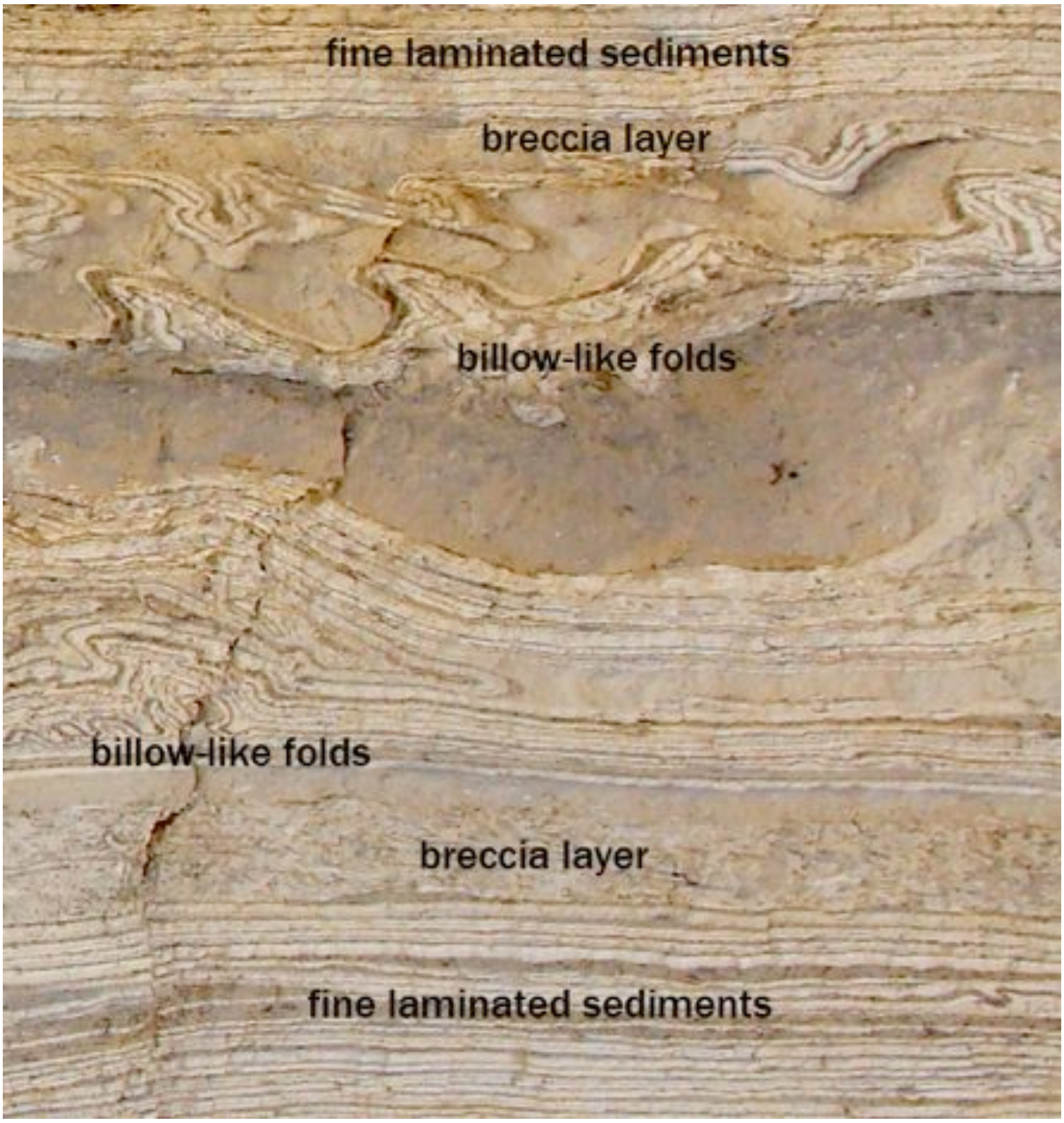

Figure 8 Patterns of billow-like folds within the well-stratified horizontal lamina-packet of the Lisan Formation. Mark the fixed orientation of the curvature of the folds along the laminas. Also presented in the figure are the well-mixed breccias in contrast to the fine laminated sediments that remain intact underneath the deformed structures. This lamina-packet may exhibit deformation from two or more seismic events.

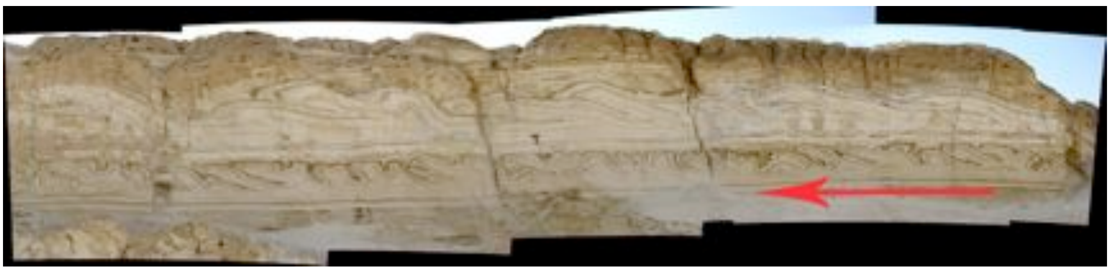

Figure 9 Panoramic view of large-scale folded sediments from Perazim creek. Clear orientation preserved through continues folded sediments along tens of meters, marked by the red arrow. Photographed and composed by Shmuel Marco.

1.6 Hypothesis

Heifetz et al (2005), have already suggested that the billow-like folds of the Lisan Formation may have been induced by shear instability during relative sliding, e.g. Kelvin-Helmholtz instability. In this research we investigate the feasibility of such mechanisms using a hypothesis that suggests an order of occurrences that involves KHI by the following (Figure 10):

- The sediments at the bottom of Lake Lisan were stably stratified horizontally. The process of sedimentation forms a light layer of sediments above older denser layers at the bottom of the lakes.
- Resulting from large intensity earthquakes (M>5.5), and due to the preservation of momentum and the influence of the pressure gradient force, the light and less dense upper layers slide horizontally on top of the heavier denser layers. As earthquakes occur, liquefaction may lower the density of the top layers, increasing the density gradient profile.
- Small-scale perturbations evolved due to the shear instability at the interface of the light and heavy layers having different densities.
- The velocity difference induces shear instability between the layers, which increases the small perturbation and folds the sediments to small billows. The billows are tilted toward the flow direction while deeper sediment layers remain intact and do not experience any deformation.
- Reduction of porosity of the sediments freezes the process.

Along this research we investigate different aspects of the presented hypothesis, and the feasibility of several other mechanisms.

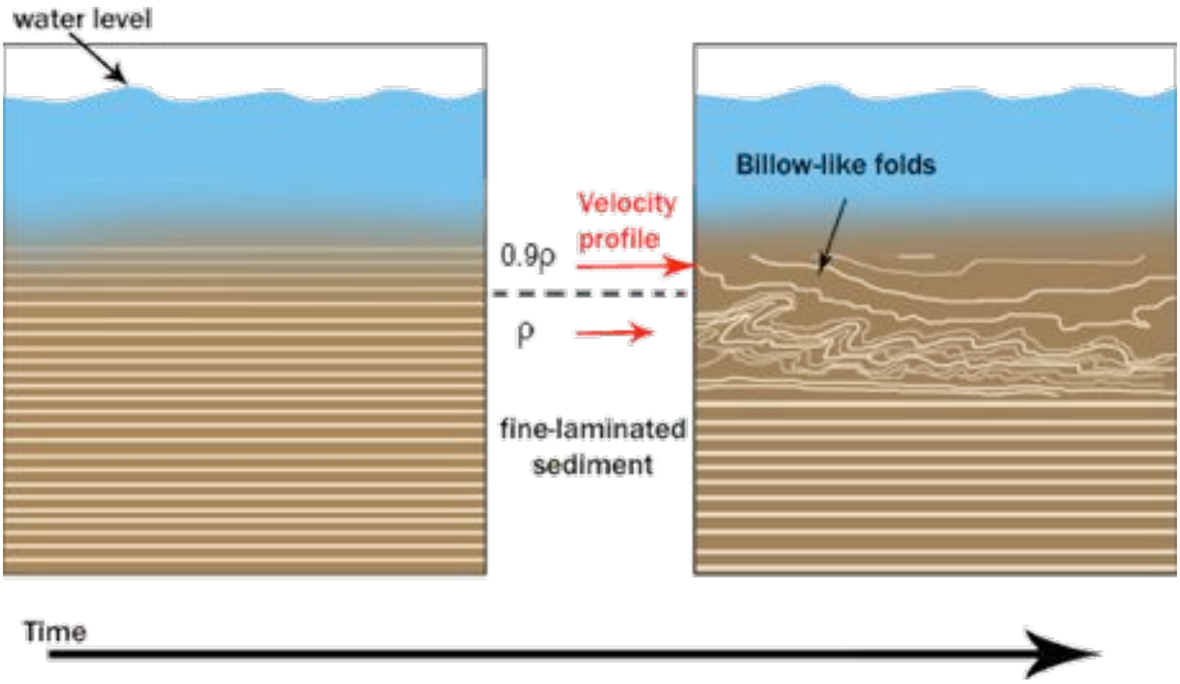

Figure 10. Left: before an earthquake, laminated sediments stratified horizontally at bottom of Lake Lisan. Right: After an earthquake, deformed structures in the shape of billows created as a result of the ground shaking. In response to shaking the less dense layers slide on top of the relatively heavy layers at the bottom, creating velocity shear that allows small perturbations to grow by the conditions of instability, while deeper laminas remain intact.

2 BACKGROUND CONCEPTS

In this section we introduce the concepts of fluid dynamics used in this study, followed by a skeleton treatment of the phenomenology of turbulence, the Kolmogorov theory of turbulence flow and the application of this theory to this research. The final sections of this chapter are dedicated to the theoretical introduction of Kelvin-Helmholtz Instability.

2.1 Equation of motion: The Navier-Stokes equation

All forms of flow in nature can be described by a set of three equations of motion: The Navier-Stokes equations (NSE). The NSE is a set of differential equations describing the motion of fluid substances such as liquid or gas. The most general form of the NSE is the equation of conservation of mass, momentum and energy.

$$\rho\left(\frac{\partial\overline{V}}{\partial t}+\overline{V}\cdot\nabla\overline{V}\right)=-\nabla P+\mu\nabla^2\overline{V}+f \qquad (1)$$

V is the vector of the fluid velocity at time t, P is the pressure, μ is the viscosity and f is other forces such as gravity or centrifugal force.

2.2 Incompressibility

Throughout the numerical model, we only consider incompressible fluids. For our present purposes it is assumed that the fluid density ρ always remains constant, and the equation of continuity (which expresses the conservation of mass)

$$\frac{\partial\rho}{\partial t}+\nabla\left(\rho\overline{V}\right)=0 \qquad (2)$$

takes the form

$$\nabla\cdot\overline{V}=0 \qquad (3)$$

2.3 Viscosity and Newtonian Fluids

Viscosity is the measure of resistance arising from the attractive forces between the molecules of the fluid to a shear. All fluids have some resistance to shear and a fluid that has no resistance is called ideal fluid or inviscid fluid. Isaac Newton (1642-1727) postulated that in the case of laminar flow (whereby fluid particles move in parallel lines), the shear stress τ on an interface tangent to the direction of the flow is proportional to the change of velocity in a direction normal to the interface. Mathematically this is stated as: $\tau \propto \frac{\partial V}{\partial n}$. We can describe this relationship as Taylor series about a point y=0:

$$\tau_{yx} = f\left(\frac{\partial V_x}{\partial y}\right) = f(0) + f'(0)\frac{\partial V_x}{\partial y} + f''(0)\frac{1}{2}\left(\frac{\partial^2 V_x}{\partial y^2}\right) + f'''(0)\frac{1}{6}\left(\frac{\partial V_x}{\partial y}\right)^3 \quad (4)$$

We can neglect the third derivative and demand that the function to be coupled (changes in the direction of the stress changes the direction of velocity), and so we obtain:

$$\tau_{yx} = \mu \frac{\partial V_x}{\partial y} \quad (5)$$

An infinitesimal area of the flow is chosen as shown in Figure 11. The fluid velocities at points along the normal to the interface are plotted against the horizontal abscissa, thus forming a velocity profile. The slope of the profile toward the *n* axis at the position corresponding to the area element is the value $\partial V / \partial n$, which is related as stated above to the shear stress τ (H.Shmase, 1962).

μ Is the coefficient of viscosity, having the dimensions [kg m^{-1} s^{-1}]. Related coefficient is the kinematic viscosity - ν, having dimensions [m^2 s^{-1}]. All gases and most liquids are Newtonian fluids and hence behave according to the above equation for the conditions outlined.

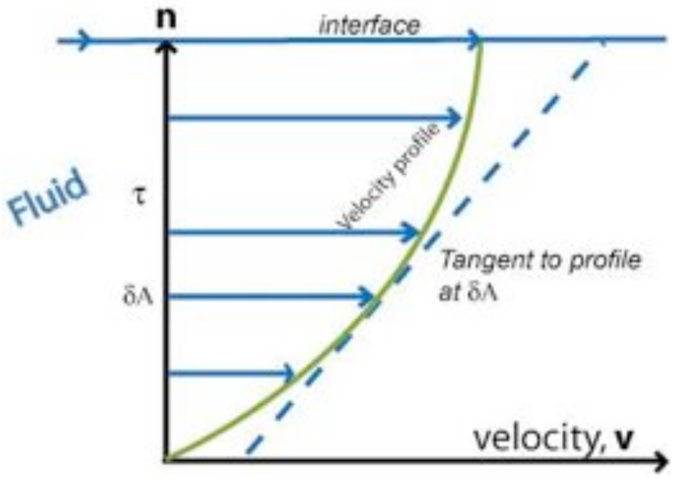

Figure 11 Illustration of a velocity profile for Newtonian fluid flow. Blue lines represent the velocity vectors. Dashed line represents the tangent to the velocity profile at a distance of δA from interface.

2.4 Waves parameters

The simplest type of wave solution, for homogeneous medium, is the plane wave:

$$\phi(x,t) = \mathrm{Re}\left[Ae^{(i(kx-\omega t))}\right] \quad (6)$$

Where ϕ is field variability e.g. pressure, velocity. A is the wave amplitude, k is the wave number, and ω is the wave frequency. The wave phase $\theta = kx - \omega t$, where at any fixed point in space, the rate of change of phase with time

$$\frac{\partial \theta}{\partial t} = -\omega \quad (7)$$

2.4.1 Wave number - *k*

The NSE that describes the dynamics of flow of viscous fluids can be translated to a spectral form in which the variables are the wave numbers for vortices of various sizes. The wave number k of a vortex of spatial dimension L is given by $k = 2\pi / L$. The spectral form of the NSE indicates that the energy can be transferred from two wave numbers, k_1 and k_2 to a wave number k_3 only if $k_3 = k_1 + k_2$. This is called the *Selection Rule*. Let us assume that the wave numbers of interacting vortices can be approximately equal, in which case $k_3 \cong 2k_1$. This is the type of interaction by advection term $v \cdot \nabla v$ of the NSE. If we describe the local motion of an eddy by $v_x \sim \sin(kx)$, we get

$$\sin(kx)\partial_x \sin(kx) = k\sin(kx)\cos(kx) = \frac{1}{2}k\sin(2kx) \quad (8)$$

This presents the concept of energy dissipation according to Kolmogorov's $k^{-5/3}$ law (Manneville, 2004).

2.4.2 Energy

The total energy in a system is composed by the total energy in wave number magnitude *k*.

$$E = \int E(k)dk \quad (9)$$

The energy that interests us is the kinetic energy that expresses the transformation and evolution of the system.

$$\int_0^{\infty} E(k)dk = \frac{1}{2}\int |\hat{u}|^2 (k)dk \quad (10)$$

Kolmogorov’s analysis deduced that the energy density should depend only upon the wave number *k* and ε, the rate of energy dissipation:

$$\varepsilon = 2v\int_0^{+\infty} k^2 E(k)dk \quad (11)$$

At high Reynolds number, between the scale in which the energy is 'produced' and the small scales at which it 'destroyed', lies a range of scales at which neither process is very important. This is called the *inertial range*, a concept introduced by Kolmogorov (1941) and discussed in the next section.

2.4.3 The energy of a harmonic wave

In order to obtain the amount of energy carried by the folded laminas, we address the geometrical structures as harmonic waves with a typical amplitude and wavelength. Although many of these folded beds are not pure linear harmonic wave functions, we measure these billow-like structures as such.

The simplest case of a propagating harmonic wave is represented by the equation:

$$y(x,t) = A\sin(kx - \omega t) \qquad \textbf{(12)}$$

Kinetic energy is represented by the equation:

$$KE = \frac{1}{2}mv^2 \qquad \textbf{(13)}$$

The kinetic energy, KE, of a small string segment dx is found from the vertical velocity of the string $\partial y / \partial t$

$$KE = \frac{\rho}{2}\left(\frac{\partial y}{\partial t}\right)^2 dx \qquad \textbf{(14)}$$

The mass of the string segment is $m = \rho dx$.

For a length of string in a case of harmonic wave, the kinetic energy

$$KE = \int \frac{1}{2}\rho A^2\omega^2 \cos^2(kx - \omega t)dx \qquad \textbf{(15)}$$

Since the average value $\int_0^\lambda \cos^2(\omega t - kx)dx = \frac{1}{2}$, for continuous harmonic wave the average KE per unit length is $\overline{KE} / meter = \frac{1}{4}\rho\omega^2 A^2$

We can define the average potential energy, PE, in a segment dx as,

$$PE = \frac{\tau}{2}\left(\frac{\partial y}{\partial x}\right)^2 dx \qquad \textbf{(16)}$$

τ is the tension of the string segment. The energy of a traveling wave is characterized by the averaged kinetic energy and potential energy over a wavelength.

Similarly, the potential energy averaged over a wavelength is

$$PE = \frac{\tau}{2\lambda}\int_0^\lambda \left(\frac{\partial y}{\partial x}\right)^2 dx = \frac{\tau A^2 k^2}{2\lambda}\int_0^\lambda \sin^2(\omega t - kx)dx = \frac{A^2 k^2 \tau}{4} \quad (17)$$

$$k = \frac{\omega}{v_i}, v_i = \left(\frac{\tau}{\rho_i}\right)^{1/2} \quad (18)$$

$$PE = \frac{A^2 \omega^2 \rho}{4} \quad (19)$$

the same as the kinetic energy. Hence, the total energy transport, averaged over a wavelength, is the sum of the potential and kinetic energies:

$$E = PE + KE = \frac{A^2 \omega^2 \rho}{2} \quad (20)$$

Therefore, the energy of a single wave is proportional to the square amplitude and the radial frequency of the wave. This is the left side of the equation of the *equi-partition* of the inertial stage of the energy dissipation of the Kolmogorov power law.
In this study we represent the energy of each billow-like deformation by the square amplitude of its wave. The method of measurement will be presented in the next chapter.

2.5 Turbulence, instability and shear flows.

In this chapter we present some of the basics of turbulence flow with an attitude to instability in cases when shear flow is involved.

2.5.1 Turbulent flow

The turbulent nature of fluids plays a major role in everyday life as it influences the velocity distribution and shear stress in a flow. We watch the behavior of smoke coming out of a cigarette or evolution of weather patterns and relate them the characteristics of turbulence.
We know empirically two modes of fluid flow: the laminar and turbulent mode. In 1883 the English mathematician and physicist Lord Reynolds observed the nature of fluid flows and conducted one of the most important experiments in fluid dynamics. By inserting dye into a flow in a long straight pipe he characterized the streamlines of the dye with respect to the velocity of the flow, the kinematic viscosity and another parameter that is a characteristic length (Figure 12). He showed that in low velocities the dye line remains stable and preserves a pattern steady over time (the laminar stage). As he increased the flow velocity, the dye line became unstable and highly distorted (turbulent stage).

Reynolds expressed and characterized the flow by a dimensionless number – Reynolds number. The Reynolds number can be seen as a measure of the importance of the viscous terms versus the inertia terms in the equations of motion. If a typical length-scale (L) and a typical velocity-scale (U) are substituted and the inertia terms are divided by the viscous terms the Reynolds number is obtained.

$$\mathrm{Re} = \frac{\dfrac{\partial \rho u_i u_j}{\partial x_j}}{\nu \dfrac{\partial^2 u_i}{\partial x_j^2}} = \frac{\dfrac{U^2}{L}}{\nu \dfrac{U}{L^2}} = \frac{UL}{\nu} = \frac{UL\rho}{\mu} \qquad \textbf{(21)}$$

Reynolds found that the number value of transition to turbulence is in the order of 2000.
The transition to turbulent is still ambiguous. It can be said that a flow becomes turbulent as it crosses the critical non-dimensional parameter Reynolds number (Re). For instance, the critical Re for a flow above a half infinity plate is ~500,000. however, a comprehensive understanding of shear instability processes and their transition to turbulence has remained elusive due to an inability to quantify high Reynolds-number flow either via observational or numerical techniques (Werne and Fritts, 1999). Former numerical studies of KHI (Smyth, 2004; Werne and Fritts, 1999; Werne and Fritts, 2001) use Reynolds number values above 500 in order to achieve satisfactory shear instability.

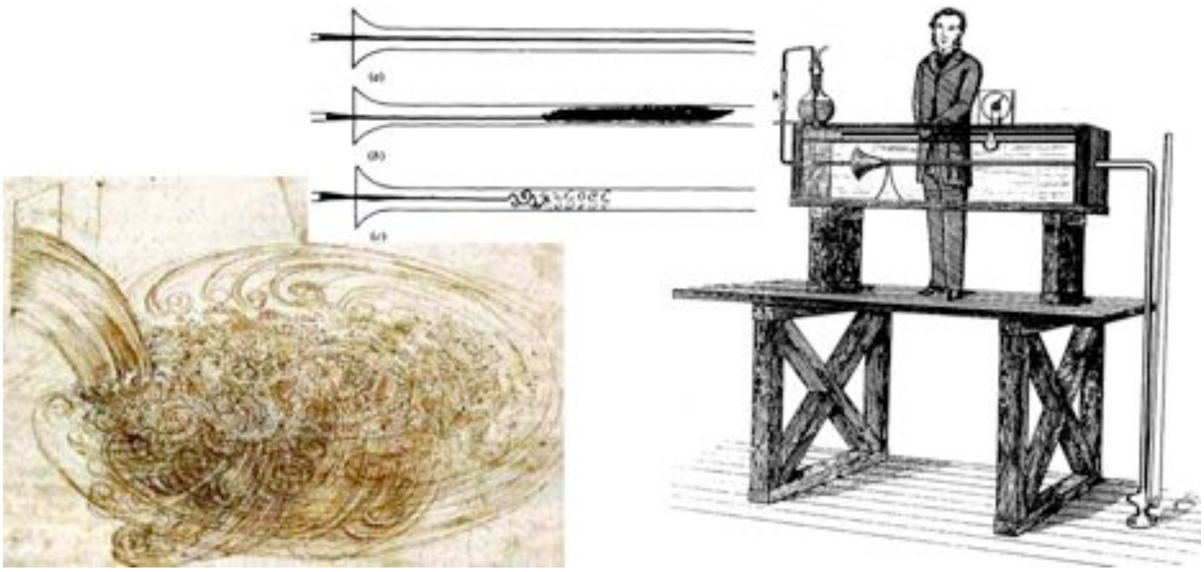

Figure 12 Turbulence. Form left to right. Painting by Leonardo da Vinci (1452-1519). Turbulent flow. Leonardo recognized that turbulence involves a multitude of eddies at various scales. The results from the Reynolds experiment; three stages of flow: Laminar, unsteady and turbulent. On the right, the Reynolds experiment set up.

2.5.2 Kolmogorov’s theory

The theory of Kolmogorov is one of the most famous theories of isotropic turbulence. This theory was published in 1941 by Andrei Kolmogorov (Kolmogorov, 1941a; Kolmogorov, 1941b) one of the most famous Russian mathematicians. Since then numerous studies measuring the characteristics of turbulence have been carried out in natural media such as the ocean (Phillips, 1991; Smyth and Moum, 2000) and the atmosphere (Zilberman et al., 2008). The measurements have completely confirmed the theory put forward by Kolmogorov (Obukhov, 1983) (Figure 14).

What is the theory of Kolmogorov?

Kolmogorov predicted the amount of energy that is retained in a curtain vortex in a turbulent flow. An Energy spectrum of such vortices gives a distribution of turbulence energy in terms of wave number or inverse length scale. In the *inertial-range*, energy cascades to smaller scales according to a certain power law. This spectrum in such region has the form: $E(k) = C_k \varepsilon^{2/3} k^{-5/3}$ where C_k is the Kolmogorov constant and has a value of about 1.6. ε Is the *dissipation rate*, the rate at which energy is input at wave number k_i. This equation sets the right side of the equipartition equation:

$$\frac{A^2 \omega^2 \rho}{2} = C_k \varepsilon^{2/3} k^{-5/3} \quad \textbf{(22)}$$

2.5.2.1 "The Two-thirds law"

The theory is a dimensional prediction concerning either the second-order velocity function, or the kinetic energy and relates to the "two-thirds law". The law predicts that in every turbulent flow, “the mean square difference of the velocities at two points at a distance of r apart is proportional to $r^{2/3}$” (Figure 13). In other words we can say that the mean square velocity difference depends on the separation *r* and sometimes characterizes the strength of the turbulence.

The turbulent flow of a liquid consists of vortices from large to smaller magnitudes until the energy of motion will eventually dissipate and the motion will cease. The motion of a liquid is made of waves of different lengths (Figure 12); Kolmogorov asked the question, what is the share of energy carried by waves of a particular length?

In turbulent flow the factor that matters most is the transfer of energy from large eddies down to small eddies that dissipate the energy through the action of viscous forces. This energy transfer rate per unit has units of $m^2 s^{-3}$. Denoting the energy dissipation rate by ε

and assuming that the mean square velocity difference depends only on this and the separation r, then the mean square velocity difference must be proportional to $\varepsilon^{2/3}r^{2/3}$ in order to have units of m^2s^{-2}. In association with kinetic energy, the distribution of energy is proportional to $\varepsilon^{2/3}k^{-5/3}$. k is the wave-number and is proportional to the invert of the eddy scale. The Kolmogorov's law is not valid for any scale of motion: under k_i the spectrum will be influenced by long-range forcing interactions. Above a sufficiently high wave number k_d, called Kolmogorov wave number, the viscose dissipation will dampen the velocity perturbation. The order of magnitude of this wave number can be obtained by this equation:

$$k_d = \left(\frac{\varepsilon}{\nu^3}\right)^{\frac{1}{4}} \qquad \textbf{(23)}$$

For k > k_d , the energy spectrum will rapidly drop to negligible values. This range is the dissipation range.

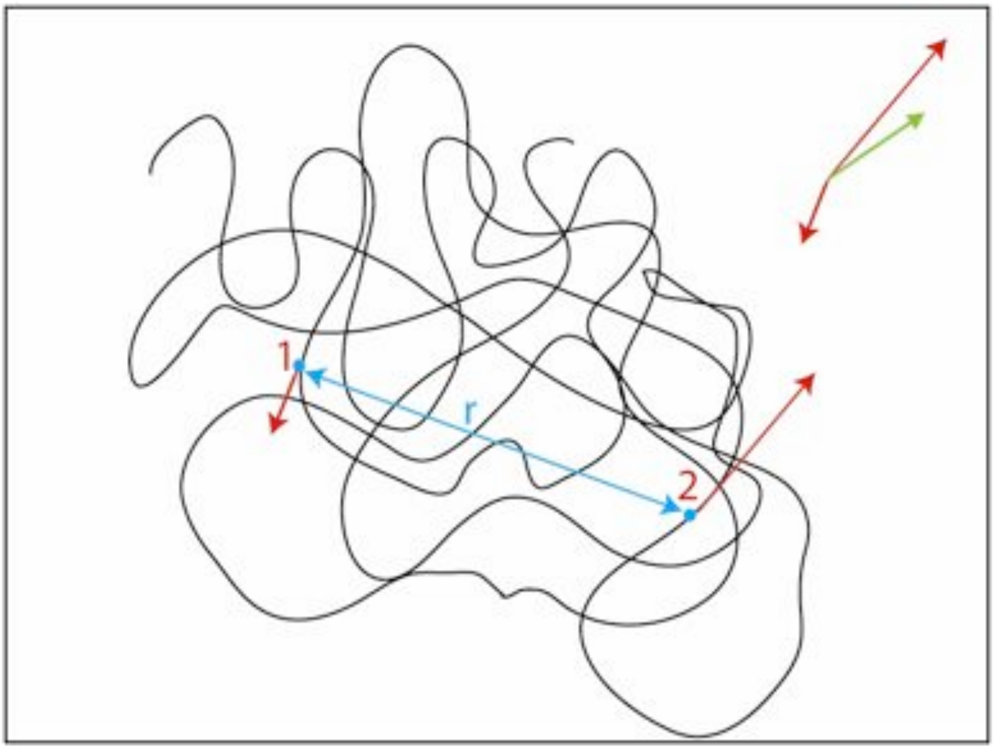

Figure 13. Two particles at a distance of r apart in a turbulent flow (black line shows the path of the particles), have different velocities, indicated by the red arrows at position 1 and 2. The green arrow at the upper right part of the figure depicts the velocity at position 1 minus velocity at position 2. The average of the square of the green velocity is proportional to $r^{2/3}$

2.5.2.2 Dimensional Analysis

The Kolmogorov theory assumes that the energy spectrum at wave numbers greater than k_i depends only on ε and k. A dimensional analysis based on the Vaschy-Buckingham Π-theorem for these variables yields:

$$E(k,\varepsilon) = C\varepsilon^{2/3}k^{-5/3} \quad \textbf{(24)}$$

One seeks an expansion of the spectrum of the form: $E(k) = G(\varepsilon,k) = \sum_{\alpha,\beta} k^{\alpha}\varepsilon^{\beta}$. We look for exponent α and β such that $k^{\alpha}\varepsilon^{\beta}$ has dimension of kinetic energy spectrum. If [L] and [T] are dimensions of space and time respectively, we obtain:

$$\begin{aligned}
[k] &= L^{-1} \\
[\varepsilon] &= L^{2} \cdot T^{-3} \\
[\nu] &= L^{2} \cdot T^{-1} \\
[E] &= L^{3} \cdot T^{-2}
\end{aligned}$$

Dimensional compatibility is required. We will use the Buckingham π theorem.

$$\begin{aligned}
&E = C \cdot k^{\alpha} \cdot \varepsilon^{\beta} \\
&L^{3} \cdot T^{-2} = C \cdot L^{-\alpha} \cdot L^{2\beta} \cdot T^{-3\beta} \\
&L : 3 = -\alpha + 2\beta \\
&T : -2 = -3\beta \\
&thus \\
&\beta = 2/3, \alpha = -5/3
\end{aligned}$$

Thus the Kolmogorov's energy spectrum is: $E(k,\varepsilon) = C\varepsilon^{2/3}k^{-5/3}$

2.5.2.3 The Energy spectrum

Kolmogorov had proven that the energy that is added to a system at a large scale "break down" into smaller and smaller structures. This is called the energy spectrum and it is divided into three main ranges:

Energy containing range. This stage contains most of the energy; it also called the anisotropy range. The shape of E(k) depends on the particular physical regime and mechanism of turbulence generation.

Inertial range L0>L>Ld. At intermediate scales the advection terms dominates and the spectrum shape is $k^{-5/3}$.

Dissipation range. Smaller then L_d, the spectrum falls due to the disappearance of the kinetic energy into molecular collisions and heat. The spectrum is steeper than any power law, often taken the shape $E(k) \propto k^{\alpha} e^{-ck/k_d}$

The transfer from energy from large eddy to the smallest eddy and the dissipation of energy into heat is called the energy cascade. The length and time scale where the dissipation takes place is indicated as the Kolmogorov scale. And the dissipation rate is given by $\varepsilon = \frac{dissipated(kinetic)energy}{time} \sim \frac{u^3}{l}$

In this research we examine the properties of the flow in the inertial range.

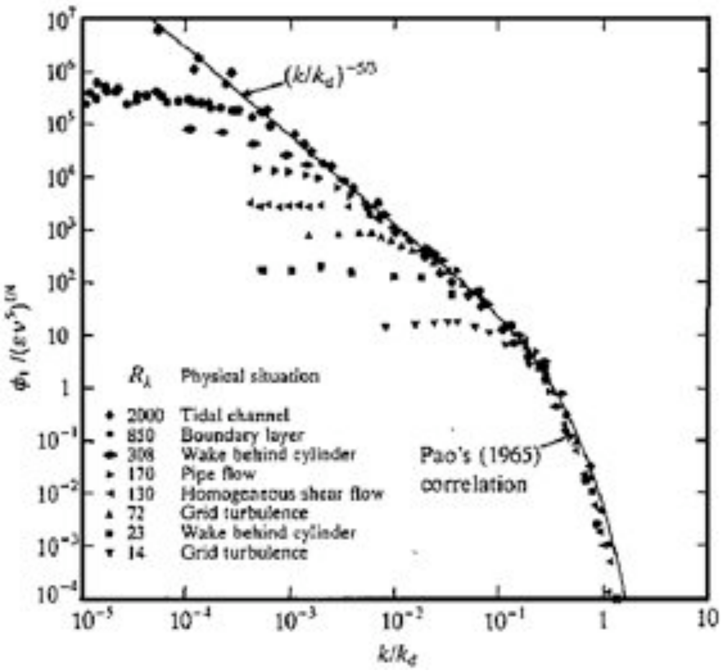

Figure 14. Presentation of the Kolmogorv power law. Measured is the one-dimensional spectra for a wide range of Reynolds numbers and physical situations (note that both wave-number and spectra have been scaled by the appropriate Kolmogorov variables) (McComb, 1995).

2.5.3 Instability

Instability is a signal that grows in amplitude with time without any external forcing. They lead to disturbances that have important tracers of momentum fluxes (such as in weather forecasting), and are an important phase for generating turbulence. Instabilities are responsible for much of the time-dependent small-scale motion in oceans and the atmosphere, and mostly involve density stratification and rotation. In fact, without any inducing force the viscosity will cause such disturbances to decay. In order that an infinitesimal perturbation can grow to become a large amplitude, they require a source of energy, which come from the basic state.

Shear instability - Velocity shear in the basic state provides a source of vorticity for instability. Instability extracts kinetic energy from the large-scale flow.

Convective instability – Large-scale unstable density gradient (heavier fluid above lighter fluid) provide a source of potential energy for instability. Instability converts this potential energy to turbulent kinetic energy.

Baroclinic instability – Baroclinic instability contains elements of both of the above: energy is extended from a large-scale shear, and a large-scale potential energy is reduced. This condition is possible wherever there are large-scale horizontal density gradients with geostrophic imbalance currents.

2.5.4 Kelvin Helmholtz instability

This chapter is dedicated to the introduction of the Kelvin-Helmholtz instability. We present quality description of the acting forces and the presetting configuration of the system. The mathematical formulation is of no interest of this research therefore we have decided not to include it as such.

2.5.4.1 General overview

Natural bodies of fluid such as the atmosphere, oceans and lakes are characteristically stably stratified: that is, their mean (potential) density decreases as one moves upwards, in most regions and for most time (Turner, 1973). When they are disrupted in any way, internal waves are generated and may take the form in typical Kelvin-Helmholtz billows. Kelvin-Helmholtz instability is a common feature turbulent phenomenon in nature which first described by Lord Kelvin (1871). This special instability frequently appears in oceanic measurements and observed in the atmosphere when a cloud layer breaks up into a string of billows (Figure 15). The observed vertical scale of billows is of the order of 5 to 20 m in oceans and up to 400 m in the atmosphere (DeSilva et al., 1996). KHI billowing appears as a series of rolled vortices separated by thin braids. The instability, created by the competition between large-scale shear and stable ambient density stratification, eventually gives rise to small-scale perturbations. Recently direct numerical simulation (DNS) studies helped considerably to understand this instability and the large-amplitude billows that emerge as a result (Smyth, 2003; Smyth, 2004; Zheng et al., 2004).

Figure 15 Natural KHI. a) Atmospheric Kelvin-Helmholtz instability patterns above the horizon, New Zealand. Conditions of strong stratification, humidity and shear provide development of such KHI clouds. Photographed by Mr. Attay Harkabi, January 1999. b) KHI patterns within the atmosphere of Jupiter as described by Bosak and Ingersoll (2002).

2.5.4.2 Conditions

Stratification and sheared fluid are crucial players in many geophysical flows. Key processes include shear instability and internal gravity wave breaking. The turbulence redistributes momentum, mass and constituents, taking on a critical role in defining the flow structure and stability (Werne and Fritts, 1999).

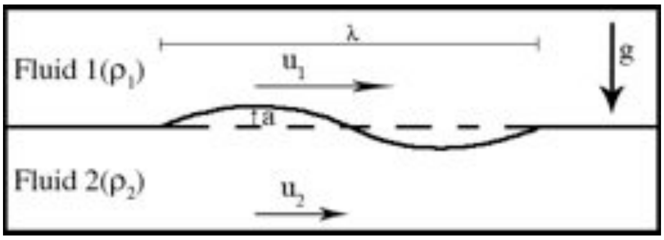

Figure 16 KHI configuration. Shear flow, density gradient, perturbation and gravity.

In general, this type of instabilities involves the interplay of at least two of the following forces:

Buoyancy force, acts due to the density gradient between the fluids. This can be characterized by $gl^3\Delta\rho$, where $\Delta\rho = \rho_1 - \rho_2$, g is the gravitational acceleration, and l is a typical dimension of the waves. In the common case of KHI in which the upper situated fluid is lighter than the lower situated fluid, the buoyancy force acts as a stabilizer. When the density gradient is reversed, the buoyancy force destabilizes the interface that may cause Rayleigh-Taylor instability.

Surface tension force, acts as a stabilizing force.

Bernoulli effect, change in the pressure acts on the interface, caused by a change in velocity. Such force depends on the difference in the velocity of the two streams $\Delta u = u_1 - u_2$, and characterized by $\rho(\Delta u)^2 l^2$, where ρ and l are characteristic density and dimension, respectively, of the flow.

2.5.4.3 Process and mechanism

Consider the basic flow of two incompressible fluids with different densities ρ_1 and ρ_2 horizontally stratified the lighter layer above the heavy one, in two infinite streams of different velocities u_1 and u_2 (Figure 16). The interface between the two layers appears as a vortex sheet with uniform vorticity while outside the sheet vorticity equals to zero due to the constant shear velocities. External or small scale perturbations at the interface may stimulate folding of the vortex sheet to a small billow or waveform.

The Bernoulli equation,

$$P_i + \rho g y + \frac{1}{2}\rho v_i = C \qquad (25)$$

sets the dependency between the dynamic pressure, velocity and hydrostatic pressure. We obtain that the higher local velocity of Fluid 1 decreases the pressure relative to the heavy and slower layer of Fluid 2. This implies an induced pressure difference at the raised perturbation that would increase the amplitude of the distortion, *a*. This amplification continues as long as the shear continues. Finally, vorticity rolls the growing amplitude creating a 'cat's eye' like vortex (Figure 17 a to f).

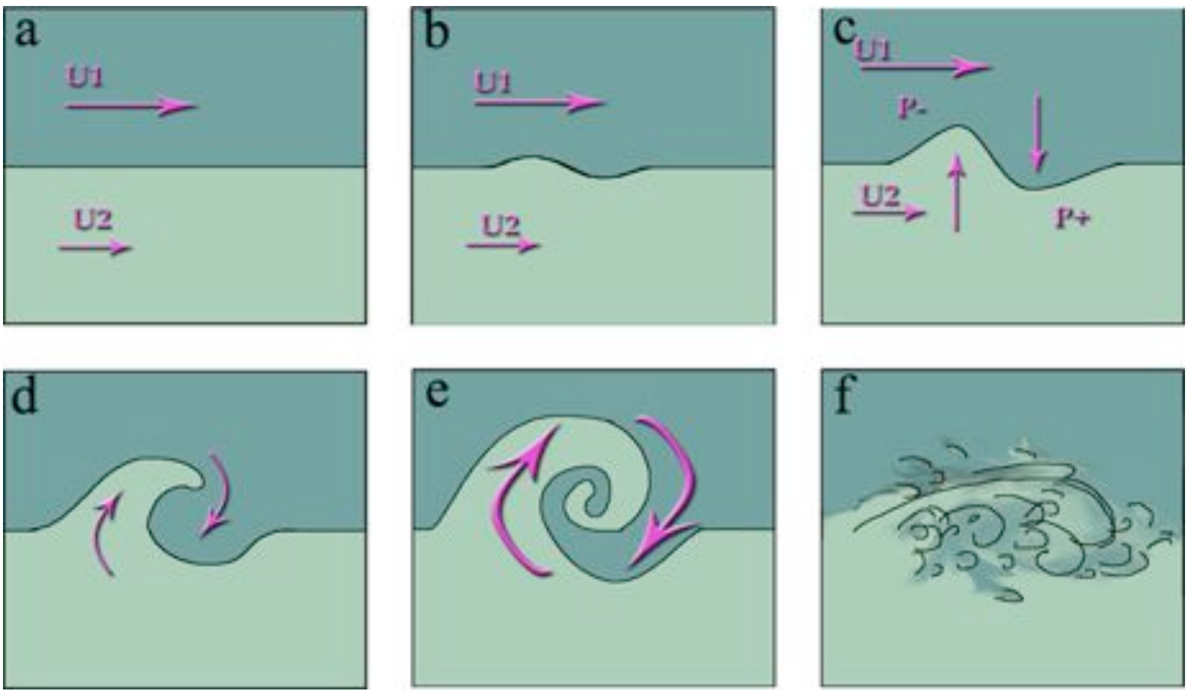

Figure 17 Illustration of stages of evolution of Kelvin-Helmholtz instability. a) Two horizontal layers in two horizontal parallel infinite streams of different velocities. The interface between the two layers appears as a vortex sheet with uniform vorticity, while outside the sheet it is equal to zero due to the constant velocities. b) An external perturbation may locally oscillate the interface between the layers. c) Amplitude grows due to the lower pressure at the upper layer. d) Vorticity rolls the grown amplitude and tilts it towards the direction of flow e) Full vortex stage - 'Cat's eye' f) Stage of collapse and full turbulence.

2.5.4.4 Anisotropic turbulence

The theory of Kolmogorov states that the energy of an isotropic turbulent flow cascades according to the -5/3 power law at the inertial range. In cases where the flow becomes directionally dependent, one must refer to the flow as an anisotropic flow. In our case, shear sets a clearly preferred direction. Properties of experimental KH billow show that the power law slope at low wave-numbers is close to -2, rather than -5/3 (Li and Yamazaki, 2001).

3 Research Methods

In this chapter we describe the research methods used in order to measure, analyze, simulate and eventually produce the billow like folds of the Lisan Formation. Three different methods of research are used in order to examine the relation between the folded sediments of the Lisan and the shear instability mechanism that occurs by regional earthquakes. We begin the research with a geometrical survey of the folded sediments that reveals an energy spectrum similar to Kolmogorov's power law of turbulent flow, emphasizing our basic assumption regarding a shear instability mechanism. The second method is the CFD model by a commercial software Fluent in which we investigate such mechanisms under the paleo-conditions (viscosity and density) of the region. The third method is a laboratory experiment; two layers of Dead-Sea mud, stratified in a tilted water tank induced by gravity.

3.1 Spectral Analysis

In this section we present a geometrical survey of the folded Lisan laminas, followed by series of spectral analyses. Spectral analysis is commonly used in statistical signal processing and physics. The interest in the spectral analysis as a tool stems from the ease which power law reveals certain uniform behavior characteristics that share the same fundamental dynamics. In order to produce such distribution we measure the geometrical properties of over 300 single billow-like folds along the Lisan Formation including: amplitude, wavelength and the thickness of the distorted lamina. The fold's energy spectrum relation $E \propto k$ was calculated according to chapters 2.4.1 and 2.4.2.

3.1.1 Geometric Measurements

When defining the geometric properties of curved surfaces one must consider the curvature, amplitude and length of the fold. These properties define this geometrical survey. The measurement technique is set as follows:

Photograph by scale - We photographed folds in the hinge direction using a digital camera (Cannon 350D; lens: Cannon 18-55) through a 1m x 1m aluminum frame with grid lines spaced at 10 cm (view Figure 18L). For smaller features we use a simple ruler.

Digital sample - We isolate each billow by marking the most contrasted lamina (by graphic software Adobe Photoshop cs2). Each marked lamina represents a single fold sampled (via Datathief software) and cataloged as a fold-sample.

Measurements - We measure the wavelength and the amplitude of each fold-sample. The amplitude of the fold-samples was measured from the base of the lamina to the most upper part of the curved wave structure. The wavelength was measured from one point on the lamina to another point on the lamina, which includes the fold-sample wave and on the same height as the first point (view Figure 18R).

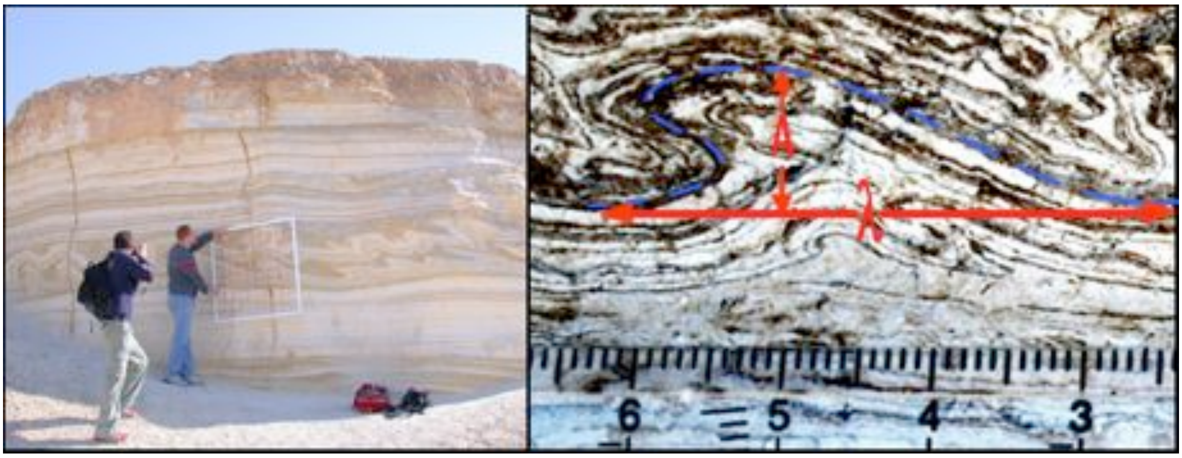

Figure 18 Measurement technique. The photographing of large scale folds by the use of a 1m x 1m aluminum grid, with resolution of 10cm. Peratzim creek (left). Amplitude and wavelength of a single fold-sample marked by dashed blue line. Wavelength is marked by red arrow. Notice the small-scale features; ruler at the bottom graduated in millimeters. Photographed near Masada (right).

3.1.2 Geometrical Analysis

Based on our fold-bank, which includes a large diversity of deformation, we search for a common relation between the different fold features. We examine these fold-samples as still images of a consistent viscous flow, just as one takes a photograph of smoke coming out of a cigarette. The square amplitude of deformation represents energy of the folded structures, and wave-number k is 1/L, where L is the measured wavelength of the fold-sample. The energy spectrum of single-wave folds from both locations (Masada and Peratzim creek) is presented in Figure 19. Each point represents a measurement of single fold-sample, amplitude and wavelength. Analysis shows staggering total mean power law fit of -1.89 with R^2 of 0.98.

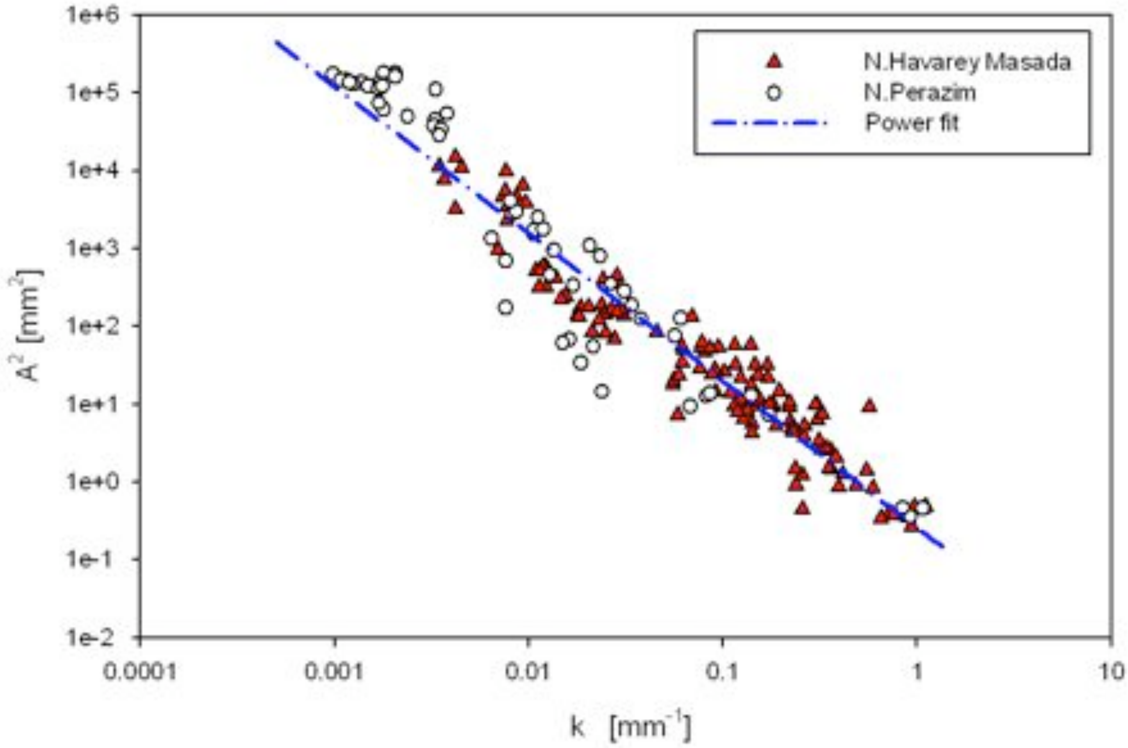

Figure 19 Energy spectrum of 300 single folds from N.Havarey Masada (red triangle) and Peratzim creek (circle). Each point in the graph represents one fold-sample. Mean power law fit represented by the dashed blue line, $y(k)=0.26k^{-1.89}$, $R^2=0.98$.

3.1.3 Analysis of fold-packets

The Lisan Formation folds are a case of multilayer folding, as deformation occurs along several sediment layers; lamina-packet. The deformed structures are usually composed of a few to several tens of laminas, folded together to the shape of waves or billows. As the beds fold under the impact of shear forces, they rotate in response to the density gradient created by the natural sedimentation*; the light top layers undergo more displacement then the lower ones. Due to this process the amplitude and the wavelength of the deformed laminas decrease according to the radius of the fold's curvature. It means that laminas at the bottom of the lamina-packet exhibit less shear and therefore tends to develop smaller wavelength and amplitudes then laminas at the top of the same packet. This does not concern the fractal behavior discussed in chapter 1.5.4. We suggest that if the folding paused at the same non-linear stage of flow, different laminas of the same folded-packet should correlate to the same power law.

* The process of sedimentation and density gradient is detailed in chapter 4.2.2

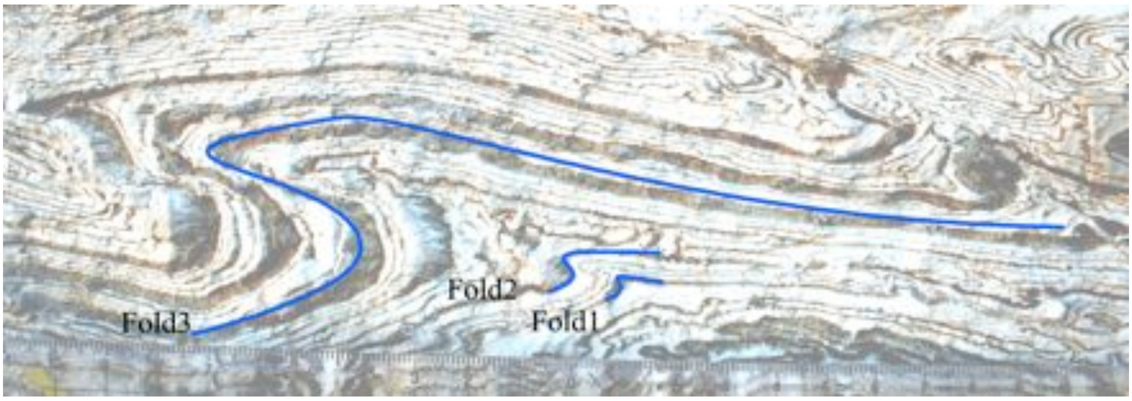

Figure 20 Fold-packet. Three different folded laminas marked correspond to three different measurements. The mean power law calculated for the fold-packet above composed by 7 single folded laminas:

$y(k)=0.08k^{-1.91}$, $R^2=0.99$.

3.1.3.1 Results

Power law fit for 23 different fold-packets is presented in Figure 20. In each folded-packet we measure between: 3 to 14 single folded laminas with overall 125 single folded laminas. We examine the spectral dispersion of each individual fold-packet by Amplitude Square to wave-number ratio as described in the previous chapter. Using the measured folded laminas we calculate power law fit for each of the fold-packets along with R^2, the correlation coefficient (Appendix 4).

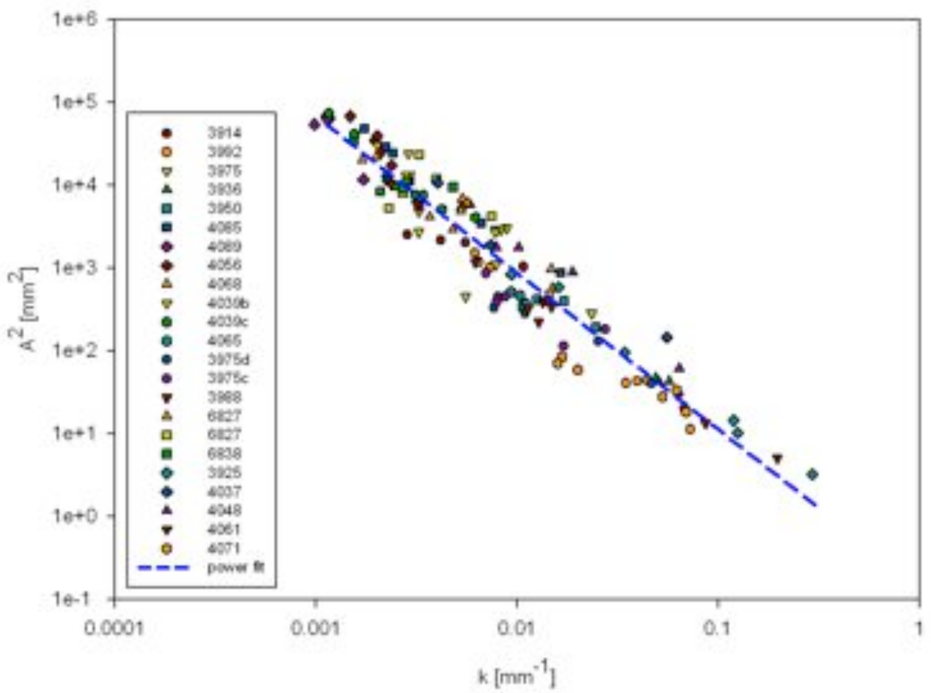

Figure 21 Spectral distribution of fold-packets Lisan Formation. Different color and symbol, presented in legend according to the caption number, mark each fold packet. Mean power fit is presented in dashed blue line, $y(k)=0.144k^{-1.89}$, $R^2=0.98$.

3.1.3.2 Statistics

The calculated power fit of the fold-packets varies from -0.4 to -3.25. We want to examine the degree of compatibility of the power fits to the Kolmogorov's power law of -5/3 based on the R^2 value. We used factor $\Delta k = \boldsymbol{PF}_i + 5/3$, which presents the differential delta from the Kolmogorov power law. Figure 22 shows that most of the power fits are about -1.667±0.5 and carry high values of R^2 (0.8 to 1). Therefore, we can suggest that the natural process of folding tends to produce folded packets compatible with the Kolmogorov power law.

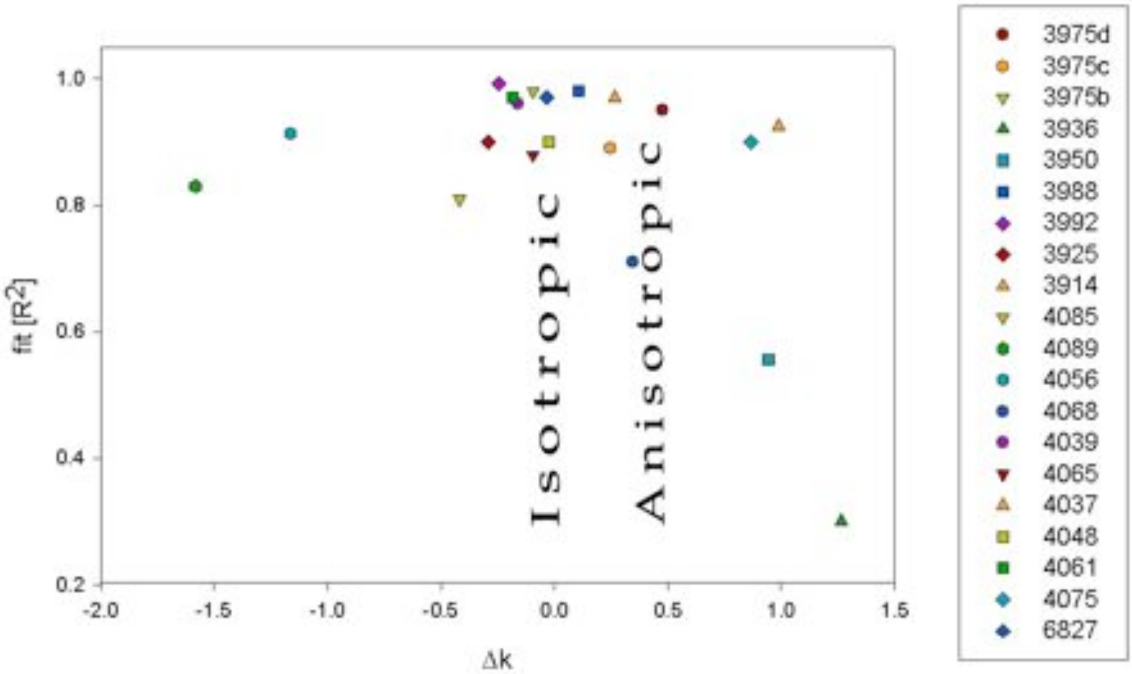

Figure 22 The compatibility of calculated power fits with the -5/3, Kolmogorov's power law. The graph shows that as the deviation (x axis) reduces, the fit (R^2, y axis) grows. Fold-packet numbers presented in the legend and corresponds to sings and colors on graph.

3.1.4 Results of spectral analysis

The energy spectrum of the Lisan folds shows consistency in respect to a uniform power fit. Calculated power law according to the analyzis method: $y(k)=0.26k^{-1.89}$, $R^2=0.98$.

The relatively high R^2 values show good compatibility ratio to the power fittings. Statistical distribution shows that fold-packets tend to deform according to a natural power law coefficient in the order of -5/3. In other words, most folding occurs between the Kolmogorov inertial-range of isotropic turbulence to the -2 power law of anisotropic turbulent flow measured by Li and Yamazaki (2001). All the above indicates that the Lisan deformed under process which led to anisotropic turbulent structures.

3.1.5 Wavelength to lamina thickness

We measure the Lisan's deformation wavelength-to-layer-thickness ratio in Masada. No clear fit was discernible.

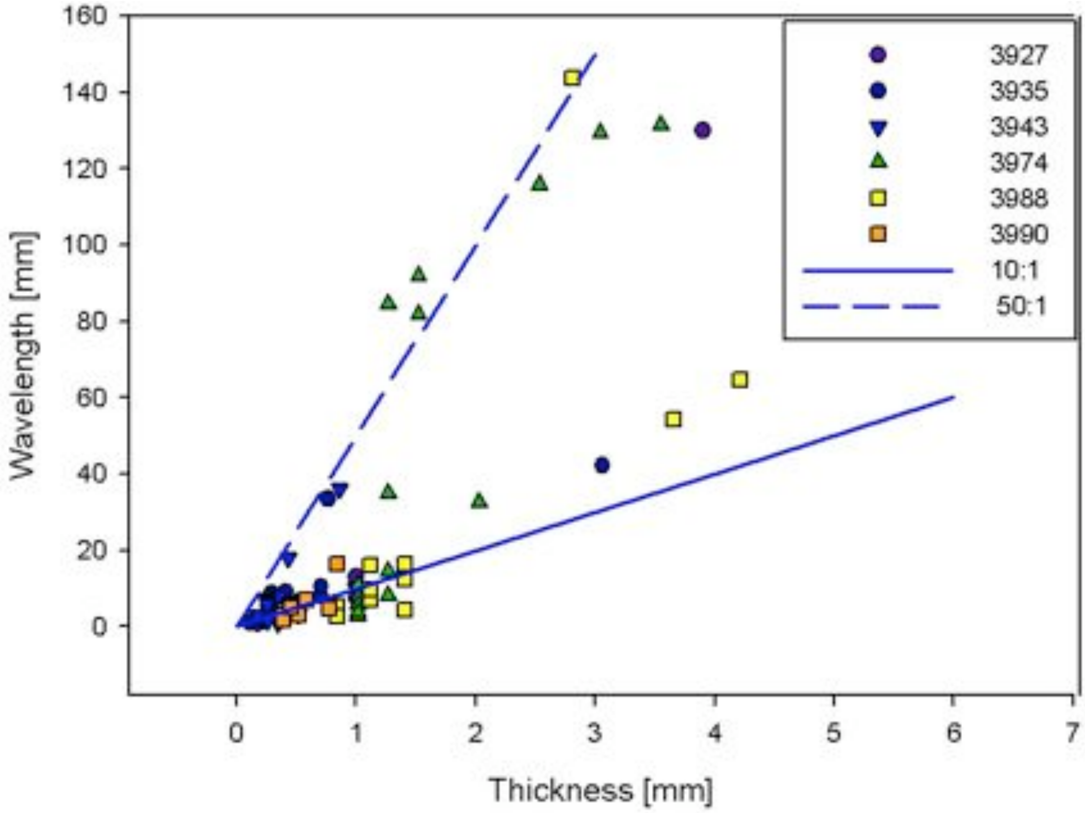

Figure 23 Wavelength to layer thickness of billow like folds, Masada.

3.2 CFD Simulation

In the previous chapter we came to an understanding that allows us to refer to the geometrical structures of the Lisan Formation as a non-linear stage of an outcome to a turbulent flow. Therefore we create a model based on these understandings.

Here we shall restrict our attention to a study of the Kelvin-Helmholtz modes, as we consider the influence of the shear instability in some detail. The methods of numerical models are well suited for these kinds of non-linear studies, and known as computational fluid dynamics (CFD) simulation. Thanks to present-day powerful computers, we are able to describe, quantify and investigate the evolution of such flows with sufficient resolution.

In this chapter we demonstrate the feasibility of such structures by a model of sheared flow mechanism of the Kelvin-Helmholtz instability type. We perform a series of 2-D numerical simulations using the commercial software Fluent (by ANSYS, version 6.2) that exhibit the physical properties of the bottom Lake Lisan during earthquake.

3.2.1 About Fluent

Fluent is a CFD commercial software; it solves the Navier-Stokes equations numerically, where supposed proper boundary conditions and mesh set up are provided by the user. The software can produce animations of flow when the flow is unsteady and displays the fields of the velocity, pressure, densities and more. We use the Gambit software for meshing and Fluent for modeling. Fluent allows to describe the mesh boundary conditions as a predefined type with the physical properties such as pressure, velocity flow or wall chosen and parameterized. It is also possible to insert a time-dependent density or velocity fields along the boundaries by user defined function (UDF).

3.2.2 Physical Parameters

Proper definition of parameters (viscosity and density) of fluids is an essential and critical factor in every CFD model. It dramatically affects the solution due to the non-linear pendency of the Navier-Stokes equations with these factors.

In this section we examine the physical properties of the system's substance that is eventually inserted into the CFD model. We perform measurements of the density and viscosity of the Lisan prehistoric sediments, unconsolidated mud stratified at the bottom of the Lake Lisan, and evaluate the sedimentary vertical density and viscosity profiles along the bottom of the lake.

3.2.2.1 Determination of the material parameters

Presice viscosity value of the Lisan mud is impossible to obtain. The present Lisan Formation is almost fully dehydrated to a state of solid marl. In addition, the chemical properties of the Lisan Formation were comprehensively studied while the parameter of viscosity and the rheological behavior still not satisfy. Therefore in order to obtain the viscosity parameter of the Lisan's wet sediments we need to find other measurable material with similar material composition, density and viscosity.

The Dead Sea, the product of the dehydration of the Lake Lisan, has been filling with sediments. The sediments deposited in the post-Lisan Holocene water body comprise the Ze’elim Formation (Stein, 2001). The Ze'elim Formation is exposed along the periphery of the Dead Sea and consists of alternating aragonite and detritus laminae (about 1-2 mm thick) (Stein, 2001). The uppermost part of the formation contains two layers that were identified as ‘seismites’, which were disturbed by the 1837 and 1927 earthquakes (Ken-Tor et al., 2001). Therefore in order to perform a direct viscosity measurement we chose the Ze’elim Formation as a suitable candidate.

We took two kinds of mud samples from the shallow area "Mineral Beach", located at the southwest region of the Dead Sea, comprising the Ze'elim Formation. The samples were collected with a respect to their depth below the lake’s floor (ULF). S1 cropped directly out of the lake’s floor, about 30 to 40 cm ULF. S2 collected about 10 cm ULF.

3.2.2.2 Viscosity measurements and readings

We measure the viscosity using Newtonian analog viscometer, model: VT-04F manufactured by GOTECH; test range of 100~4000 dPas (Figure 24). This is a rotational viscometer (Searle principle) for mobile use and laboratory operation. Its dynamic drive system enables rotation tests that allow direct reading of viscosity in dPa's or mPa's. The devise measures the resistance of fluid to the rotation of disk, inserted horizontally into the medium.

The measurements were conducted on sample S2. Sample S1 consists of much higher viscous sediments that could not be measured by this equipment.

The readings of sample S2 show unstable, but high viscosity values, as the measured viscosity was between 0.3 and 3 Pas. The first reading was ~3 Pas, and after a few seconds the reading began to drop and stabilize at ~0.3 Pas. For comparison, viscosity of pure water at a temperature of 30^{O} c is $\sim 8x10^{-4}$ Pas. We suggest that this occurs due to the liquefaction of the boundary layer between the disk and the substance, thereby reducing the viscosity to lower levels.

Figure 24 Viscosity measurements by viscometer. The jar is filled with Ze'elim formation's mud from "Mineral Beach", Dead Sea. A rotor is inserted into the sample, rotating at 62.5 rpm. Measured viscosity ~0.3 - 3 Pas.

3.2.2.3 Density measurement

Based on the resemblance of the Ze'elim Formation to the Lisan Formation, we perform a set of density measurements for sediment samples S1 and S2. Overall, instrumental measurements show a slight increase of the density profile with depth. The density profile starts with values of ~1.59 gr/cm^3 (S2), reaching maximum values of ~1.77 gr/cm^3 (S1). Therefore, two layers were taken into account for modeling purposes:

Layer	*Viscosity Pas*	*Density kg/m3*
Upper S2	0.3	1600
Bottom S1	3	1750

Table 1 Density and viscosity values taken for modeling, based on instrumental measurements of mud samples S1 and S2.

3.2.3 Building up the model

We consider the flow of two fluids in two horizontal parallel infinite streams that carry different densities and in different velocity fields. The two layers are defined as incompressible and immiscible fluids. The two phases that define the two layers were determined by the parameters described in Table 1. Each layer was patched to a different zone on the mesh (Figure 25), the light above the heavy one. Boundary conditions (velocities and pressure) set with a respect to the ground acceleration induced by the regional earthquake. Static pressure is calculated by the height of water column above the lake floor defining the hydrostatic pressure. For perturbation we use a user-defined function (UDF) of a small-scale sequence of sinusoidal oscillation at the interface between the layers.

3.2.3.1 Mesh

Mesh was built via Gambit software. The mesh defines the model environment numerically. It sets the model resolution, defines the type of the boundary (wall, vent, pressure inlet, velocity inlet etc.), and characterizes the region types (solid or liquid). In this model we consider three cases of two-dimensional rectangles: 2 meters length and 4, 20 and 100 cm height. Nodes were set as described in Table 2.

Height [cm]	*nodes x*	*nodes y*
4	400	40
20	400	60
100	400	100

Table 2 Dimensions and mesh node distributions for the three models.

The system of coordinates so oriented that its x-axis aligns with the mean flow and its y-axis defines the height perpendicularly to the lake's floor. Three cases of mesh represent three different thicknesses of layers.

3.2.3.2 Model type

We choose a *Volume of Fluid* (VOF) model for the study of our two-phase problem. The VOF model is an unsteady (time-dependent) surface-tracking technique applied to a fixed *Eulerian*[4] mesh. It is designed to describe two or more immiscible fluids when the position of the interface between the fluids is of interest. Applications of the VOF model include stratified flows, free-surface flows, filling, sloshing, the motion of large bubbles in a liquid and more. Therefore, VOF seems to be the best model for our study. The physical restrictions of the VOF model are described in Appendix C.

[4] A mathematical viewpoint, expresses the characteristics of moving particles through a fixed frame. A "fluid particle", located in $\vec{x}$ at time t, will have velocity $\vec{u}(\vec{x},t)$ with respect to the reference frame. Other view point called *Lagrangian*, means "following the motion".

3.2.3.3 Operating Conditions and Phases

Operating conditions were set according to the physical parameters of the problem. Gravity set to -9.81 m/s^2 in respect to axis y, and operating pressure set to 600,000 Pa, corresponding the hydrostatic pressure under 50 m of the lake's water column (Bartov et al., 2002). We set the primary phase to be the lighter layer, and the secondary phase to be the heavier layer, as recommended in the Fluent help manual.

3.2.3.4 Boundary Conditions

We consider a rectangle ABCD (Figure 25).

The edge types were set as follows:

- Edge AB set as *Symmetry*.
- Edge CD set as *wall*.
- Edge AD set as *Velocity inlet*.
- Edge BC set as *Pressure outlet*.

Boundary conditions were set (in Fluent) as follows:

- ***Wall***: set to the default options in the Fluent wall's boundary conditions, with a *'no slip condition'*[5]. This type of boundary is trivial to these kinds of problems and does not affect the interface line between the two layers as discussed in chapter 3.2.3.1. This type of boundary was chosen in order to represent the interface between the fixed deeper layers of sediments and the upper flowing sediments (fixed to 1 m/s).

Symmetry: this kind of boundary condition is used when the physical geometry of interest has mirror symmetry. They can also be used to model zero-slip walls in viscous flows, such as our case. This free boundary represents the interface between the mud and the water above. The boundary is set as default.

- ***Velocity inlet***: the velocity was set by a UDF, presented in Appendix B. We divide the velocity field into two zones in respect to the horizontal symmetry line. The velocity of the bottom layer is fixed to: $v_0 = 1\ m/s$ where the velocity of the top layer is set at the commencement of every simulation by: $v(t) = v_0 + a \cdot t\ m/s$, where g is gravity and *'a'* is a variable parameter of acceleration in the units of [g], and. In

[5] A condition used for viscous fluid at a solid boundary. The fluid will have zero velocity relative to the boundary.

order to develop a growing instability, we insert sinusoidal perturbation at boundary interfaces (described in chapter 3.2.3.6.).

- ***Pressure outlet***: we use a static value of pressure corresponding to the hydrostatic pressure under a water column of ~50 m, same as the pressure in the operating condition section: 600,000 [P].

3.2.3.5 Velocity field

The model is based on a fixed rectangular window in which the flow is moving into the mesh from the left side and exiting the mesh at the right. The growth rates of types of instabilities are mainly dependent on the intensity of the velocity shear. Furthermore, the relatively short duration of an earthquake strictly defines our model time laps. Therefore, it is in our main interest to examine the behavior of this stratified structure according to the velocity difference between the two layers.

We set the bottom layer to a fixed velocity of 1 m/s.

3.2.3.6 Sinusoidal Perturbation

We insert a sinusoidal perturbation at the interface between the two layers. This kind of external disturbance acts as a fluctuated *splitter-plate*. Splitter-plate is an experimental tool, commonly used in cases of impinging-shear-layer-instability, mixing (Mehta, 1991) and vortex-shedding studies (Nakamura, 1996).

Frequency of perturbation was set according to the most energetic frequency of an earthquake, which is about 1 Hz. Therefore, the UDF function defines the velocity inlet boundary set as a *sin* function that perturbates the contact point between the two fluids, and the velocity inlet boundary (view Figure 25). The *sin* function is time dependent oscillation $x_0 = A\sin(wt)$. Such combination of sinusoidal perturbation and the shear velocity creates a "greenhouse" for fluctuations to develop along the interface between the two fluids that corresponds to the velocity profile. The amplitude of the initial perturbation is chosen such that it should be well within the linear growth range. This is checked explicitly by calculating an apparent growth rate from the non-linear model as a function of time as suggested in similar previous research (Peltier, 1978).

The UDF function used in this research is based on the work of Laurent Nack and Ludovic Maas (2000), and is described in Appendix B.

Figure 25 Illustration of the phases and boundary conditions in CFD model. Sheared velocity inlet on edge AD (U1 and U2), along with a sinusoidal perturbation. Upper layer set to be the primary phase (the lighter layer) and the heavier layer set to be the secondary phase. Edge BC is set to pressure outlet boundary.

3.2.3.7 Initial conditions

The physical parameters of the simulations were set under the parameters suggested in Table 1. The initial conditions of the model were set as follows:

- Frequency of oscillation: f=1 Hz.
- Amplitude of oscillation: A=0.005 m.
- Time Step size: 0.01 s.
- Number of iterations: 150
- Total time of simulation: 1.5 sec

Overall we perform 12 simulations. In every simulation we increase the acceleration of the upper layer (0.1, 0.2, 0.3, 0.6 [g]) producing stronger shear at the interface between the two layers.

3.2.4 Results – CFD Model

We present now results of 12 simulations in respect to the acceleration and mesh size.

3.2.4.1 Density and velocity profiles

This section contains results of 12 simulations. Four simulations were conducted for each of the meshes, for the 4 different accelerations; compatible with the ground acceleration carried out by the earthquake's intensity. We present three main figures (Figure 26, Figure 27, Figure 28). Each figure represents a mesh case model, in which density and velocity fields are presented. The density and velocity legends are presented in each of the figures. The simulation figure represents the density and velocity fields at T=1 sec.

Complete motion clips of the simulations are available online on:

http://www.tau.ac.il/~shmulikm/Nadav_W/simulations.html

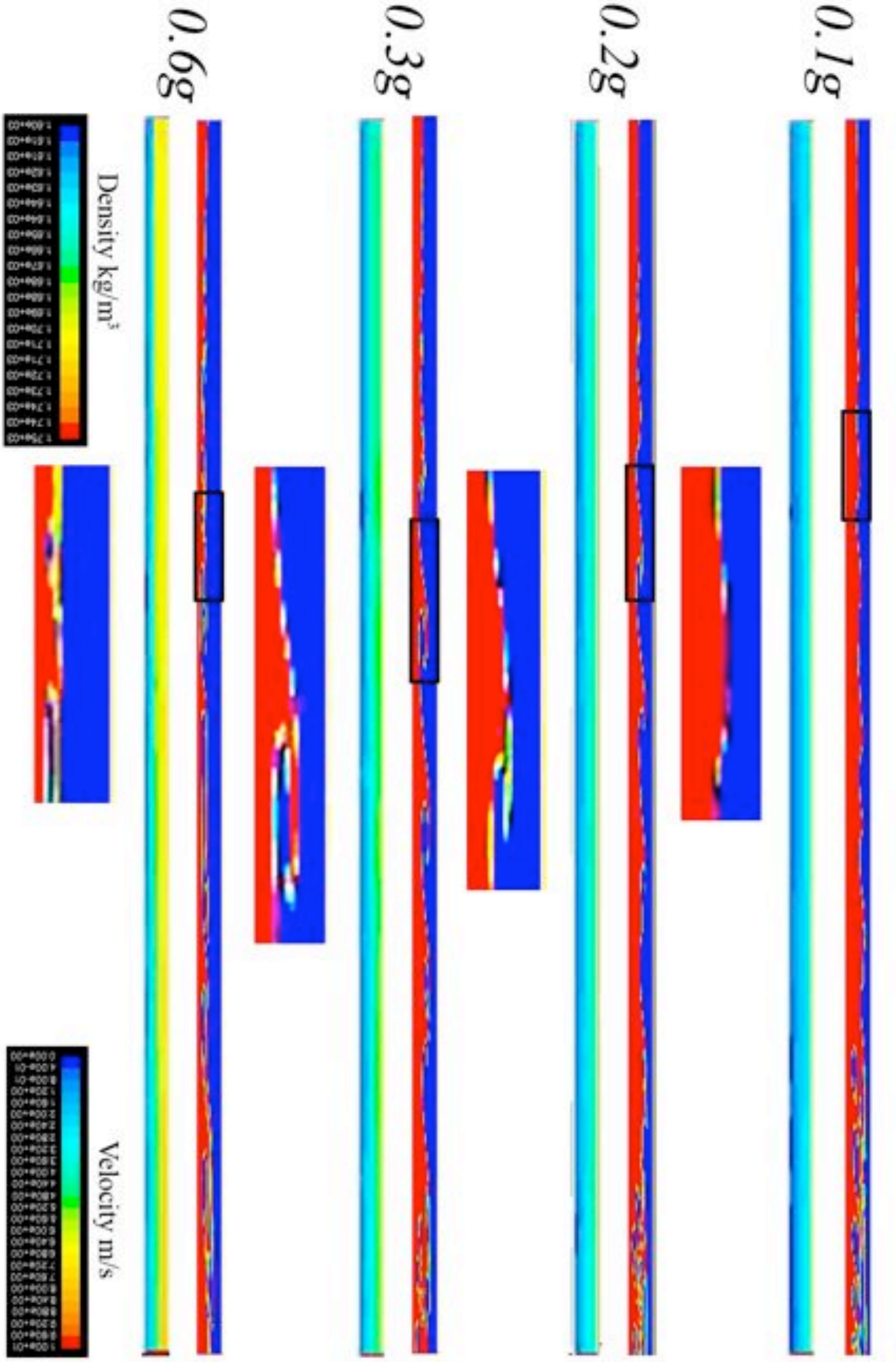

Figure 26 CFD simulations. Mesh size: 0.04 m x 2 m. Magnified rectangle section from the mesh is located at the bottom of each simulation.

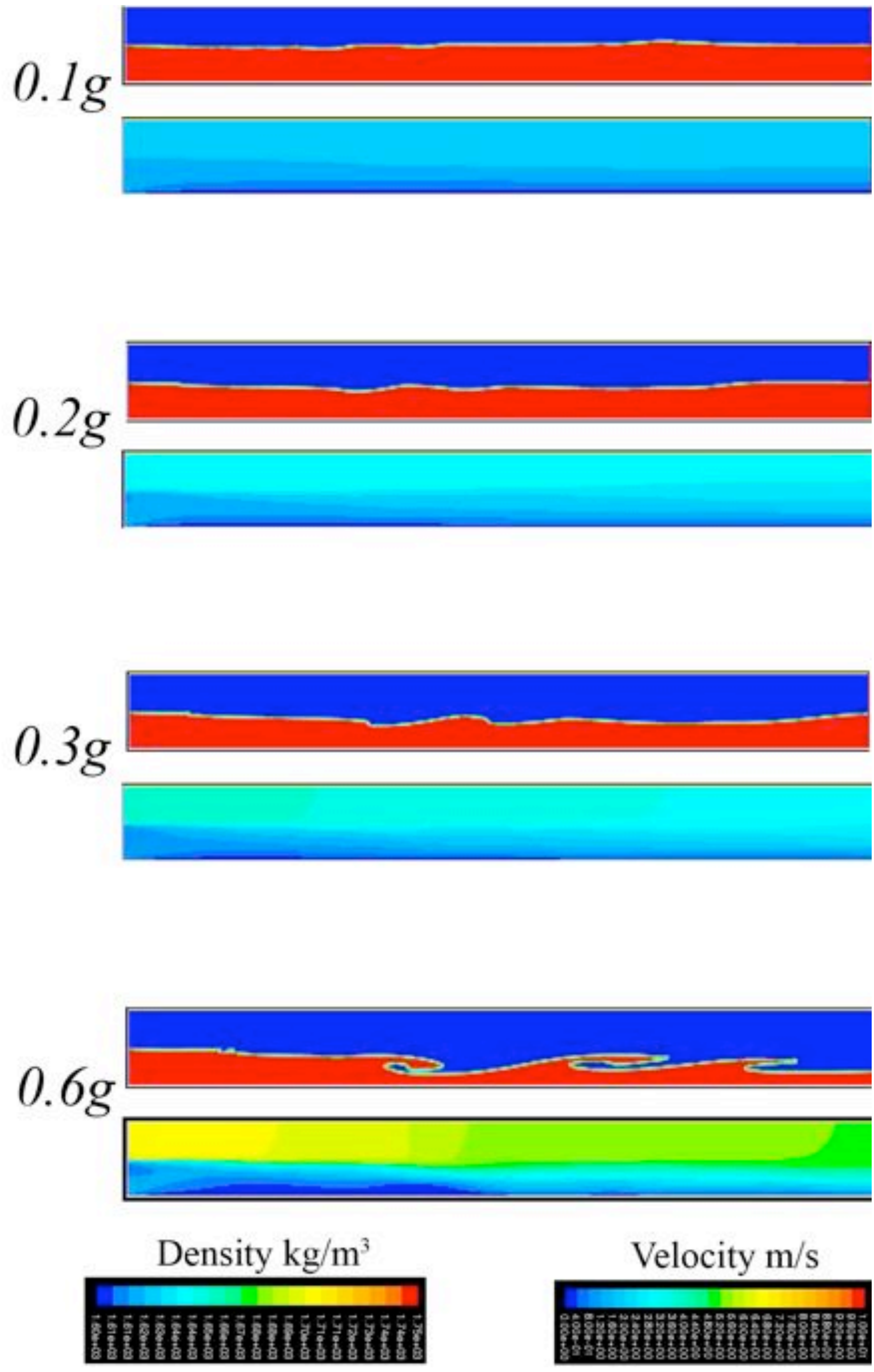

Figure 27 CFD simulations. Mesh size: 0.2 m x 2 m

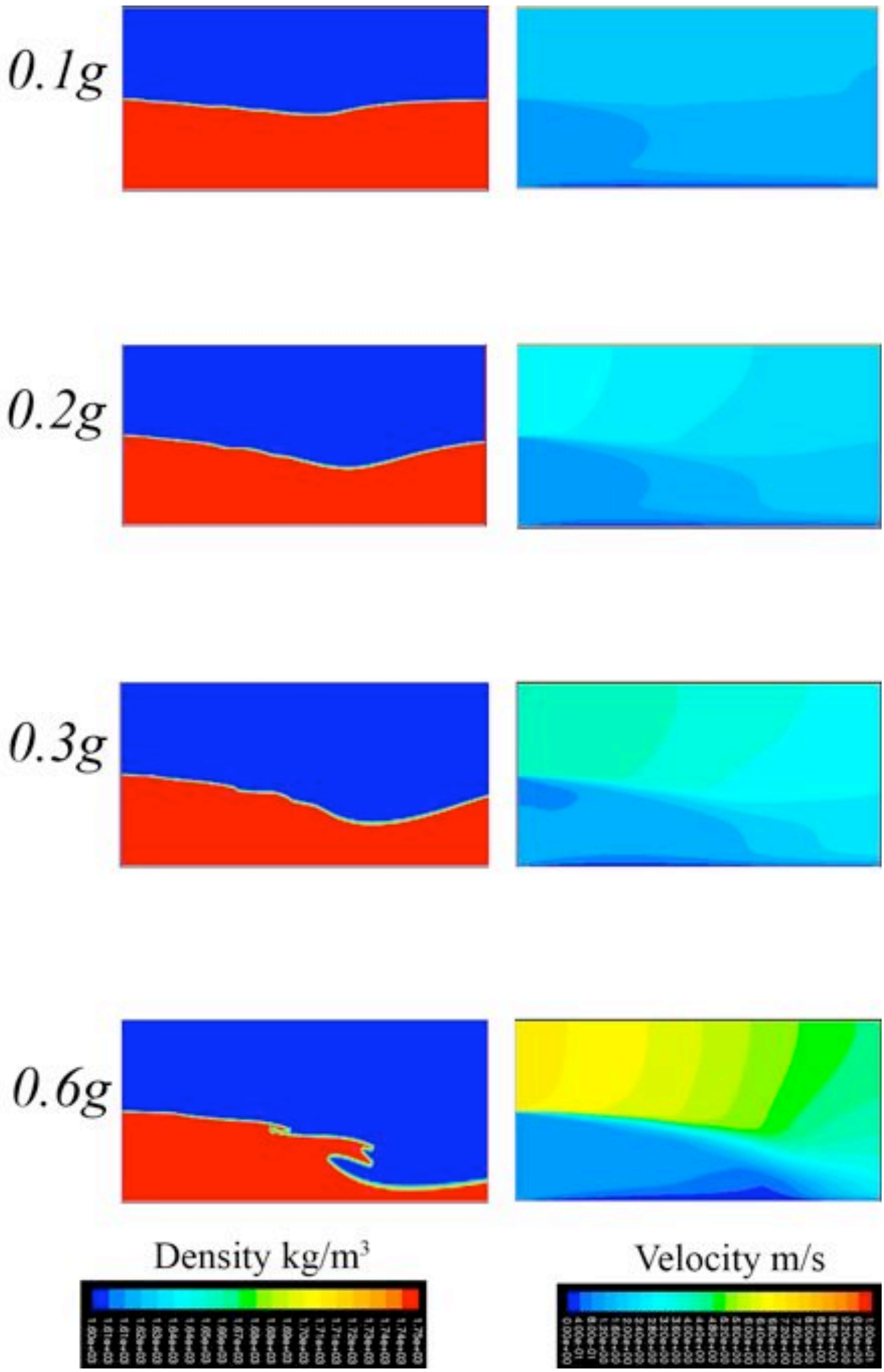

Figure 28 CFD simulations. Mesh size: 1 m x 2 m.

3.3 Laboratory Experiment

The main aim of the experiment is to produce KHI billow patterns in a laboratory setting using a substance that matches the Lisan wet sediments. The experiment is designed to resemble the CFD model configuration and is based on the shear mechanism induced by gravity. We used the same Dead Sea sediment described in former chapters as samples S1 and S2, which correspond to the two-layer-model.

By producing billow patterns similar to the ones in the Lisan Formation we achieve a better understanding of this complex natural configuration. The establishment of similar fold patterns in this laboratory experiment suggests that the Kelvin Helmholtz instability could have been the mechanism that created billow like folds of the Lisan Formation during the Late Quaternary.

3.3.1 Introduction

Laboratory studies of instabilities and turbulent mixing in stratified shear flow are highly significant because the matching of computer-generated model to Nature is limited. Therefore most of our knowledge and understanding of the nature of turbulence comes from field observations.

Former experiments (Owen, 1996) have demonstrated the style of deformation resulting from the liquefaction of sand, mostly cross-bedded, under different driving forces. He conducted several experiments using shaking table motion of 5-10 s duration with maximum accelerations from 0.29g to 1.15g. Although the experiment simulates the deformation of sediments triggered by earthquakes, this experiment does not include vibration. Our aim in this experiment is to investigate the setup of two layers sliding one above the other under shear flow.

One of the first who investigated shear flow by experimental design was Thorpe (1968). In his research he demonstrates this using a long horizontal tube containing two liquids with two different densities, horizontally stratified, light above the heavy. The tube is tilted by a small angle so the lighter layer will flow above the heavy inducing a velocity shear across the fluid layers. Thorpe observed the onset of the instability as the interface deformed and rolled up into a string of billows with a certain wavelength. This experiment was very successful and was followed by a number of studies. Experiments on interfacial stability structure have revealed that the evolution (birth, growth, breakdown and collapse) are dependent on the characteristics of the initial flow, stratification and viscosity(DeSilva et al., 1996; Rotter et al., 2007; Thorpe, 1973).

Hitherto most of the laboratory experiments of KHI billow generation-involved materials containing low viscosity values (gas, water, oil) such as sheared ocean and atmospheric flows. In the Lisan Formation the substance stratified with high viscosity values, which may carry a complex form of a two-phase-flow. Therefore, converting our 2D CFD model into a laboratory experiment is not a trivial problem.

3.3.2 Experimental setup

Laboratory investigations have many limitations because:

1. The mud that we brought from the Dead Sea seems to have high cohesion and viscosity values, making a shear flow configuration a difficult task.
2. The delicate process of sedimentation builds a natural density gradient over many years, which could not be imitated within laboratory conditions.
3. The high cohesic relations between the partials and the sediment beds make the process of manual layering difficult.

One of the major difficulties was to establish shear between the two layers. Former laboratory experiments describe sophisticated laboratory equipments such as pumps (Strang and Fernando, 2001), or dynamic flow-management (Mastrano and Melatos, 2005) which were followed and documented by laser or X-rays. We decided to simplify our experiment analogously to Thorpe's (1968). Therefore shear is achieved naturally by gravity that leads this experiment to focus essentially on the KH billow generation up to the stage of rotation.

The experiment was performed in a glass water tank, 60 cm long, 30 cm wide and 40 cm deep, initially horizontal and stably stratified with two layers of different densities (Figure 29). The density profile corresponds to the characteristics of the samples S1 and S2 and is stratified lighter above heavy.

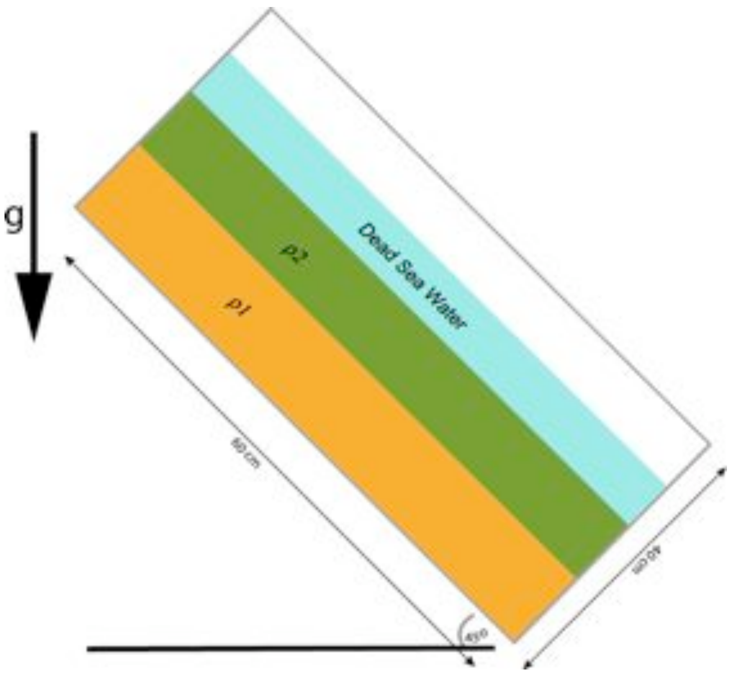

Figure 29 Illustration of the experiment set-up. Tilted water tank (45^{O}) contains two layers of the Dead Sea mud, stratified with density gradient ($\rho_1 > \rho_2$); on top of the layers Dead Sea water.

In order to distinguish the density profile, each layer was dyed a different color with gouasch pigments. The bottom layer was cropped from the Dead Sea shallow water bottom of 'Mineral beach' by sticking the water tank directly into ground. The stratification of the top layer was obtained by pouring the mud carefully into the water tank. The layer was carefully smoothed and balanced horizontally.

The motion was initiated by tilting the water tank to an angle of $\sim 45^{O}$ that provided effective gravitational acceleration of: $a = g\sin(45) \approx 0.7g$ parallel to the layers, where g is the gravitational acceleration. The light layer on top and the heavy layer on the bottom generate a velocity shear in response to the gravity. Despite the fact that in our CFD model we used sinusoidal perturbation to trigger the billows, in the laboratory experiment we did not include any initial perturbation.

The experiment was recorded by a 3CCD digital camera (Sony DCR-TRV900E) at 25 frames per second. The resolution of the camera was 512 x 720 pixels x 32-bit. The measurements of the deformations performed according to the dimensions of the water tank.

3.3.3 Results - Experiment

As we tilted the water tank, lighter sediments (S2) began to smoothly slide past the bottom layer S1, which remained still. This created a velocity shear between the two mud layers. A few seconds after we tilted the water tank we saw that on the left side of the water tank a small elevation was formed at the interface between the layers. After a few more seconds the elevation began to take the shape of an asymmetrical billow. Then, the top of the billow began to stretch in the direction of the flow. No roll-ups were formed, probably due to insufficient velocity shear. The total time of the experiment was ~100 sec. The billow amplitude was 6.2 mm. The measured velocity of the upper layer was about 1mm/s.

Figure 30 shows a series of video frames of the interface at different time and stages of evolution and the measured amplitude of the billow-like deformation that formed at the interface between layer 1 and 2.

Capture	*Time [sec]*	*Amplitude [mm]*
a	0	1.9
b	12	3.5
c	21	3.9
d	35	4.1
e	59	4.9
f	81	6.2
g	107	6.2

Table 3 Description of time and amplitude measured for the frame displayed in Figure 30.

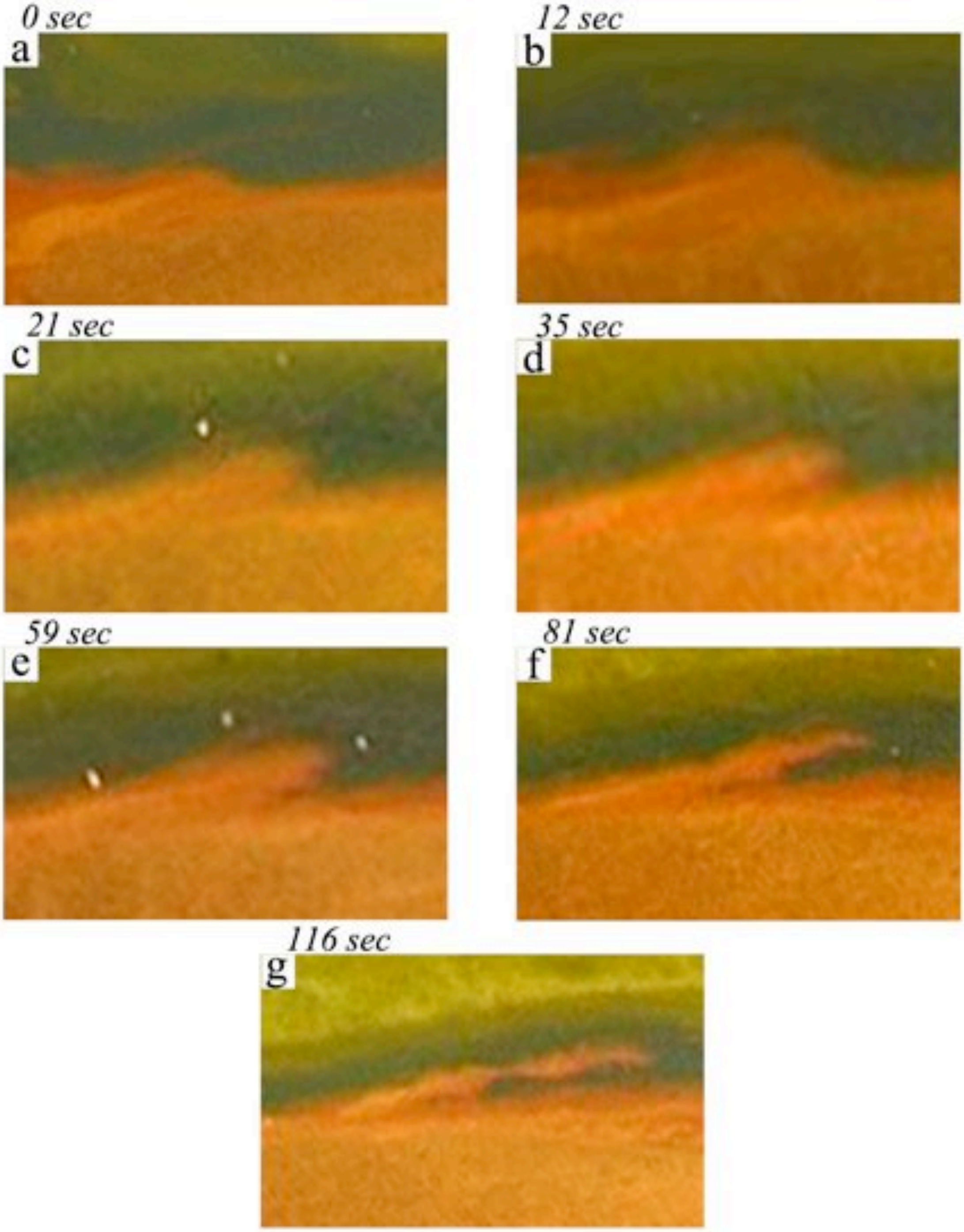

Figure 30 Video frames of billow evolution from a stratified Dead Sea mud experiment. We performed the classic KHI experiment with the Dead Sea floor substance. Two layers of horizontally stratified sediments in a tilted water tank (~45^{O}).

3.3.4 Analysis

The miniDV tape was sampled to PC for editing purposes. We captured still images of the evolving deformation in order to inspect the growth rate of the billow's amplitude. Each image was inspected and the amplitude and wavelength of deformation were measured. The growth rate of amplitude is presented in Figure 31 with linear fit.

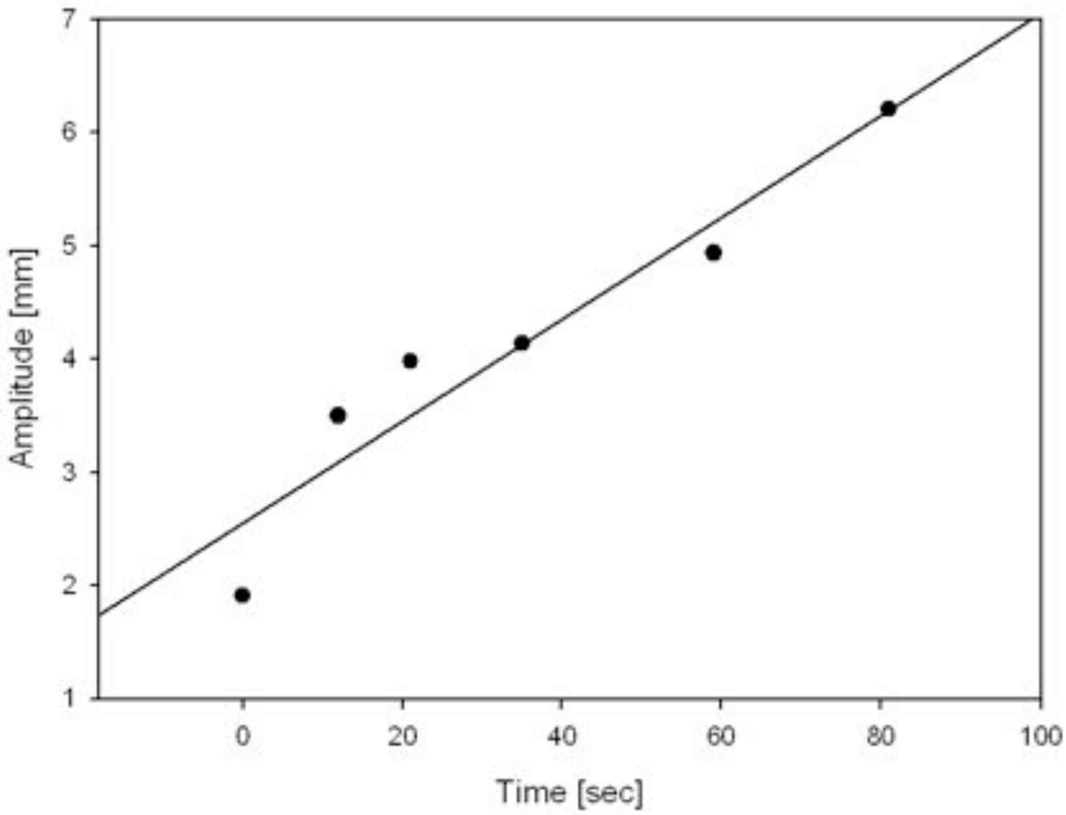

Figure 31 Amplitude in mm (A) as a function of time of a single billow evolution from the laboratory experiment of the Kelvin Helmholtz instability. Linear fit: A(t)=0.045t+2.5, R^2=0.914.

The experiment shows that deformed billows could be established even by a minimal shear of 1mm/sec. In cases where shear instability is involves, the external perturbation obtains exponential growth rate (Shearer and Fruh, 1999). The linear growth rate shown in Figure 31 may point deference between the experiment and the KHI model, or a lack of shear.

4 DISCUSSION

In this chapter we discuss the results of our three-method investigation: geometrical analysis of field observations, numerical simulations and experiments. We examine each of the physical parameters that were utilised in this research and discuss the characteristics and their roles in the KHI process. We also examine the feasibility of several other mechanisms that may also lead to such deformations.

4.1 Why KHI?

Folding to billow-like structures is not uniquely reserved to KHI. There are several other natural mechanisms that may also trigger similar structures of billow-like folds of the Lisan Formation. Theses mechanisms include: gravitational instabilities triggered by tectonic activity, stress/strain conditions leading to deformed beds and others which relate to the topographic configuration of the basin; all of these can be related to the Lisan region. Therefore, before we proceed to discuss the results, we first inspect the feasibility of other types of fold-producing mechanisms.

4.1.1 Rayleigh Taylor instability

The Rayleigh–Taylor Instability (RTI), (after Lord Rayleigh 1883 and G. I. Taylor 1950), occurs when a dense, heavy fluid is being accelerated into a light fluid in a gravitational field (Ramaprabhu and Andrews, 2004). The initial configuration of RTI refers to two plane-parallel layers of immiscible fluids characterized by different densities, stratified with the heavy one above the light one, in metastable equilibrium. The slightest perturbation leads to the release of potential energy. Due to gravity the heavier material moves down as the lighter material is displaced upwards. As the instability develops, downward-moving irregularities are quickly magnified into sets of inter-penetrating "mushroom cups" (Figure 32).

There are few resemblances between a Rayleigh-Taylor instability and the billow-like folds in the Lisan. Sediments may have been folded to a bell-like shape under the mechanism of RTI, and look similar to the exposed folds in the Lisan (Brodsky et al., 2009).

However, the situation of a heavy layer above a lighter layer is unlikely in the Lisan. Particles sink and press the top of the sediments on the lake's floor. In this process a denser layer is formed beneath the lighter ones. Therefore the condition of inversed density gradient, the crucial requirement for instability, is unfeasible under the circumstances of our case study and rules out the possibility of the Rayligh-Taylor instability.

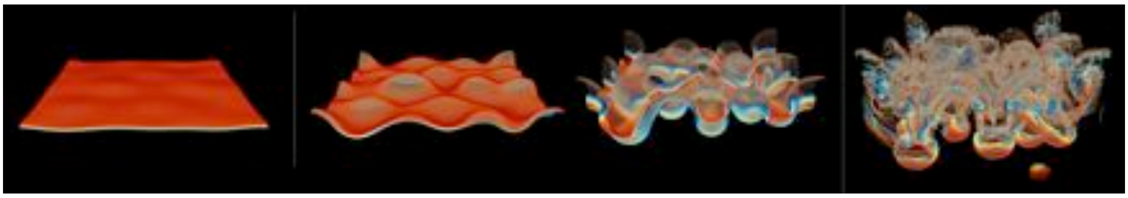

Figure 32 Numerical simulation of Rayleigh-Taylor instability. This sequence shows four time intervals from an XT3 simulation (on a 768^2 x 1536 grid), with regions of predominantly heavier fluid (red), lighter fluid (blue). By the time of the fourth image the mixing shows descending “mushroom caps” that produce fine-scale mixing. Note the visual likeness of the mushroom-cups to the folded sediments of the Lisan Formation. By a vertical incision the density interface may look similar to the exposed billow-like folds of the Lisan Formation.

4.1.2 Buckling

Buckling is responsible for the formation of many natural fold structures. The fact that most folds exist in rock volumes that have undergone shortening roughly parallel to the layers that are folded (Suppe, 1985) gives rise to the possibility that buckling may be responsible as the mechanism causing the Lisan's folds.

The mechanism of buckling can produce folds in reasonably regular patterns, for which a wavelength and amplitude may be defined due to bending, transverse deflection in response to a transverse applied forces couple (Suppe, 1985). In other words horizontal shortening which leads folding. Some of the wave patterns are not characterized by uniform wavelengths (such is the case of the folds of the Lisan Formation); instead, several wavelengths are superposed, reflecting the control of the layer thickness over the fold wavelength. Usually the fold’s size corresponds to the layer thickness; microscopic layers display microscopic wavelengths and so on. The ratio of the wavelength to layer thickness in multilayer configuration is ~27 (J. B. Currie, 1962). In chapter 3.1.5 we show that there is no clear linear fit for the wavelength to layer thickness relation in the cases of the Masada folds (Figure 23).

In the cases of multilayer folds created by buckling there is no indication in the literature regarding the consistency in the folds orientation, or distinguished preferred asymmetric folding. This is in contrast to the clear preserved orientation of the folding that is commonly observed in the case of the Lisan Formation's folds. Furthermore, the process of buckling usually involves a shortening of the deformed rock. If a buckling mechanism would have taken place along the sediments of the Lisan Formation, one could expect the full packet of sediments, from bottom to top of the lake's floor, to deform. In the case of the Lisan's billow-like folds it is clear that only some of the layers have deformed while the sediments at the bottom remain intact. Therefore, it is unlikely that the buckling mechanism is responsible for the billow-like folds of the Lisan Formation

4.1.3 Floods

In dry climate regions rainfall is highly variable and can be of high intensity. An 1800 year record of paleofloods from Nahal Zin in the Negev Desert includes 28 large floods ranging from 200 to 1500 m^3s^{-1} (Greenbaum et al., 2000). A recent study (Greenbaum et al., 2006) reported evidence of increased flood magnitude and frequency in the southern Negev during Marine Oxygen Isotope Stage[6] MIS3 transition into MIS 2. This report is compatible with the largest documented level rise of Lake Lisan between 30 and 27 ka. Therefore, it is clear that Lake Lisan was affected by frequent flood events. The fact that floods are a powerful energy source raises the possibility that they may induce the formation of the billow-like folds.

Water floods, which are Newtonian fluids, have very little shear strength (depending on the amount of sediments loads) (Baker et al., 1988), therefore it is not likely for such liquid to produce a shear force which would overcome the high porosity and viscous forces within bottom-lake-sediment.

More significantly, there was no evidence for turbidity currents or any other lateral flow within the disturbed units (Ken-Tor et al., 2001).

4.1.4 Seiche

Paleoseismic studies along the Lisan Formation (Agnon et al., 2006; Marco and Agnon, 1995; Marco and Agnon, 2005; Marco et al., 1996) indicate at least 30 M>5.5 seismic

[6] Marine isotopic stages (MIS) are alternating warm and cool periods in the Earth's paleoclimate, deduced from oxygen isotope data reflecting temperature curves derived from data from deep sea core samples.

events extended from 70-14 ka in the form of breccias. Some of the breccias were found with gypsum ($CaSO_42H_2o$) beds on top. The Paleolake Lisan structure divided into sulfate-rich upper water layer and calcium-rich lower water layer reservoirs (Stein et al., 1997) which led to under-saturation of gypsum (Torfstein et al., 2008). The gypsum beds led Begin et al. (2005b) to suggest earthquake-induced high waves (seiche) as a water column mixing mechanism, which resulted in the gypsum saturation. Under these circumstances 11 layers of gypsum beds have been formed on top of breccias; associated with M>7 earthquakes which may be responsible for seiche waves.

Tsunami may produce enough energy in order to mix the natural water column of Lake Lisan. But as discussed in former chapter, water alone is unable to overcome the internal forces within the sediments therefore unable to produce enough shear in order to create such instability.

4.1.5 Waves and Rushed waters

Surface waves occur as regularly spaced hummocks and hollows of many different scales on the air-water interface. The wind energy perturbs the equilibrium of the water-air interface and propagates waves as a result of friction and pressure forces. Sea waves are a combination of longitudinal and transverse wave motions. When waves propagate, the particle trajectories are compressed into ellipses. The radius of the circular motion decreases with depth. At depth equal to half of the wavelength (wave-base), the orbital movement decreases to less than 5% of its value on the surface. It is the greatest depth at which the surface waves can influence the bottom. For ideal progressive waves on infinitely deep water, we can describe with g (the gravitational acceleration) the wave length $\lambda = \frac{g}{2\pi}T^2$ in a relation to the time period T and in velocity $c = \left(\frac{g\lambda}{2\pi}\right)^{1/2}$.

The water column height above both of the locations, Masada and Peratzim creek, is in the order of ~100 m (Bartov et al., 2002). Therefore, in order to influence the lake's bed a wave must have a wavelength λ> 300 m with a velocity in the order of ~20 m/s. Such waves occur under severe storm conditions in the oceans and develop heights of more than 15m. Therefore it is not reasonable to propose that such waves developed at the paleolake Lisan.

4.1.6 Gravitational-slide

Gravitational-slides occur under the influence of gravity on sediment layers in a condition when horizontally stratified layers are tilted. The experiment described in chapter 3 contributes to our understanding of the kinematic properties of the Lisan substance. The experiment shows that gravitational-slide alone could not produce enough shear in order to deform the sediments up to the present state through KHI mechanism. Internal forces within the soft sediments resist the gravitational forces and slow down the dynamic processes. Furthermore, we cannot unambiguously demonstrate that the folding orientation of billow-like formations corresponds to the sediment layer strike. Therefore we cannot refute or prove that gravitational-slides took place at all or participated in the folding process.

4.2 Parameterization of the KHI model

In this chapter we inspect and discuss the physical parameters that combine the KHI model in the light of the observations geometrical analysis, and CFD results.

4.2.1 Viscosity

The effective viscosity of sediments changes when in suspension. It depends on the size and shapes of the suspended particles as well as the rheology. The highly concentrated and cohesive sediments exhibit non-Newtonian and time-dependent behavior caused by particle interactions, which complicates the prediction of the strain-stress ratio and their response to applied forces (Faers and Kneebone, 1999). All the above introduce us to a non-trivial problem when examining the viscosity using the traditional approach.

Non-Newtonian behavior under vibration

With a Newtonian fluid the applied shearing stress is directly proportional to the rate of flow or shear, the constant of proportionality, being the viscosity.

Natural saturated sediments under shear commonly exhibit non-Newtonian behavior, as the stress-strain rate curve may be either non-linear or linear. Experimental examination of saturated commercial clay powder shows that the kinematic viscosity changes and carry non-Newtonian characteristics under suspension (Lioubashevski et al., 1999). In spite of the fact that the Lisan sediments may act as a non-Newtonian fluid we had no choice but to perform viscosity measurements using a Newtonian viscometer. In this research we do not attempt to investigate the stress-strain behavior of these sediments under shear or vibration or to solve the issues and complexities of the non-linear behavior.

Without dealing with the exact rheology of the sediments, overall we suspect that these sediments were quickly liquefied, absorbing large amount of water. As a result of the liquefaction the magnitude of the viscosity is reduced to a state of linear stress-strain ratio therefore although the measurements of the viscosity were not precise, it gave us a good evaluation of the viscosity before and during the process of liquefaction.

Pore pressure

When saturated sediments are subjected to earthquake induced shaking, pore water pressure in the soil starts to progressively build up leading to the loss of soil strength. The complex process of liquefaction is presented as the liquefaction cycle and discussed in many research studies (Liyanathirana and Poulos, 2002; Snieder and van den Beukel, 2004). These research studies present the cycle of liquefaction as a self-inducing process that occurs during earthquake. The chain of events between the: deformation, pore space, pore pressure, and the elastic moduli, are linked by non-linear relations.

Our CFD model does not take these issues into consideration. The model initialize after sediments were liquefied and non-linear processes (such as the increase or decrease of the pore pressure) within sediment are not taken into account.

Viscosity gradient

The Viscosity gradient used in the CFD model is based on measurements described in chapter 3.2.2.2. As the viscometer's rotor rotates, viscosity readings drop from 3 to 0.3 Pas. This leads us to assume that the mechanism of the liquefaction reduces sediment's viscosity while the ground shakes during an earthquake.

There is another possibility that may produce this kind of viscosity gradient. Previous research (Amy et al., 2005) in vertical stratification experiments show sharp front at the sediments viscosity profile between two top layers. They conducted their experiment in a large tank (6m x 0.5m) filled with solution and studied how density and viscosity stratification influence flow behavior. The viscosity of the solution is introduced as a dimensionless viscosity ratio: $\mu^* = \dfrac{\mu_U - \mu_a}{\mu_L - \mu_a}$, where μ_L and μ_U are the viscosities of the lower and upper layers, respectively, and μ_a is the viscosity of the ambient fluid. They have measured viscosity ratio values of 0.05 to 0.4 due to the process of gravitational particle stratification. This kind of process can act as alternative mechanism and produces a pre-earthquake viscosity gradient.

4.2.2 Density

Unlike the viscosity parameter, density can be accurately measured. In the former chapter we presented measurements of two mud samples (S1 and S2) corresponding to the two stratified layers on the lake's floor.

The density gradient of about 10% that was measured pre-CFD model can be explained by two mechanisms or a combination of the two: natural sedimentation and liquefaction.

When mud floc settles, the flocs that arrive first are squeezed by the flocs that settle on top of them. Pore water is driven out of the flocs and out of the space between the flocs. This process is known as self-weight consolidation. Due to this process and as a result of a hindered-settling[7], the process of sedimentation tends to form a sharp front between layers of uniform density (Thacker and Lavelle, 1977). In this way the layers are distinguished by the mass fraction of the solid material within the sediments (Table 4).

According to Gotze et al., (2007) the density of the valley deposits is 2150 kg/m^3 and the density of the Dead Sea water is about 1250 kg/m^3. The layer's density by fraction of solid ρ_j is described as $\rho_j = \chi_j \rho_s + (1-\chi_j)\rho_w$, therefore the fraction of solid material in the sediment is:

density	ρ_j	*layer*
1.59	0.25	*up*
1.77	0.37	*down*

Table 4 Density fraction of solid material within measured samples. Lower sediments are denser and precipitate less water according to natural sedimentation.

The density measurement corresponds well to the theory of natural sedimentation. Our measurements show increased density of about 10% when the two samples are compared.

It is also possible that the liquefaction increases the fraction of water in sediment increasing the natural density gradient as water penetrates the top layers during the earthquake.

We suspect that the folding occurs at a layer of an interface between two horizontal layers that carry different densities. The typical fraction difference between two successive

[7] A term used to designate the decrease in the fall velocity of sediments in suspension resulting from an increase in sediment concentration.

sediment layers and according to our density measurements of the density gradient is in of the order 10%, which gives $\Delta\rho \sim 180$ kg/m^3.

4.2.3 Shear

Shear is a crucial factor in any turbulent flow. Numerical models show that in cases of initial density profile, in the absence of a mean shear, the buoyancy frequency slowly decreases with space and time (Galmiche and Hunt, 2002).

There has been evidence that the density gradient has a major effect on shear build-up. Damaging effects of the soil liquefaction on pile foundations and structures have been observed in past earthquakes. Tests show that the pile-soil interaction is influenced by the dynamic response of the soil, the dynamic response of the pile and the soil's density profile (Kramer et al., 2002). Experimental data analyzed by a WAVE program indicates that permanent shear strains increase as relative density decreases. Numerical simulations show that with higher soil density the pore pressure builds up slower and the shear strains are limited at a lower level. It also shows that piles embedded in soil with lower density experience more displacement that piles embedded in the soil with higher density. These simulations show that in the case of liquefiable layers the affect on the pile head deformation is stronger even when the external loads are small.

4.2.4 Peak Ground acceleration, DSB

In this research we attempt to develop a connection between our field observations to earthquake intensity. The initial conditions at the velocity inlet boundary are set according to values of peak ground acceleration (PGA). The attenuation relationship of PGA is based exclusively on the recorded seismic events. One of the most frequently used attenuation function by the Geophysical Institute of Israel (GII) for rock soil conditions was that of Boore, Joyner and Fumal (2005; 1981).

On 22 November 1995 a large earthquake was felt in south Israel and along the Gulf of Aqaba. Magnitude of M_L 6.2 (M_w=7.1) was measured, and epicenter is 80 km south to the city of Eilat. PGA of ~0.15g and peak ground velocities of ~0.085 m/s were measured near the Aqaba Hotel (Saffarini, 2000). This is the strongest earthquake recorded in the region. The seismic data show inconsistency between the PGA models and the observed values. Therefore modifications were advised to the PGA model to:

$$
\begin{aligned}
\ln(A) &= -0.055 + 0.525(Mw - 6) - 0.778\ln(r) \\
r^2 &= R^2 + 31.02
\end{aligned}
\qquad \textbf{(26)}
$$

Where A is PGA in units of g, M is moment magnitude and R is the distance in km to the fault plane. Figure 33 demonstrates Boore's attenuation equation, colored by the magnitudes compatible to the distance and PGA. The distance to the fault in our case is evaluated to be ~10 km. Therefore the correlating magnitudes to the CFD model to PGA (0.3 - 0.6 g) are 6 to 7.5. This is also compatible with the strong earthquakes evaluated by Begin et al (2005b), responsible for the BGD's and Breccias (Heifetz et al., 2005) along the Lisan Formation.

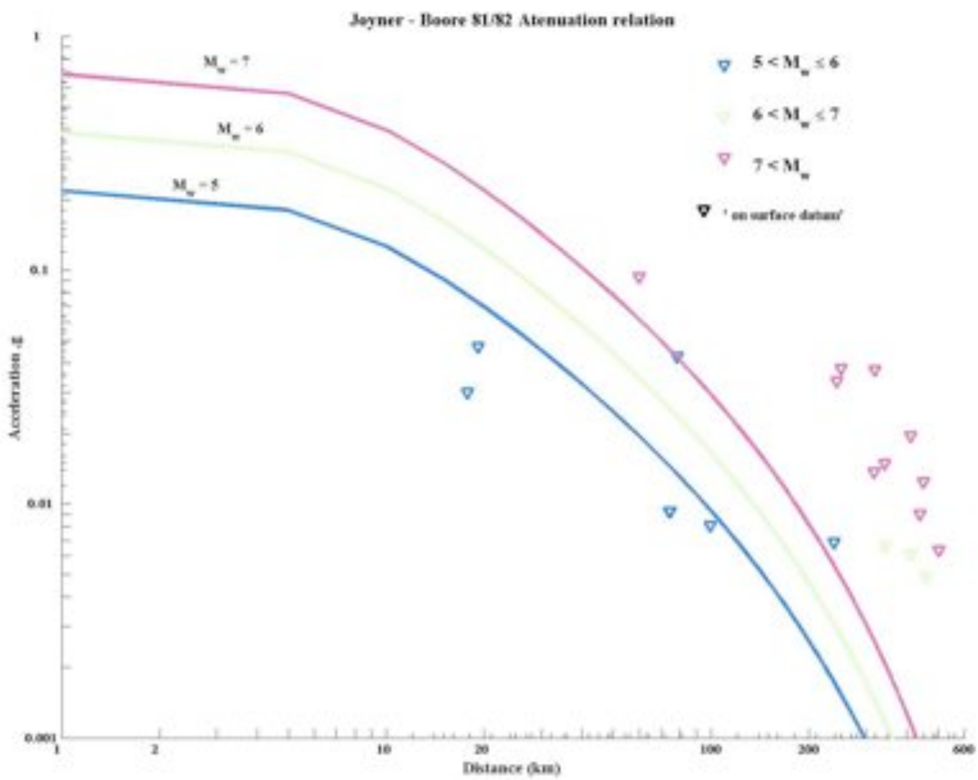

Figure 33 Horizontal peak ground acceleration attenuation relationship, Boore (2005).

4.2.5 Site effect

It has become evident that sedimentary basins may constitute an important factor of site effect. Recent studies have shown that when sedimentary cover lies on top rocks with higher seismic velocities two-dimensional resonance patterns may prolong the duration of shaking and force a large amplification; much larger than the one predicted from similar one-dimensional analysis. This was shown in several simulations (Bard and Bouchon,

1980; Frankel and Stephenson, 2000) and also by field measurements (Frankel et al., 2002).
This kind of site effect was felt during the earthquake of November 1995. Inconsistencies in magnitude between the observed PGA to the GII's PGA model were interpreted as the site effect amplification. These inconsistencies attribute modifications to the PGA model.
As body waves arrive at the edge of the basin they are reflected, in a way that the body wave energy is trapped within the basin, between the free surface and the basin interface. Once trapped, they are reflected back and forth thus increasing the seismic loading (Begin et al., 2005a). The reflection and refraction of the seismic wave may create focusing effect that amplifies the contribution of the seismic energy.
Site effect amplification cannot be taken into account in the CFD model due to the complexity of the problem, but cannot be neglected in terms of the theoretical-parameterization.

4.2.6 Perturbations

Given sufficiently strong shear, instabilities seeded as small amplitude, quasi-random disturbances or 'noise', which is always present in natural flows, grow exponentially dominated by the fastest growing modes. Therefore, in order to employ such instabilities in the numerical model, we need to insert oscillation. This oscillation serves two mechanisms:
i) Singular seismic pulse corresponds to most energetic frequency of earthquakes. Seismic waves considered as a propagating body waves or surface waves (i.e. Rayleigh or Love waves). Surface waves with a frequency ω_0 are generated on a liquid surface when vertically vibrating of the medium is at $\omega=2\omega_0$. The dispersion relation of the medium determines the wavelengths of such waves. The developed wavelengths depend on the physical parameters of the medium and not on the geometry or scale of the boundary. Such incidental seismic wave can create a small perturbation at the interface between the two layers that eventually evolve under shear instability.
Hamiel (1999) conducted several laboratory experiments with layers composed of saturated Kaolinite and Lisan Formation sediments. He used a shaking table in order to examine the dynamic behavior of such sediments under vibration. Three types of waves developed on the surface of the mud layers: solitons, oscillons and global wave patterns. Each of these features can act as a localized initiator for instability.

ii) Imitation of small scale bumps at the interface between layers. The interface between the two layers is not completely flattened due to local sedimentation changes. Those natural bumps can be referred as spacious perturbation that amplifies under shear instability as shown in chapter 3.3.3.

Despite the fact that natural KHI do not necessarily involve perturbations, the external oscillation added to the CFD model may serve the developed instability in the two suggested mechanisms or as a combination of both.

4.2.7 Scale and deformation, *Re* vs. *Ri* number

Instability is a product of the combination of shear and stratification. Simulations show that the layer's thickness affects the shear impact. As we increase the thickness of the mesh, instability grows under stronger shear and deformation takes place at higher ground acceleration values. The fact that the deformation is more intense at thinner layers is not trivial. Since the Reynolds number is linearly dependent on the length-scale (thickness of the layer), we expect the deformation to concur with the increase of the Reynolds number (Figure 34): Larger layers - Higher Re - stronger turbulence.

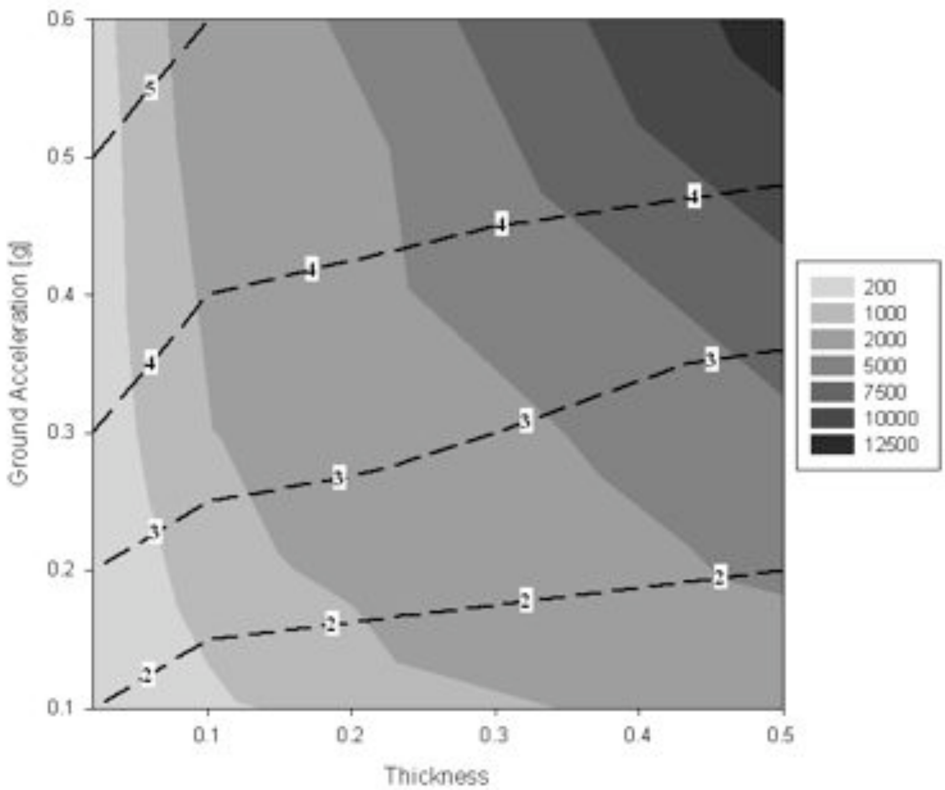

Figure 34 Simulation's Reynolds number. Grey scale shows value of Re number based on the mean velocity, represented by the dashed lines. High Reynolds numbers are compatible with thicker layers at higher velocities.

The dissonance between the calculated Reynolds number and the results of the simulations is clarified as we examine the corresponding Richardson (Ri) number. The Ri number is the dimensionless number that measures the stabilizing influence of the stratification, compared with the destabilizing inertial effects. It is defined by the ratio of the square buoyancy frequency (Brunt-Väisälä) divided by the velocity vertical gradient:

$$Ri = \frac{N^2}{\left(\frac{dU}{dZ}\right)^2}, N^2 = \frac{g}{\rho_m}\frac{\Delta\rho}{H} \qquad (27)$$

Kelvin-Helmholtz instability may occur in a continually stratified fluid in which the density decreases in height. It is possible to show that according to the linear instability theory of a shear flow U(z), KHI can only occur if the Ri < 0.25 (Acheson, 1990).

We present a brief examination of the Richardson number in all cases of simulations. The Brunt-Väisälä frequency is shown calculated according the thickness of the layers and is shown in Table 5, where mean density is ρ_m=1650 kg/m^3 and the deference density is $\Delta\rho$=180 kg/m^3.

Brunt-Väisälä	***Thickness [m]***
44.59091	0.02
8.918182	0.1
1.783636	0.5

Table 5 Values of Brunt-Väisälä frequencies for Ri number calculation in Figure 35.

In Figure 35 it is shown that the values of the Richardson number throughout most simulations is below 0.25, which is the critical value for generating KHI. The dark area in this figure (high values of Ri number) corresponds to the 'no-deformation' area previously presented in Figure 37, which sets a critical minimal shear velocity of ~2 m/s. The figure also shows smaller Ri numbers at the thinner layers; compatible with the CFD results.

As the seismic energy spreads through thicker layers, the energy flux decreases. Weaker energy leads less shear and therefore a flow parcel located at the interface between the layers exhibit less vorticity. This theory is well illustrated by the CFD model. The energy density overcomes the viscous effects and therefore the instability increases.

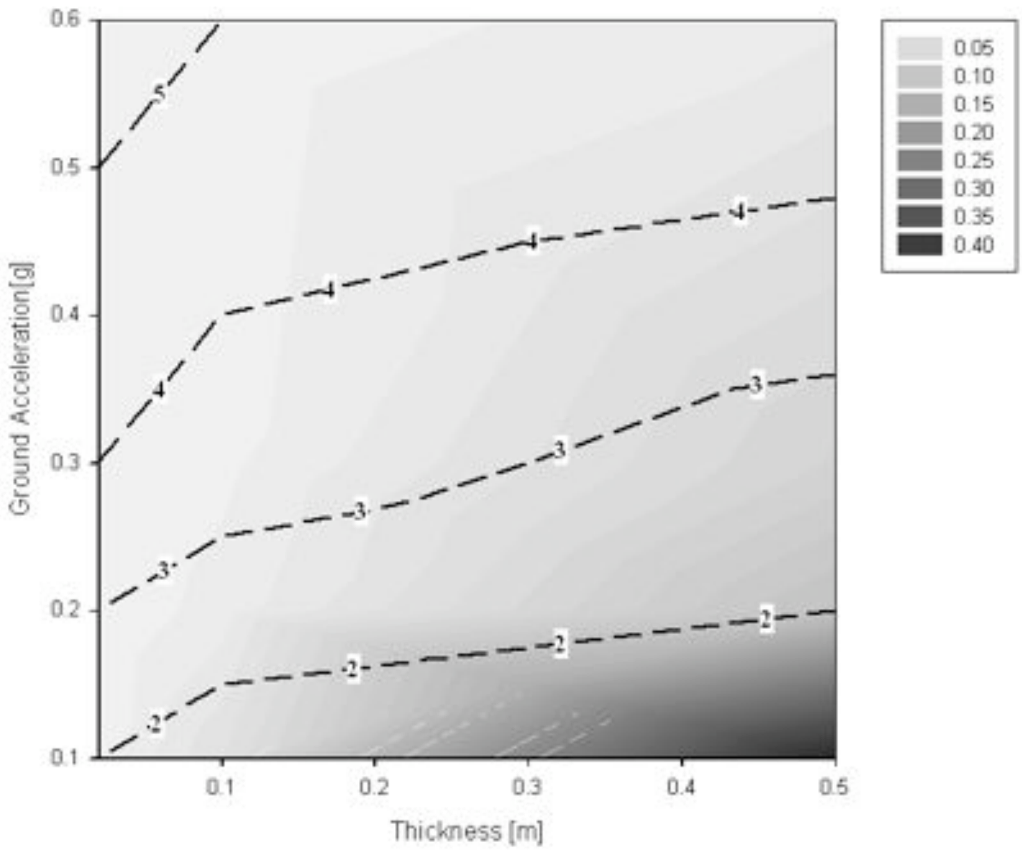

Figure 35 Richardson number. The figure shows the values of Ri number to the Layer Thickness and ground acceleration. Brunt-Väisälä frequency was calculated based on the mean velocity field of the top layer, and marked as white lines. Most of the simulations show values of Ri<0.25.

4.2.8 Direction of flow

The KHI mechanism is based on the principle of shear flow. But the lack of any preferred orientation in ground motion during earthquakes makes it difficult to suggest a shear-like mechanism which follows to a defined and preserved flow direction.

Although field observations serve the KHI hypothesis, due to the constant orientation found in most of the billow like folds it presents us with a non-trivial problem.

The direction of the flow is dictated by the first seismic impact. The velocity of the flow evolves through a process of ratcheting that fed by ground attenuations of the cyclical movements of earthquakes undergo.

This approach manifests the concepts by first motion seismic arrivals of P waves, e.g. "up" and "down" (Figure 36). This terminology is derived from the direction of the first observed motion on the seismogram (up or down). The seismic waves propagate away from hypocenter in all directions with respect to the orientation of the motion along the fault. In some cases the ground first moves away from the source and toward a seismic station, whereas in other cases the ground moves away from the receiver. This sets the orientation of P waves; "up" points compression, and "down" points dilation.

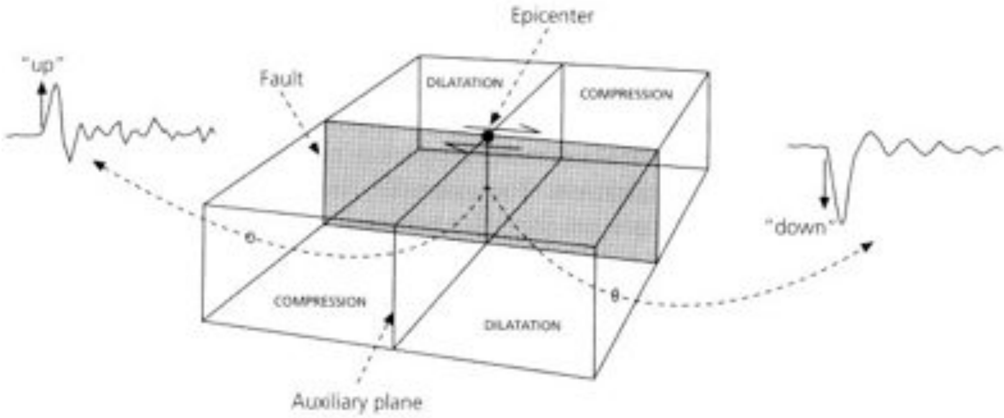

Figure 36 First motions of seismic P waves observed at seismometers located in various directions about the earthquake allow the fault orientation to be determined (Stein S., 2003).

In the case of and earthquake in a distance less than about 100 km, Pg is the first arrival (Lay and Wallace, 1995) and therefore may project by a strong horizontal component.

4.2.9 Turbulent power law

In order to verify the objectiveness of the geometrical analysis employed in our research method, we conduct a brief spectral analysis of several fold types. We examine whether other folds do exhibit geometrical power laws during the process of deformation. This investigation is divided into two parts, based on the sizes of the folds. Small-scale features provided by Ramsay and Huber (1987) and large-scale folds are the measured monoclines of the Syrian Arc Eran (1982).

Most of the folds do not correspond to a clear power fit with poor compatibility of R^2 values. This brief geometrical analysis (presented in Appendix E), shows that power-law-like behavior of the order of -5/3 is exclusive for a fluid-like behavior that follow the rules of turbulent flow such as the Lisan Formation billow-like folds.

4.2.10 End of process

The well-preserved geometrical features along the Lisan Formation indicate a "freezing" mechanism to the process of deformation. Heifetz et al (2005) suggests that this preservation of the billows occurs due to an instantaneous water loss which led to the consolidation of the sediments shortly after the onset of instability (Heifetz et al., 2005). Deformed sediment under shear force have shown displacements of the millimeter to centimeter magnitude, and exhibit lower porosity than the original parent material (Aydin, 1978; Crawford, 2007). These research findings show the collapse of pore pressure in case of *deformation bands* that show decrease of volume as they are formed during coseismic rupture. In this process of consolidation with the decrease of porosity water 'exhausts' from the deformed layers of sediments into upper layers. As the quake fades to a critical point, viscous forces within the sediment overcome the ground momentum and the deformation stops.

Saturated clay may also be treated as a model of *Single-phase continuum* of a *debris flow*. The characteristics of such fluid are determined by the relationship between the operating shear stress and the rate of strain that is called the constitutive law or the consistency (Takahashi, 2007). As the skeletal structure of the laminas is affected by the operation of a shear stress larger than the yield strength, particles disperse within the mass decoupled each other diminishing the resistance of the flow.

4.3 Simulation analysis

The density profiles at simulations time T=1sec show different stages of deformation. We described these stages by 5 main categories: 1) No deformation, 2) Linear, 3) Billows, 4) Roll up, 5) Breccia. The next step is to establish relationships between the ground acceleration, thickness of the deformed layer and the stage of the deformation (Figure 37). We find that the 'Billow-stage' is compatible with the threshold of instability calculated in previous work by Heifetz et al. (2005). They establish a parabolic minimal threshold for instability based on damping factor *r*, the buoyancy frequency and the layer thickness for the onset of linear KHI waves.

$$a/g > \frac{r}{\sqrt{\pi}N} \quad \textbf{(28)}$$

The damping factor represents the viscosity factor in terms of the bulk Rayleigh damping, and is taken as 0.1 Hz.

In addition to Heifetz et al. (2005), Hamiel (1999) also found that the critical acceleration required for the initiation of localized waves in a configuration of vertical shaking of mud layers depends on the thickness of the layers, the vibration frequency and the density of the mud.

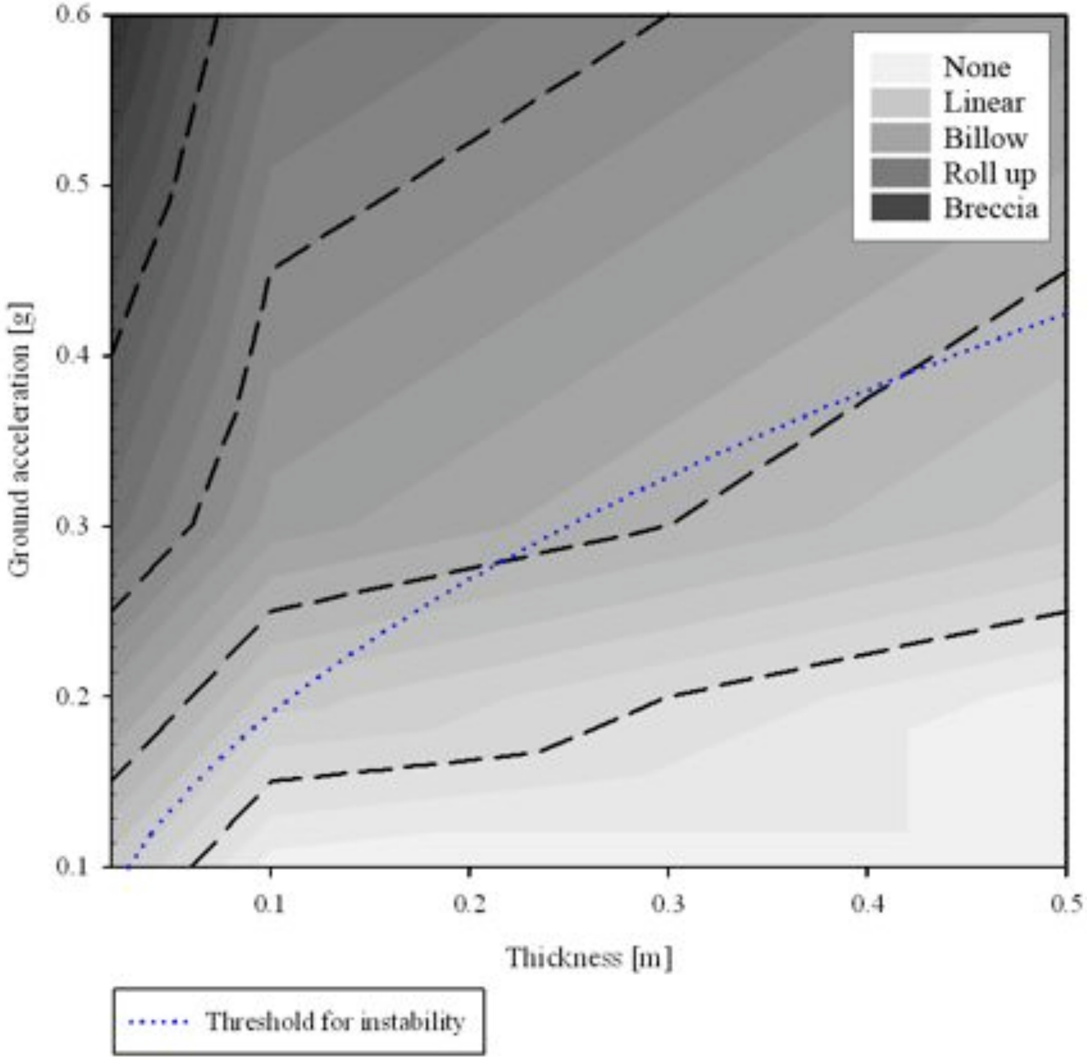

Figure 37 Results of simulations. The contours mark the stages of the KHI process with respect to ground acceleration and the thickness of the layers. The thinner layers tend to deform more rapidly than the thicker layers. The dotted parabolic line marks the threshold for instability (Heifetz et al., 2005).

5 FINAL CONCLUSIONS

Laminated fine-grained sediments can exhibit various forms of deformed structures during earthquake. It is obvious now that the billow-like folds of the Lisan Formation are a product of a shear mechanism. Besides the striking visual similarity of those features to KHI, this research shows that they also have the same dynamical characteristics and physical properties of such a shear mechanism.

Our research examines the behavior of an evolving, stably stratified turbulent shear flow in a two-layer, perturbaised, high-viscous, 2-D rectangle mesh. Simulations show that the natural configuration of the Lisan Formation is capable to produce such deformation as the result of a shear force. All dynamic and physical conditions necessary for an established shear instability exist within the Lisan Formation in the DSB region:

Stably stratified density gradient: The natural lacustrine sedimentation of Lake Lisan creates a density gradient; light layer of sediments on top of denser layers.

Energy source: Proximity to active faults systems corroborates the conjecture that these deformations are indeed seismites. Regional earthquakes induce sufficient energy source for seismic waves for a pressure gradient force and ground acceleration. CFD simulations show that a ground acceleration of ~0.2g is sufficient in order to create a KHI billow.

Shear: The configuration of the density gradient and ground acceleration produces a setup of shear instability along sediments at the lake's floor. The clear orientation preserved through continuous folded sediments is evidence to the direction of the flow.

Perturbation: Seismic energy and natural fluctuations along the interface between the two layers.

Turbulence: Spectral analysis of the billow like structures along the Lisan Formation show a uniform power fit in the order of the Kolmogorov power law -5/3. This resemblance is not accidental if we consider that these folds were generated under turbulent conditions.

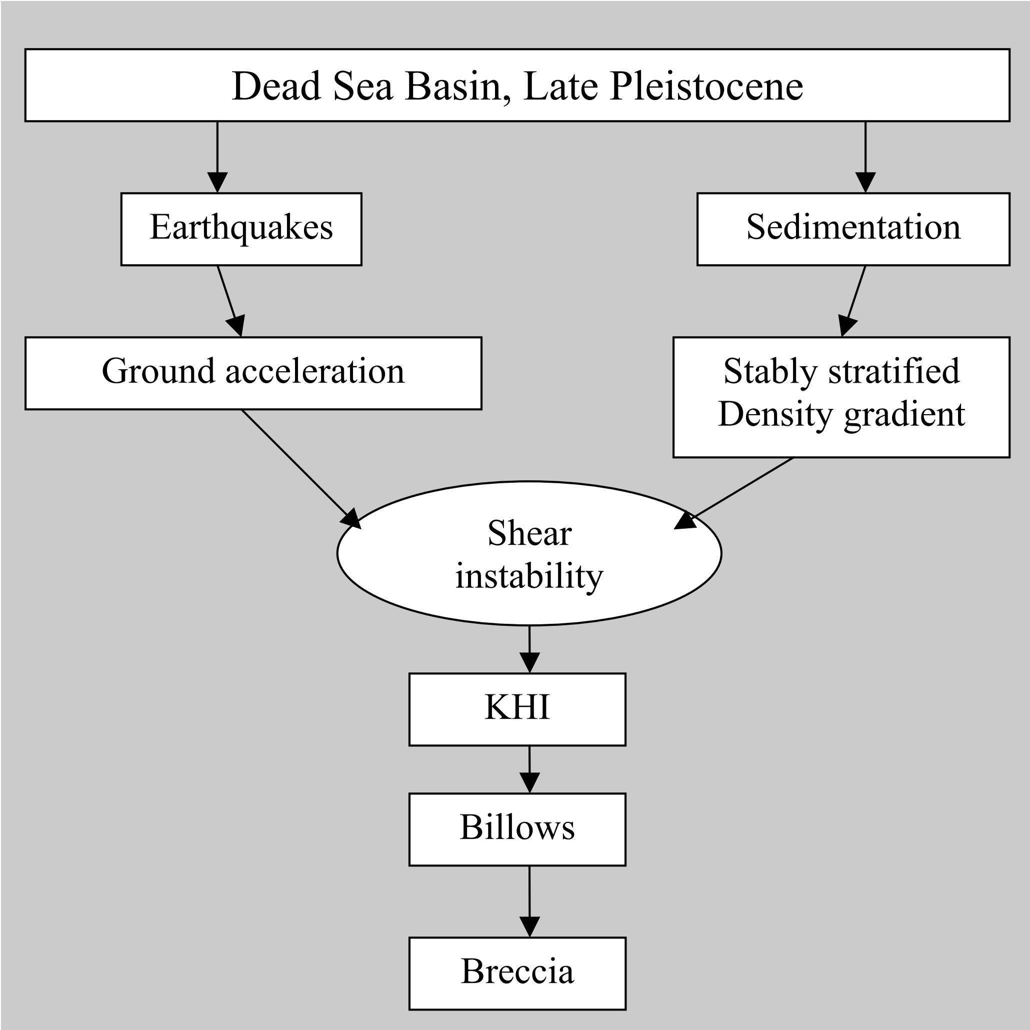

Figure 38 Schematic flow chart of the KHI model.

5.1 Field observations vs. CFD

The stages of deformation were defined according to the most deformed feature at simulation time T=1 sec. We find that these 'stages' (which determine the degree of deformation) show striking resemblance to the soft deformations patterns and correlate to the degree of acceleration parameter in addition to the layer thickness. Figure 39 shows this relationship in the case where the mesh thickness is 40cm. In this figure we present compatible field features which were photographed and cropped under the same dimensions as the mesh displayed on the right.

During simulations the stage of roll-up use up a significant and rather long part of the numerical simulation duration. In contrast, we did not find many of these rolled-up features in the field compared with the rather large variety of breccias and billow-like folds. We suspect that during an earthquake the consistency of the momentum might be terminated, resulting in the production of the breccias at earlier stages.

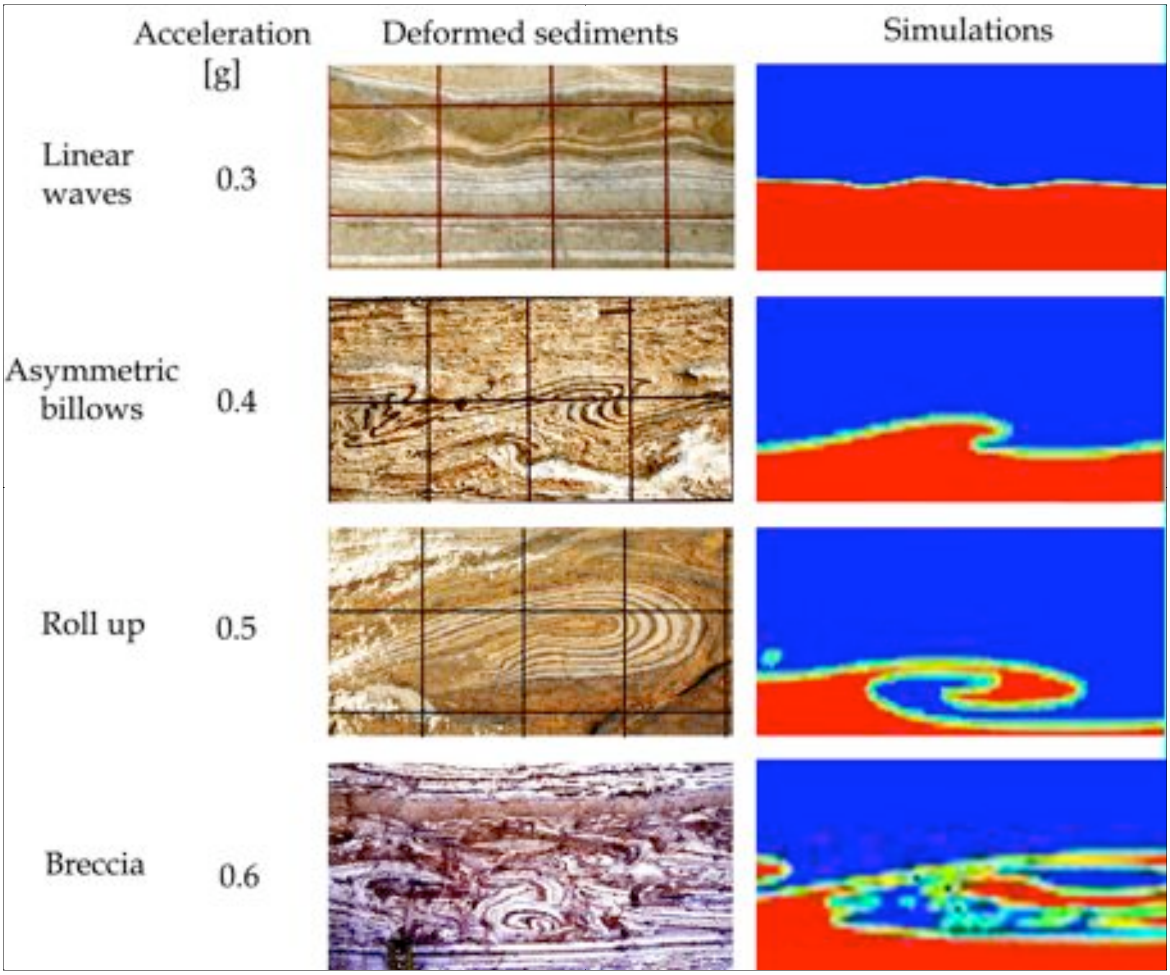

Figure 39. Visual comparison between deformed sediments to CFD simulations. Scale of field photographs are exactly as the CFD model captures 20 x 40 cm, and represent the density profile at T=1 sec.

5.2 Future direction

The final phase of this research is a theoretical attempt to evaluate earthquake's intensity by a geometrically measuring of a single billow-like fold. CFD simulations show that the stage, in which the billows are created at simulation time of 1 sec, corresponds to the value of the PGA. Using attenuation equation (Boore, 2005) we convert the ground acceleration to earthquake magnitude at a specific distance and correlate it to the degree of deformation (Figure 40).

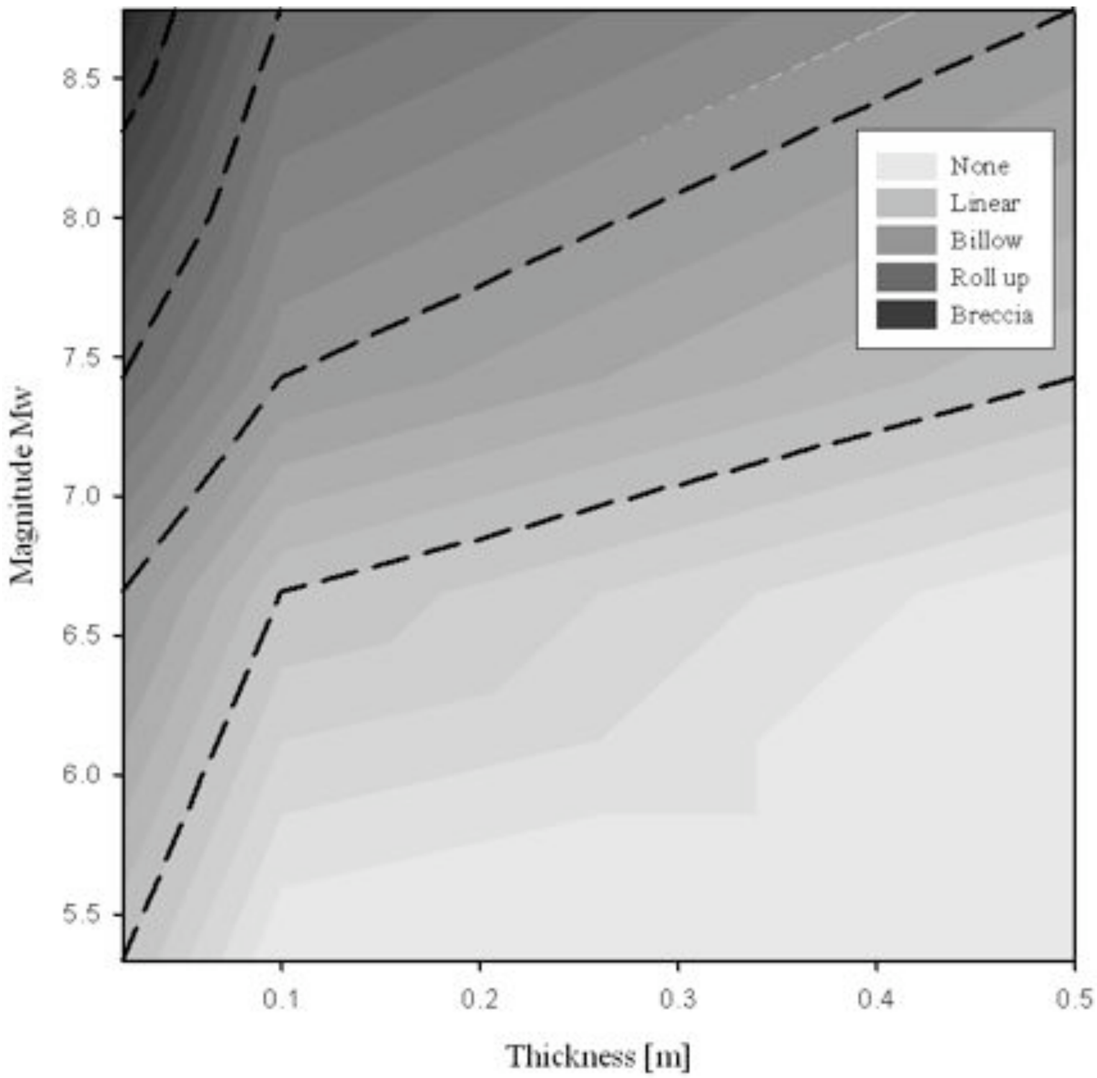

Figure 40 Stages of deformation at a distance of 10 km from the fault. Magnitude calculated according to Boore attenuation equation (2005) with respect to the CFD model.

6 BIBLIOGRAPHY

Acheson, D.J., 1990. Elementary Fluid Dynamics. Oxford Applied Mathematics and Computing Science Series. Oxford University Press, 397 pp.

Agnon, A., Migowski, C. and Marco, S., 2006. Interclust Breccias in Laminated Sequences Reviewed: Recorders of Paleo-earthquakes Geological Society of America, 401: 195-214.

Amit, R., Zilberman, E., Enzel, Y. and Porat, N., 2002. Paleoseismic evidence for time dependency of seismic response on a fault system in the southern Arava Valley, Dead Sea rift, Israel. Geological Society of America Bulletin, 114(2): 192-206.

Amy, L.A., Peakall, J. and Talling, P.J., 2005. Density- and viscosity-stratified gravity currents: Insight from laboratory experiments and implications for submarine flow deposits. Sedimentary Geology, 179(1-2): 5-29.

Arkin, Y.a., 1985. Deformation of Laminated Sediments of the Dead Sea. GSI Current Research, 5: 57-61.

Aydin, A., 1978. Small Faults Formed as Deformation Bands in Sandstone. Pure and Applied Geophysics, 116(4-5): 913-930.

Bachmann, G.H. and Aref, M.A.M., 2005. A seismite in Triassic gypsum deposits (Grabfeld formation, ladinian), southwestem Germany. Sedimentary Geology, 180(1-2): 75-89.

Baker, V.R., Kochel, R.C. and C., P.P., 1988. Flood Geomorphology. Wiley-Interscience, 503 pp.

Bard, P.Y. and Bouchon, M., 1980. The Seismic Response of Sediment-Filled Valleys .2. the Case of Incident P-Waves and Sv-Waves. Bulletin of the Seismological Society of America, 70(5): 1921-1941.

Bartov, Y. and Sagy, A., 2004. Late Pleistocene extension and strike-slip in the Dead Sea Basin. Geological Magazine, 141(5): 565-572.

Bartov, Y., Stein, M., Enzel, Y., Agnon, A. and Reches, Z., 2002. Lake levels and sequence stratigraphy of Lake Lisan, the late Pleistocene precursor of the Dead Sea. Quaternary Research, 57(1): 9-21.

Begin, Z.B., Louie, J.N., Marco, S. and Ben-Avraham, Z., 2005a. Prehistoric Seismic Basin Effects in the Dead Sea Pull-apart, Geological Survey of Israel.

Begin, Z.B., Steinberg, D.M., Ichinose, G.A. and Marco, S., 2005b. A 40,000 year unchanging seismic regime in the Dead Sea rift. Geology, 33(4): 257-260.

Ben-Menahem, A., 1991. 4000 Years of Seismicity Along the Dead-Sea Rift. Journal of Geophysical Research-Solid Earth, 96(B12): 20195-20216.

Bernhardt, P.A., 2002. The modulation of sporadic-E layers by Kelvin-Helmholtz billows in the neutral atmosphere. Journal of Atmospheric and Solar-Terrestrial Physics, 64(12-14): 1487-1504.

Boore, D.M., 2005. Equations for estimating horizontal response spectra and peak acceleration from western north American earthquakes: A summary of recent work (vol 68, pg 128, 1997). Seismological Research Letters, 76(3): 368-369.

Bosak, T. and Ingersoll, A.P., 2002. Shear instabilities as a probe of Jupiter's atmosphere. Icarus, 158(2): 401-409.

Brodsky, E.E., Rowe, C.D., Meneghini, F. and Moore, J.C., 2009. A geological fingerprint of low-viscosity fault fluids mobilized during an earthquake. Journal of Geophysical Research-Solid Earth, 114.

Crawford, R., 2007. EARTHQUAKE HISTORY, MICROSTRUCTURE, AND FAULT FRICTIONAL PROPERTIES OF NEAR-SURFACE SEDIMENTS ON THE NORTHERN SAN ANDREAS FAULT AT ALDER CREEK, CALIFORNIA, Humboldt State University, 79 pp.

Csato, I., Kendall, C.G.S., Nairn, A.E.M. and Baum, G.R., 1997. Sequence stratigraphic interpretations in the southern Dead Sea basin, Israel. Geological Society of America Bulletin, 109(11): 1485-1501.

DeSilva, I.P.D., Fernando, H.J.S., Eaton, F. and Hebert, D., 1996. Evolution of Kelvin-Helmholtz billows in nature and laboratory. Earth and Planetary Science Letters, 143(1-4): 217-231.

El Isa, Z.H. and Mustafa, H., 1986. Earthquake Deformations in the Lisan Deposits and Seismotectonic Implications. Geophysical Journal of the Royal Astronomical Society, 86(2): 413-424.

Faers, M.A. and Kneebone, G.R., 1999. Application of rheological measurements for probing the sedimentation of suspension concentrate formulations. Pesticide Science, 55(3): 312-325.

Frankel, A. and Stephenson, W., 2000. Three-dimensional simulations of ground motions in the seattle region for earthquakes in the Seattle fault zone. Bulletin of the Seismological Society of America, 90(5): 1251-1267.

Frankel, A.D., Carver, D.L. and Williams, R.A., 2002. Nonlinear and linear site response and basin effects in Seattle for the M 6.8 Nisqually, Washington, earthquake. Bulletin of the Seismological Society of America, 92(6): 2090-2109.

Galmiche, M. and Hunt, J.C.R., 2002. The formation of shear and density layers in stably stratified turbulent flows: linear processes. Journal of Fluid Mechanics, 455: 243-262.

Garfunkel, Z., 1981. Internal Structure of the Dead-Sea Leaky Transform (Rift) in Relation to Plate Kinematics. Tectonophysics, 80(1-4): 81-108.

Garfunkel, Z., Zak, I. and Freund, R., 1981. Active Faulting in the Dead-Sea Rift. Tectonophysics, 80(1-4): 1-26.

Garfunkel.Z and Horowitz, A., 1966. Upper Tertiary and Quaternary Morphology of Negev Israel. Israel Journal of Earth Sciences, 15(3): 101-&.

Gilead, U. and Karnieli, A., 2004. Locating potential vicarious calibration sites for high-spectral resolution sensors in the Israeli Negev Desert by GIS analysis. Post-Launch Calibration of Satellite Sensors – Morain & Budge (eds).

Ginzburg, A., Makris, J., Fuchs, K. and Prodehl, C., 1981. The Structure of the Crust and Upper Mantle in the Dead-Sea Rift. Tectonophysics, 80(1-4): 109-119.

Gotze, H.J. et al., 2007. Integrated 3D density modelling and segmentation of the Dead Sea Transform. International Journal of Earth Sciences, 96(2): 289-302.

Greenbaum, N., Porat, N., Rhodes, E. and Enzel, Y., 2006. Large floods during late Oxygen Isotope Stage 3, southern Negev desert, Israel. Quaternary Science Reviews, 25(7-8): 704-719.

Greenbaum, N., Schick, A.P. and Baker, V.R., 2000. The palaeoflood record of a hyperarid catchment, Nahal Zin, Negev Desert, Israel. Earth Surface Processes and Landforms, 25(9): 951-971.

H.Shmase, I., 1962. Mechanics of Fluids. Kogakusha Co., Ltd, Tokyo, Japan.

Hamiel, Y., 1999. Dynamic Behavior Under Vibration: Laboratory Experiments with Sediments, Wave Propagation in Non-linear Elastic Medium and Possible Implications to Earthquakes, The Hebrew University of Jerusalem, Jerusalem, 61 pp.

Heifetz, E., Agnon, A. and Marco, S., 2005. Soft sediment deformation by Kelvin Helmholtz Instability: A case from Dead Sea earthquakes. Earth and Planetary Science Letters, 236(1-2): 497-504.

Hofstetter, R., Klinger, Y., Amrat, A.Q., Rivera, L. and Dorbath, L., 2007. Stress tensor and focal mechanisms along the Dead Sea fault and related structural elements based on seismological data. Tectonophysics, 429(3-4): 165-181.

J. B. Currie, H.W.P., and R. P. Trump 1962. Development of folds in sedimentary strata Geological Society of America, 73: 655-673.

John J.Ramsay , M.I.H., 1987. The Techniques of Modern Stractural Geology, 2. ACADEMIC PRESS INC, San Diego, 400 pp.

Joyner, W.B. and Boore, D.M., 1981. Peak Horizontal Acceleration and Velocity from Strong-Motion Records Including Records from the 1979 Imperial-Valley, California, Earthquake. Bulletin of the Seismological Society of America, 71(6): 2011-2038.

Kaufman, A., Yechieli, Y. and Gardosh, M., 1992. Reevaluation of the Lake-Sediment Chronology in the Dead-Sea Basin, Israel, Based on New Th-230/U Dates. Quaternary Research, 38(3): 292-304.

Ken-Tor, R. et al., 2001. High-resolution geological record of historic earthquakes in the Dead Sea basin. Journal of Geophysical Research-Solid Earth, 106(B2): 2221-2234.

Klinger, Y., Avouac, J.P., Dorbath, L., Abou Karaki, N. and Tisnerat, N., 2000. Seismic behaviour of the Dead Sea fault along Araba valley, Jordan. Geophysical Journal International, 142(3): 769-782.

Kolmogorov, A.N., 1941a. Dissipation of energy in locally isotropic turbulence. C.R. (Doklady) Acad. Sci. URSS (N.S.), 32: 16-18.

Kolmogorov, A.N., 1941b. The local structure of turbulence in an incompressible fluid for very large Reynolds numbers. C.R. (Doklady) Acad. Sci. URSS (N.S.), 30: 301-305.

Kramer, S.L., Arduino, P. and David A. Baska, P.L., 2002. Dynamic Stiffness of Piles in Liquefiable Soils. WA-RD 514.1, University of Washington,, Washington.

Lay, T. and Wallace, T.C., 1995. Modern global seismology. Academic Press, San Diego.

Lesieur, M., 1997. Turbulence in Fluids. KLUWER ACADEMIC PUBLISHERS.

Levi, T., Weinberger, R., Aifa, T., Eyal, Y. and Marco, S., 2006. Earthquake-induced clastic dikes detected by anisotropy of magnetic susceptibility. Geology, 34(2): 69-72.

Li, H. and Yamazaki, H., 2001. Observations of a Kelvin-Helmholtz billow in the ocean. J Oceanogr, 57(6): 709-721.

Lioubashevski, O., Hamiel, Y., Agnon, A., Reches, Z. and Fineberg, J., 1999. Oscillons and propagating solitary waves in a vertically vibrated colloidal suspension. Physical Review Letters, 83(16): 3190-3193.

Liyanathirana, D.S. and Poulos, H.G., 2002. Numerical simulation of soil liquefaction due to earthquake loading. Soil Dynamics and Earthquake Engineering, 22(7): 511-523.

Lowe, D.R., 1975. Water Escape Structures in Coarse-Grained Sediments. Sedimentology, 22(2): 157-204.

Manneville, P., 2004. Instabilities, Chaos and Turbulence: An Introduction to Nonlinear Dynamics and Complex Systems. Imperial College Press, 391 pp.

Marco, S. and Agnon, A., 1995. Prehistoric Earthquake Deformations near Masada, Dead-Sea Graben. Geology, 23(8): 695-698.

Marco, S. and Agnon, A., 2005. High-resolution stratigraphy reveals repeated earthquake faulting in the Masada Fault Zone, Dead Sea Transform. Tectonophysics, 408(1-4): 101-112.

Marco, S., Rockwell, T.K., Heimann, A., Frieslander, U. and Agnon, A., 2005. Late Holocene activity of the Dead Sea Transforrn revealed in 3D palaeoseismic trenches on the Jordan Gorge segment. Earth and Planetary Science Letters, 234(1-2): 189-205.

Marco, S., Stein, M., Agnon, A. and Ron, H., 1996. Long-term earthquake clustering: A 50,000-year paleoseismic record in the Dead Sea Graben. Journal of Geophysical Research-Solid Earth, 101(B3): 6179-6191.

Marco, S., Weinberger, R. and Agnon, A., 2002. Radial clastic dykes formed by a salt diapir in the Dead Sea Rift, Israel. Terra Nova, 14(4): 288-294.

Marshall, L., 2004. Computational Cloud Dynamic, Fluent news.

Mart, Y., Ryan, W.B.F. and Lunina, O.V., 2005. Review of the tectonics of the Levant Rift system: the structural significance of oblique continental breakup. Tectonophysics, 395(3-4): 209-232.

Mastrano, A. and Melatos, A., 2005. Kelvin-Helmholtz instability and circulation transfer at an isotropic-anisotropic superfluid interface in a neutron star. Monthly Notices of the Royal Astronomical Society, 361(3): 927-941.

McComb, W.D., 1995. Theory of Turbulence. Reports on Progress in Physics, 58(10): 1117-1205.

Mehta, R.D., 1991. Effect of Velocity Ratio on Plane Mixing Layer Development - Influence of the Splitter Plate Wake. Experiments in Fluids, 10(4): 194-204.

Nakamura, Y., 1996. Vortex shedding from bluff bodies with splitter plates. Journal of Fluids and Structures, 10(2): 147-158.

Obukhov, A.M., 1983. Kolmogorov Flow and Laboratory Simulation of It. Russian Mathematical Surveys, 38(4): 113-126.

Owen, G., 1996. Experimental soft-sediment deformation: Structures formed by the liquefaction of unconsolidated sands and some ancient examples. Sedimentology, 43(2): 279-293.

Peltier, W.R., Halle J, 1978. The Evolution of Finite Amplitude Kelvin-Helmholtz Billows. Geophys. Astrophys. Fluid Dynamics, 10: 53-87.

Phillips, O.M., 1991. The Kolmogorov Spectrum and Its Oceanic Cousins - a Review. Proceedings of the Royal Society of London Series a-Mathematical Physical and Engineering Sciences, 434(1890): 125-138.

Quennell, A.M., 1958. The Structure and Evolution of the Dead Sea Rift. Geological society of London, 64: 1-64.

Ramaprabhu, P. and Andrews, M.J., 2004. On the initialization of Rayleigh-Taylor simulations. Physics of Fluids, 16(8): L59-L62.

Ramsay, J.J., Martini I.Huber, 1987. The Techniques of Modern Stractural Geology, 2. ACADEMIC PRESS INC, San Diego, 400 pp.

Rodriguez-Lopez, J.P., Melendez, N., Soria, A.R., Liesa, C.L. and Van Loon, A.J., 2007. Lateral variability of ancient seismites related to differences in sedimentary facies (the synrift Escucha Formation, mid-Cretaceous, eastern Spain). Sedimentary Geology, 201(3-4): 461-484.

Rossetti, D.D., 1999. Soft-sediment deformation structures in late Albian to Cenomanian deposits, Sao Luis Basin, northern Brazil: evidence for palaeoseismicity. Sedimentology, 46(6): 1065-1081.

Rotter, J., Fernando, H.J.S. and Kit, E., 2007. Evolution of a forced stratified mixing layer. Physics of Fluids, 19(6).

Saffarini, H.S., 2000. Ground motion characteristics of the November 1995 Aqaba earthquake. Engineering Structures, 22(4): 343-351.

Seilache.A, 1969. Fault-graded beds interpreted as seismites. Sedimentology, 13(1-2): 155-&.

Shearer, E. and Fruh, W.G., 1999. Kelvin-Helmholtz instability in a continuously forced shear flow. Physics and Chemistry of the Earth Part B-Hydrology Oceans and Atmosphere, 24(5): 487-492.

Smyth, W.D., 2003. Secondary Kelvin-Helmholtz instability in weakly stratified shear flow. Journal of Fluid Mechanics, 497: 67-98.

Smyth, W.D., 2004. Kelvin-Helmholtz billow evolution from a localized source. Quarterly Journal of the Royal Meteorological Society, 130(603): 2753-2766.

Smyth, W.D. and Moum, J.N., 2000. Anisotropy of turbulence in stably stratified mixing layers. Physics of Fluids, 12(6): 1343-1362.

Snieder, R. and van den Beukel, A., 2004. The liquefaction cycle and the role of drainage in liquefaction. Granular Matter, 6(1): 1-9.

Stein, M., 2001. The sedimentary and geochemical record of Neogene-Quaternary water bodies in the Dead Sea Basin - inferences for the regional paleoclimatic history. Journal of Paleolimnology, 26(3): 271-282.

Stein, M. et al., 1997. Strontium isotopic, chemical, and sedimentological evidence for the evolution of Lake Lisan and the Dead Sea. Geochimica Et Cosmochimica Acta, 61(18): 3975-3992.

Stein S., W.M., 2003. An introduction to seismology, earthquakes, and earth structure Malden, MA : Blackwell Pub.

Strang, E.J. and Fernando, H.J.S., 2001. Entrainment and mixing in stratified shear flows. Journal of Fluid Mechanics, 428: 349-386.

Suppe, J., 1985. Principles of Structural Geology. Prentice-Hall, New Jersy.

Takahashi, T., 2007. Debris flow: mechanics, prediction and countermeasures. Routledge.

Thacker, W.C. and Lavelle, J.W., 1977. 2-Phase Flow Analysis of Hindered Settling. Physics of Fluids, 20(9): 1577-1579.

Thorpe, S.A., 1973. Experiments on Instability and Turbulence in a Stratified Shear-Flow. Journal of Fluid Mechanics, 61(DEC18): 731-&.

Torfstein, A., Gavrieli, I., Katz, A., Kolodny, Y. and Stein, M., 2008. Gypsum as a monitor of the paleo-limnological-hydrological conditions in Lake Lisan and the Dead Sea. Geochimica Et Cosmochimica Acta, 72(10): 2491-2509.

Turner, J.S., 1973. Buoyancy Effects in Fluids. Cambridge University Press.

Walley, C.D., 1998. Some outstanding issues in the geology of Lebanon and their importance in the tectonic evolution of the Levantine region. Tectonophysics, 298(1-3): 37-62.

Weber, M. et al., 2004. The crustal structure of the Dead Sea Transform. Geophysical Journal International, 156(3): 655-681.

Werne, J. and Fritts, D.C., 1999. Stratified shear turbulence: Evolution and statistics. Geophysical Research Letters, 26(4): 439-442.

Werne, J. and Fritts, D.C., 2001. Anisotropy in a stratified shear layer. Physics and Chemistry of the Earth Part B-Hydrology Oceans and Atmosphere, 26(4): 263-268.

Zheng, Y.Q., Fan, J.R., Luo, K. and Cen, K., 2004. Direct numerical simulation on the particle dispersion by the vortex structures in a three-dimensional mixing layer: the roll-up. Powder Technology, 146(1-2): 102-110.

Zilberman, A. et al., 2008. Lidar study of aerosol turbulence characteristics in the troposphere: Kolmogorov and non-Kolmogorov turbulence. Atmospheric Research, 88(1): 66-77.

Appendix A – Folds Bank

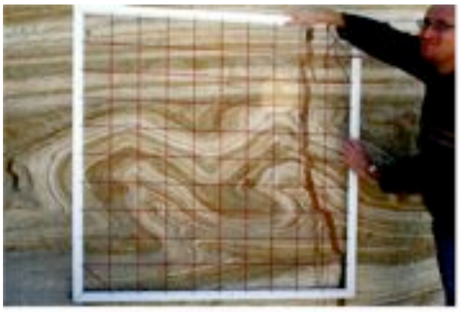

4056

4031

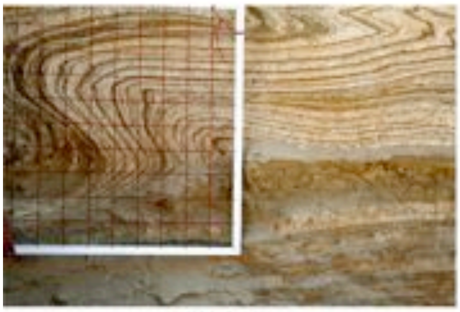

4085

4037

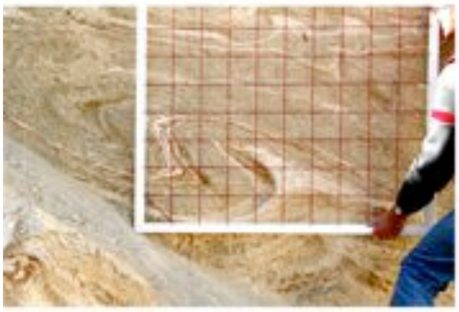

4089

4072

4068

4121

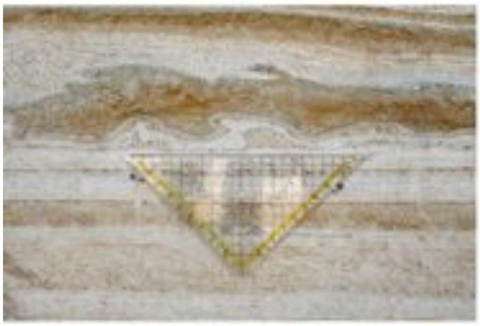

4065

4079

4048

4082

4075

4039

6827

4161


3914


3937


3936


3943

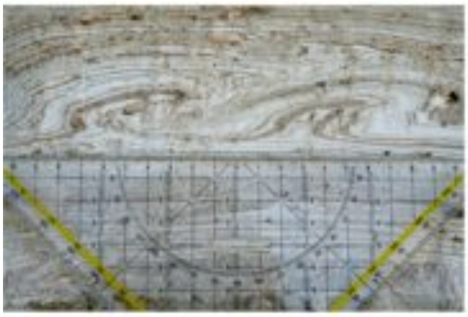
3950

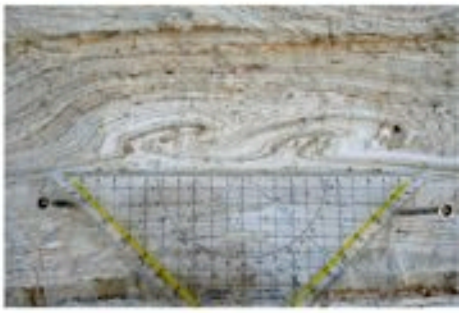
3949


3988


3975

3992

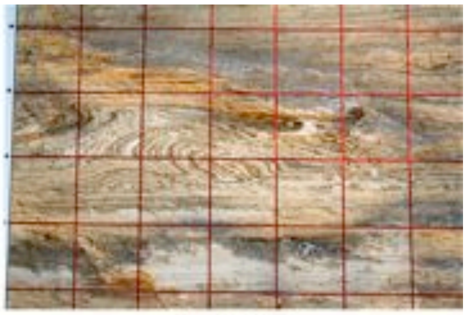

3925

3988

All folds were photographed along the Lisan Formation, Dead Sea basin. The photograph's numbers are used for cataloging purposes only. The photograph numbers starting with 3 were taken at Nahal Havarey Masada and photograph numbers starting with 4 were taken at Nahal Peratzim.

Appendix B - UDF

```
#include "udf.h"
/*input zone*****************************************************/
#define freq 1.0 /*frequency of oscillation*/
#define amp 0.005 /*hight of oscillation*/
#define g 9.81
#define v2 1.0 /*velocity inlet of mud2*/
#define A 0.2 /*acceleration a/g*/
#define alpha1 0.0 /*volume of fuid fraction of the mud1*/
#define alpha2 1.0 /*volume of fuid fraction of the mud2*/
#define PI 3.14159
/***************************************************************/
DEFINE_PROFILE(velocity_beater, thread, nv)
{
face_t f;
real flow_time = RP_Get_Real("flow-time");
real x [ND_ND];
real x0;
x0=amp*sin(2.*PI*freq*flow_time);
begin_f_loop(f, thread)
{
F_CENTROID(x, f, thread);
if(x[1]>=x0)
{
F_PROFILE(f, thread, nv) = 1+A*g*flow_time;
}
else
{
F_PROFILE(f, thread, nv) = v2;
}
}
end_f_loop(f, thread)
```

```
}
DEFINE_PROFILE(density_beater, thread, nv)
{
face_t f;
real flow_time = RP_Get_Real("flow-time");
real x[ND_ND];
real x0;
x0 = amp*sin(2.*PI*freq*flow_time);
begin_f_loop(f, thread)
{
F_CENTROID (x, f, thread);
if(x[1]>=x0)
{
F_PROFILE(f, thread, nv) = alpha1;
}
else
{
F_PROFILE(f, thread, nv) = alpha2;
}
}
end_f_loop(f, thread)
}
```

Appendix C

The physical restrictions of the VOF model are as follow: the flow must be incompressible, heat transfer is not available, species of mixing and reacting flows cannot be modeled and the LES (large eddy simulation) turbulence model cannot be used.
We choose the laminar solver in order to observe the development of instability through the stages of laminar to turbulent.
Convergence criteria set to 0.0005 for the residual continuity and 0.00001 for the X and Y velocities. Parameters of the VOF model were set to the standard values as it is advised in Fluent help. Other parameters such as *'Solution Controls'* set as follows:
Scheme: geo-reconstruct
Courant number: 0.25
Pressure velocity coupling: simple
Momentum: first order
Pressure: standard

Appendix D

measurements	*R2*	*Power Fit*	*figure*
5	0.95	-1.19	3975d
5	0.89	-1.42	3975c
7	0.81	-2.085	3975b
3	0.3	-0.4	3936
4	0.556	-0.723	3950
7	0.98	-1.56	3988
7	0.993	-1.914	3992
6	0.9	-1.96	3925
4	0.925	-0.68	3914
6	0.98	-1.76	4085
5	0.83	-3.25	4089
5	0.913	-2.83	4056
6	0.71	-1.32	4068
14	0.96	-1.828	4039
3	0.88	-1.76	4065
5	0.97	-1.4	4037
4	0.9	-1.69	4048
5	0.97	-1.85	4061
6	0.9	-0.8	4075
5	0.97	-1.7	6827

Table 6 Calculated power fits to fold-packets. We also present the number of single laminas which was measure in each fold-packet, along with R^2 value.

Appendix E

Spectral analysis of various types of folds

Small scale folds

Seven different multilayer folds are spectrally analyzed within this section. The fold figures and the interpretation of the mechanism provided in text book by Ramsay and Huber (1987) are displayed in Figure 42. We perform geometrical measurements for each of the folds, measuring the amplitude and wavelength (up to 40 single billows in each photograph). After obtaining more then 130 different single measurements of amplitude and wavelength, we produce an energy spectra, square amplitude to wave-number (as presented in previous chapters). The mean power fit of measured folds is presented in Table 7 along with the values of R^2.

Figure	*Power fit*	*Error [R^2]*
a	$A2=0.3k^{-1.7}$	0.65
b	$A2=2.7k^{-1.27}$	0.62
c	$A2=0.23k^{-2.07}$	0.59
d	$A2=0.28k^{-1.89}$	0.72
e	$A2=5.2k^{-0.42}$	0.07
f	$A2=8.65k^{-0.53}$	0.16
g	$A2=8.35k^{-0.88}$	0.2

Table 7 Power fit and calculated error of fold in Figure 42.

The power fit values of the folds show high variance from -0.42 up to -2.07, with low suitability (R^2) of 0.2 to 0.72 (

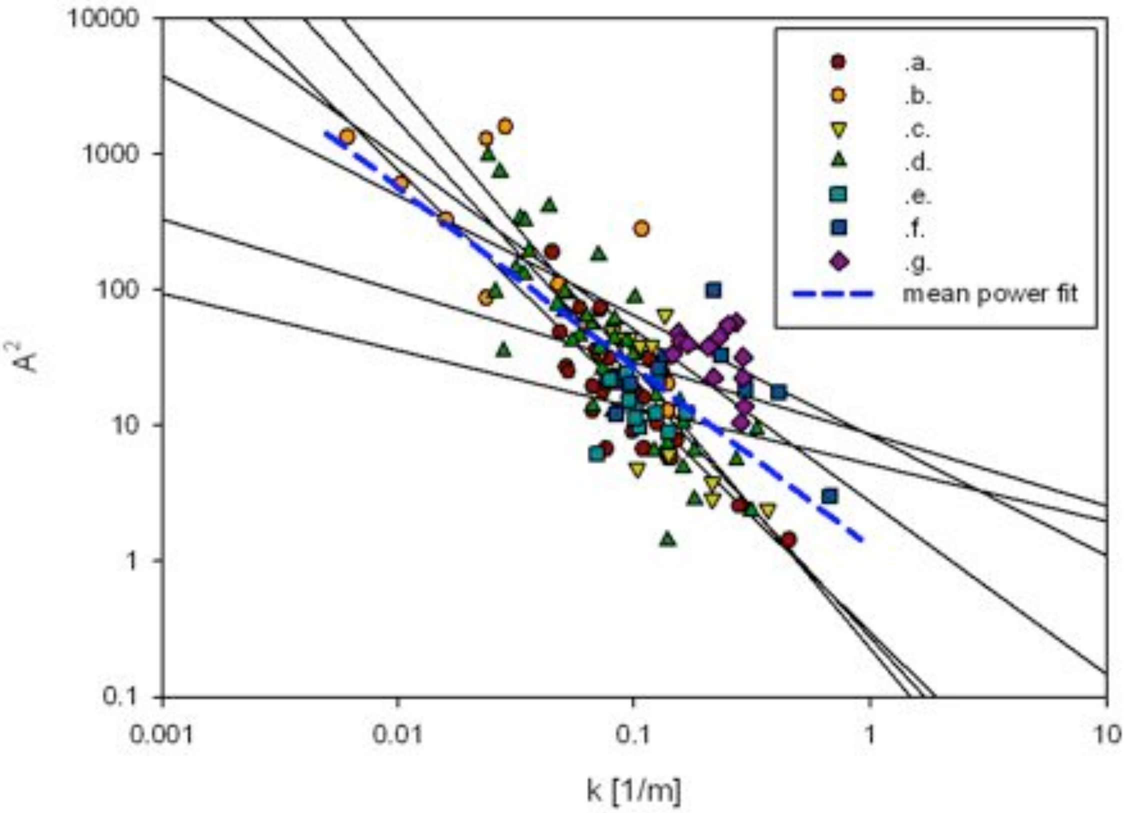

Figure 41). Mean power fit was calculated: -1.32, with R^2 value of 0.51. All the power fits show low values of R^2, therefore we can say that our attempt to globally quantify the folds shown in Figure 42 by the tool of spectral analysis has failed. These kinds of folds could not be compared based on amplitude square to wave number ratio, probably due to the variance of flow-based mechanisms to complex and non-linear processes such as buckling and compression during folding.

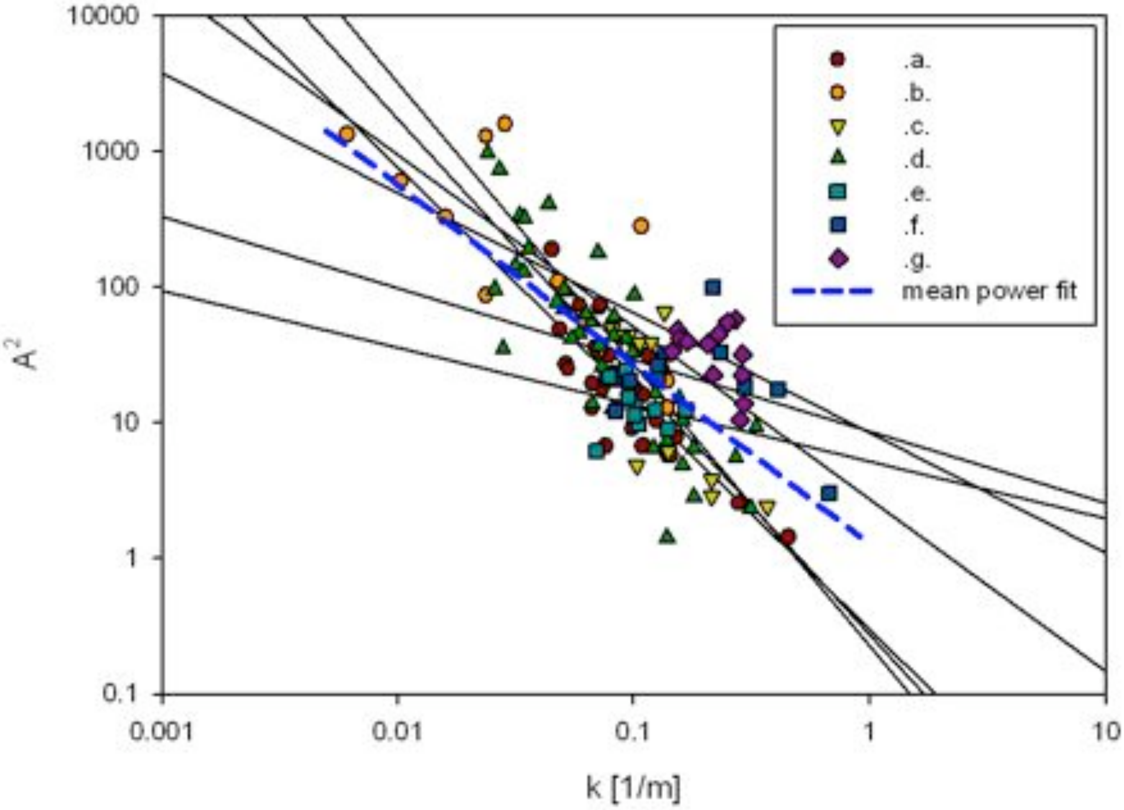

Figure 41 Spectral analysis of various folds. Mean power fit :$A^2=1.27k^{-1.32}$,$R^2=0.51$.

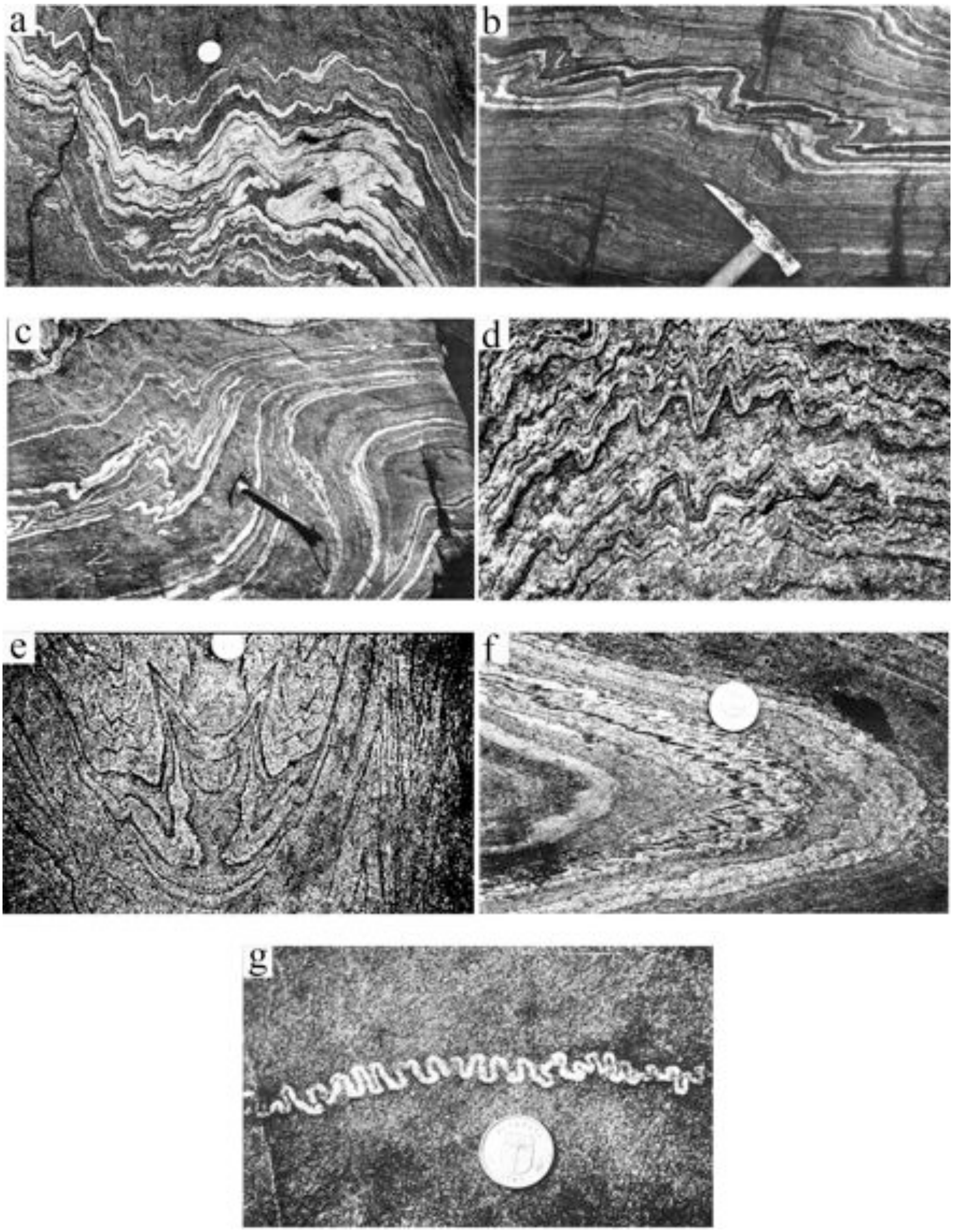

Figure 42 Seven types of folds along with their spectral analysis. Each folded structure was measured (amplitude and wavelength), hence produced geometric spectra, provided power fit. a) Refolded biotite schists and pale quartz-feldsparbands. Cristallia, Swiss Pennine Alps. b) Z-shaped small scale folds in blended hornblende-biotite gneiss, Fusio, central Pennine Alps. c) Superimposed folds interference patterns in gneisses, Cristallina, Lepontine nappes, Switzerland. d) Multilayer of alternating calc-silicate layers and marble. N.Karibib, Namibia. e) Type 2 dome-crescent-mushroom interference patterns. Developed in Moine Series metasendstones. Loch Hourn, NW Scotland. f) Plyharmonic folding in a multilayer of banded hornblende-biotite-feldspar gneiss. Fusio, Ticino, South Switzerland. g) Ptygmatic vein of pegmatite in a granitic host rock. Chindamora, Zimbabwe. Photos and captions from (John J.Ramsay 1987).

Large scale folds (Syrian Arc monoclines)

A geological comparison with the Lisan billow-shaped structures is the monoclines of the Syrian Arc (Figure 43). Eran (1982) measured the height and length of ten monoclines in the Negev, which are part of a large geological S-shaped fold belt extending from the Western Desert of Egypt through Sinai into the Palmyra folds of Syria (Walley, 1998). Most of the folds are asymmetrical and locally faulted by normal and strike-slip faults (Quennell, 1958). We used Eran's (1982) data to perform spectral analysis and examine whether these large-scale tectonic structures follows a uniform power law like the billows of the Lisan Formation. The monocline height and length corresponds to a wave's amplitude and wavelength. The length of the monoclines range from 2500 m to 15,000 m and their height is from 250 m to 1100 m above the monocline base).

Figure 43 The Syrian Arc.

We managed to calculate a reasonable power fit for the Syrian folds monoclines with a value of about -4 (Figure 44).

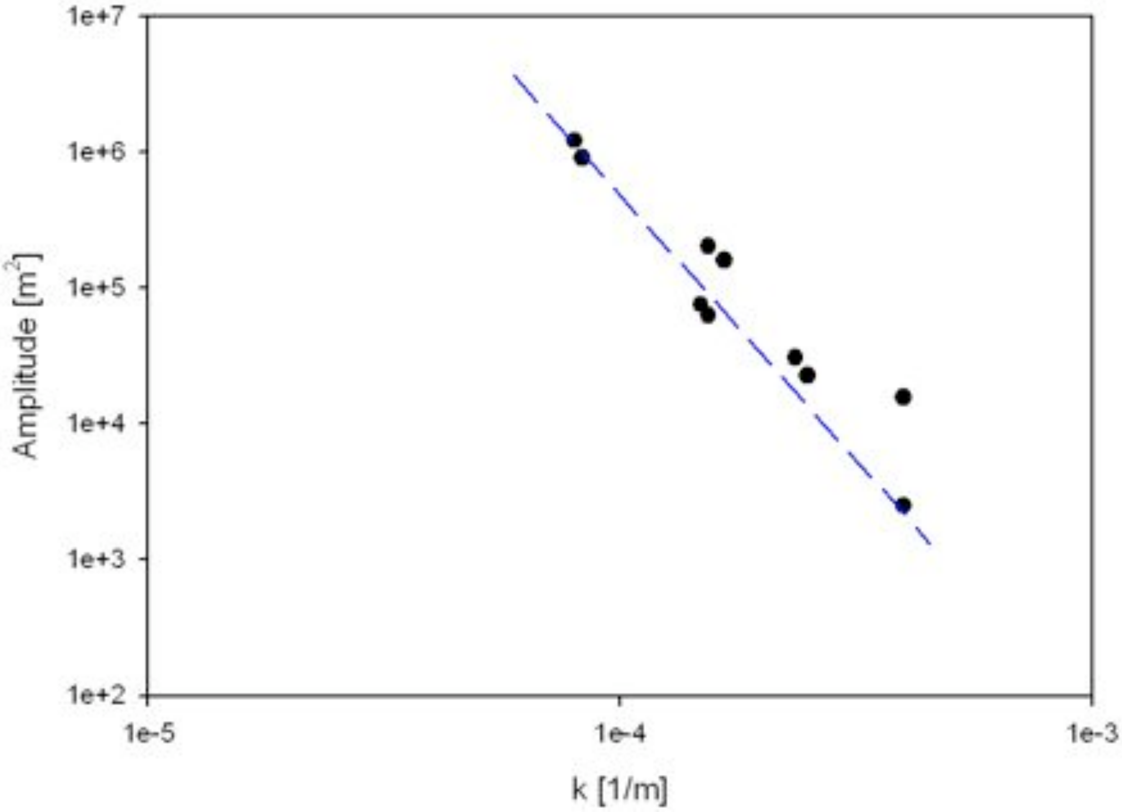

Figure 44 Spectral analysis of the monoclines of the Syrian arc in the Negev; Amplitude square to wave-number relation. Power fit is marked in red line: $y(k)=1.3E^{-10}k^{-3.9}$, $R^2=0.98$.

Our conclusion from this analysis is that large-scale tectonic activity may produce folds with a typical ratio in a power law form. However, the value of the power fit is different to the Lisan folds and the Kolmogorov power law by a factor of 2.3. The monoclines of the Syrian Arc do not fit the energy spectrum of turbulent flow.